RÉPUBLIQUE ALGÉRIENNE DÉMOCRATIQUE ET POPULAIRE
MINISTÈRE DE L'ENSEIGNEMENT SUPÉRIEUR ET DE LA RECHERCHE SCIENTIFIQUE

ÉCOLE NATIONALE POLYTECHNIQUE

Département de Métallurgie

Final year project dissertation

In partial fulfillment of the requirements for the state engineer degree in Materials Engineering

---

Preparation and Characterization of a Polyaniline-Based Photoelectrode for CO_2 Reduction

---

TOUKAL Youcef & ASSIAKHI Redha

Supervised by **Dr. TALBI Lamia** CRTSE and **Pr. LARIBI Merzak** ENP

Publicly defended on: **July 7th, 2025**

Jury committee:

President:	Dr. MERMOUL Soumia	ENP
Examiner:	Dr. DJEMA Oussama	CRTSE

ENP 2025

RÉPUBLIQUE ALGÉRIENNE DÉMOCRATIQUE ET POPULAIRE
MINISTÈRE DE L'ENSEIGNEMENT SUPÉRIEUR ET DE LA RECHERCHE SCIENTIFIQUE

ÉCOLE NATIONALE POLYTECHNIQUE

المدرسة الوطنية المتعددة التقنيات
Ecole Nationale Polytechnique

CRTSE

Département de Métallurgie

Final year project dissertation

In partial fulfillment of the requirements for the state engineer degree in Materials Engineering

---

Preparation and Characterization of a Polyaniline-Based Photoelectrode for CO_2 Reduction

---

TOUKAL Youcef & ASSIAKHI Redha

Supervised by **Dr. TALBI Lamia** CRTSE and **Pr. LARIBI Merzak** ENP

Publicly defended on: **July 7th, 2025**

Jury committee:

President:	Dr. MERMOUL Soumia	ENP
Examiner:	Dr. DJEMA Oussama	CRTSE

ENP 2025

RÉPUBLIQUE ALGÉRIENNE DÉMOCRATIQUE ET POPULAIRE
MINISTÈRE DE L'ENSEIGNEMENT SUPÉRIEUR ET DE LA RECHERCHE SCIENTIFIQUE

ÉCOLE NATIONALE POLYTECHNIQUE

Département de Métallurgie

Mémoire de projet de fin d'études

Pour l'obtention du diplôme d'ingénieur d'état en Génie des Matériaux

---

Préparation et caractérisation d'une photoélectrode à base de polyaniline pour la réduction du CO_2

TOUKAL Youcef et **ASSIAKHI Redha**

Encadré par **Dr. TALBI Lamia** CRTSE et **Pr. LARIBI Merzak** ENP

Présenté et soutenu publiquement le : **7 juillet 2025**

Composition du Jury :

Présidente :	Dr. MERMOUL Soumia	ENP
Examinateur :	Dr. DJEMA Oussama	CRTSE

ENP 2025

ملخص

أدى الارتفاع المستمر في تركيز ثاني أكسيد الكربون في الغلاف الجوي إلى تكثيف الجهود الرامية إلى تحويل هذا الغاز الدفيء إلى مركّبات كيميائية ذات قيمة مضافة باستخدام تقنيات مستدامة. في هذا العمل، قمنا بتطوير وتوصيف فوتوكاثودات هجينة قائمة على البوليانيلين المشبع بحمض الهيدروكلوريك وتركيبات المرسبة على ركائز من الغرافيت، بهدف تحقيق اختزال ضوئي-كهروكيميائي لغاز ثاني أكسيد الكربون. تم اعتماد طريقتي تحضير كيميائية وكهروكيميائية، بما في ذلك إدخال عنصر الزنك كعامل تطعيم لتحسين الخصائص الإلكترونية. أكدت التحليلات الفيزيائية والكهروكيميائية سلامة البنية البلورية، وقدرة نقل الشحنة، والنشاط تحت الإضاءة المرئية. ومن بين الأنظمة المدروسة، أظهر المركب Cu_2O/PANI أفضل أداء في محلول كربونات تحت الإضاءة الشمسية، مما يبرز قدرته العالية على تحويل CO2 بشكل انتقائي وفعال.

الكلمات المفتاحية: اختزال كهروكيميائي ضوئي لثاني أكسيد الكربون – أكسيد النحاس الأحادي – بوليانيلين – الميثانول – محلول كربونات – التحفيز الكهروكيميائي – تطعيم بالزنك – منتجات ذات قيمة مضافة.

Résumé

L'augmentation continue de la concentration atmosphérique de CO_2 a intensifié les efforts visant à convertir ce gaz à effet de serre en composés chimiques à haute valeur ajoutée à l'aide de technologies durables. Dans cette étude, nous avons développé et caractérisé des photoélectrodes hybrides à base de polyaniline dopée à l'acide chlorhydrique (HCl-PANI) ainsi que des composites Cu_2O/PANI déposés sur des substrats de graphite, dans le but de réaliser la photoélectroréduction du CO_2. Des voies de synthèse électrochimiques et chimiques ont été explorées, incluant un dopage au zinc afin d'améliorer les propriétés électroniques du polymère. Les analyses physicochimiques et électrochimiques ont confirmé l'intégrité structurale, la capacité de transfert de charge et l'activité sous lumière visible des électrodes élaborées. Parmi les systèmes testés, le Cu_2O/PANI a présenté les performances photoélectrocatalytiques les plus prometteuses en électrolyte carbonaté sous irradiation solaire, mettant en évidence son fort potentiel pour une conversion du CO_2 sélective et efficace.

Mots clés : Réduction photoélectrochimique du CO_2 - Cu_2O - Polyaniline (PANI) - Méthanol - Électrolyte carbonaté - Électrocatalyse - Dopage au zinc - Produits à haute valeur ajoutée.

Abstract

The increasing atmospheric CO_2 concentration has intensified efforts to convert this greenhouse gas into valuable chemicals using sustainable technologies. In this study, we developed and characterized hybrid photoelectrodes based on HCl-doped polyaniline (PANI) and Cu_2O/PANI composites on graphite substrates, targeting photoelectrocatalytic CO_2 reduction. Both electrochemical and chemical synthesis routes were explored, including Zn-doping to enhance electronic properties. Physicochemical and electrochemical techniques confirmed the structural integrity, charge transfer ability, and visible-light activity of the electrodes. Among the tested systems, Cu_2O/PANI showed the best performance in carbonate electrolyte under solar illumination, highlighting its potential for selective and efficient CO_2 conversion.

Keywords : Photoelectrochemical CO_2 reduction - Cu_2O - Polyaniline (PANI) - Methanol - Carbonate electrolyte - Electrocatalysis - Zn-doping - Value-added products.

Dedication

What is presented in this work is far from being the fruit of individual effort. It is, first and foremost, by the grace of God Almighty, and through the unconditional love and enduring sacrifices of my parents, that I have become the person I am today.

To my mother and father, this work is yours before it is mine. You've given me the most precious gifts one can receive: time, love, belief, and resilience. I will forever be indebted to you, and I ask Allah to grant me the strength and wisdom to give back, even if it could never equal the magnitude of what you have done for me.

To the two companions of my journey, my brothers Younes & Yacine. We argue, we clash, but your presence fills my life with strength and meaning. Without you, none of this would have the same color.

To Loupy, my precious soul companion, who—without saying a word—has accompanied me through the long nights, waited by my side every morning, and reminded me that affection can be silent yet profound.

To my dear friends Jugurtha, Amine, Mohamed, and all those I met along this path. I am grateful for every shared challenge, every late-night discussion, and every laugh. I've learned from each one of you more than you know.

To Redha, my colleague and partner through internships and adventures, thank you for making this journey as much about friendship as it was about science. I couldn't have asked for a better partner.

Finally, to Polytech, a school of life before being a school of engineering. Thank you for shaping not just my academic path, but also my character.

Youcef TOUKAL

Dedication

All praise is due to Allah, the Almighty, who guided me and granted me the strength and patience to reach this milestone. His mercy and blessings have been with me every step of the way.

To my dear father, Mourad
This work is the fruit of your sacrifices, efforts, prayers, and support. I would have loved to offer you more, but today I offer this humble achievement with pride and deep gratitude. May Allah grant you health and happiness beyond measure.

To my dear mother, DJAILEB Samia
You are the source of my strength. Your love and tenderness have carried me every step of the way. Be assured, dearest mother, of my infinite love and devotion. May Allah bless you with a long and peaceful life among us.

To my dear brother, Salim
You are still at the beginning of your journey, and I wish you all the success and fulfillment life can offer. May this achievement inspire you. I believe in you and will always be here for you.

To my dear grandparents
Thank you for your prayers, your kind words, and your unconditional love. May Allah bless you with health and joy.

To my work partner, Youcef TOUKAL
Working with you was a real pleasure. Your dedication and collaboration played a meaningful role in this journey. Thank you sincerely.

To my dear friends: Oussama, Mouloud, Adem, Riad, and Attalah
Your support, laughter, and presence made this path easier and more joyful. I truly appreciate you and dedicate part of this success to you.

To my classmates: Zakaria, Ishek, and Ramdane
Thank you for the friendship, teamwork, and good memories we shared. I'm grateful to have walked this academic journey with you.

To my beloved family
Thank you for always being my foundation. Your unwavering support, love, and encouragement have carried me through every challenge. This accomplishment is dedicated to you, with all my heart.

Redha ASSIAKHI

Acknowledgements

First and foremost, we thank God Almighty for the strength, patience, and clarity that guided us through this journey.

This work would not have been possible without the support and presence of exceptional individuals to whom we are deeply grateful. We sincerely thank ***Mrs. Lamia Talbi****, for her trust, scientific rigor, and her unwavering commitment to seeing this work through with us. We express our heartfelt appreciation to* ***Mr. Merzak Laribi****, whose guidance, and teaching over the years have greatly contributed to our growth. Our gratitude also extends to the members of our jury,* ***Mrs. Soumia Mermoul*** *and* ***Mr. Oussama Djema****, for the honor of reviewing this work and for their thoughtful attention.*

We warmly thank ***Mr. Aissa Keffous*** *and* ***Mr. Toufik Hadjersi*** *for welcoming us into the Emerging Semiconductor Technologies for Energy (TESE) of the Research Center in Semiconductor Technology for Energetics (CRTSE). Our sincere appreciation also goes to* ***Mrs. Sabiha Anas****, Senior Researcher at CRTSE, for her availability and for facilitating the characterization sessions at the El Harrach facility. We extend warm thanks to* ***Mr. H. Menari****, Head of the Scientific Equipment and Device Realization Department at CRTSE, and to* ***Mr. Abdallah Mekkadem****, State Engineer, for their critical support in device fabrication and technological processing. We are deeply grateful to* ***Mrs. Fatima Boudeffar****, Research Support Engineer, and* ***Mrs. Sihem Bouanik****, Research Officer, for their assistance throughout our experiments. Our thanks also go to* ***Mr. Amar Manseri****, Expert Engineer at CRTSE, for his valuable support with the SEM analyses, as well as to* ***Mr. Billel Hamdou****, State Engineer, for conducting the EPMA measurements. We also thank* ***Mr. Youcef Larbah****, Senior Researcher at CRNA, for his support and contribution to the XRD analyses, and* ***Mr. Idir Toumer****, Engineer at CRNA, for carrying out the EDXRF measurements. A special note of appreciation goes to* ***Mrs. Farida Messili****, Principal Engineer at CRNA, whose technical support and warm encouragement left a lasting impression on us. Our deep thanks are also extended to* ***Mr. Khaled Darkaoui****, Senior Researcher at CDTA, for his insightful advice and meaningful contribution to our understanding of the photoelectrochemical processes. Finally, our warmest thanks go to all the professors of the Materials Engineering Department, and to everyone who, from near or far, supported us throughout this thesis. Your help, in all its forms, made a difference. This project is as much the result of science as it is of solidarity.*

Thank you.

Youcef and Redha

Contents

List of Tables **12**

List of Figures **13**

List of acronyms **17**

General introduction **18**

1 Theoretical background **20**

1.1 Introduction 20

1.2 GREEN HOUSE EFFECT 21

1.3 Roots of Air Pollution and GHGs 21

1.3.1 Anthropogenic Air Emissions 21

1.3.2 Growing Population and Energy Consumption 22

1.3.3 Global Air Emissions 22

1.4 Capture and reduction of CO_2 22

1.5 Carbon Capture Technologies 23

1.6 Conversion of CO_2 into Value-Added Products 24

1.6.1 Conversion of CO_2 into Chemicals and Clean Fuels 24

1.7 Electrolysis and photoelectrocatalysis of CO_2 25

1.7.1 Introduction to CO_2 Electrolysis and Photoelectrocatalysis: 25

1.7.2 Photocatalytic CO_2 reduction 25

1.7.3 Electrocatalytic CO_2 reduction 26

1.7.4 Main systems and principle of photoelectrocatalytic CO_2 reduction . . . 27

1.7.5 Evaluation parameters for photoelectrocatalytic CO_2 reduction 29

1.8 Timeline of the development of electrolysis 30

1.8.1 Early Foundations of Electrolysis (18th - 19th Century) 30

1.8.2 First CO_2 Electrolysis Experiments (Mid-19th Century - Early 20th Century) 30

1.8.3 The Emergence of Catalyst Development (Early to Mid-20th Century) . 31

1.8.4 The Impact of the Energy Crisis (1970s - 1990s) 31

1.8.5 Advancements in Catalysis and Reactor Design (Late 20th Century - Early 21st Century) 31

1.8.6 Modern Breakthroughs and Mechanistic Insights (21st Century - Present) 32

1.9 Factors influencing CO_2 photocatalysis 32

1.9.1 Metals for CO_2 Photoreduction 32

1.9.1.1 Catalytic Reduction of CO_2 Reaction Mechanism 33

1.9.1.2 Mechanistic Role of Co-Catalysts in CO_2 Photocatalytic Reduction 34

1.9.1.3 Noble Metal-Based Co-Catalysts 35

1.9.1.4 Non-Precious Metal Co-Catalysts: 37

1.9.2 Semiconductors for CO_2 photoreduction 37

1.9.2.1 Organic semiconducting materials 37

1.9.3 Polyaniline 38

1.9.3.1 Molecular structure and redox states of PANI 39

1.9.3.2 Theoretical considerations of PANI's synthesis 40

1.9.3.2.1 Chemical oxidative polymerization 40

1.9.3.2.2 Electrochemical polymerization 40

1.9.3.3 Doping mechanism and charge transport in PANI 41

1.10 Reactors for CO_2 photoreduction 42

1.10.1 Reactor typologies and their implications 42

1.10.2 Reactor Geometry and Light Distribution 43

1.10.3 Twin reactor systems 43

1.10.4 Integration with PANI-based photoelectrodes 44

1.11 Challenges of CO_2 electrolysis 44

1.11.1 Selectivity 44

1.11.1.1 Thermodynamic and kinetic foundations 45

1.11.1.2 Intermediate binding energetics 45

1.11.1.3 Suppression of the Hydrogen Evolution Reaction 46
1.11.1.4 Faradaic Efficiency and quantitative descriptors 47
1.11.1.5 Selectivity modulation via PANI Matrix Engineering 47
1.11.2 Stability 48
1.11.2.1 Mechanisms of catalyst and electrode degradation 48
1.11.2.2 Strategies for enhancing stability in PANI-based systems 49
1.11.3 Efficiency 50
1.11.3.1 Overpotential Challenges 50
1.11.3.2 Current Density: A Bottleneck for Industrial Translation 51
1.11.3.3 Strategies to Enhance Efficiency in PANI-Based Systems 51

2 Experimental study 52

2.1 Synthesis of PANI/C_{gr} structures 52
2.1.1 Substrate preparation 52
2.1.2 Cleaning of the graphite substrates 52
2.1.3 Preparation of thin films for electrodes 53
2.1.3.1 Electrochemical route 53
2.1.3.1.1 Electropolymerization 53
2.1.3.1.2 Preparation of the Electrolyte Solution 54
2.1.3.1.3 Surface modification of the substrates by copper(I) oxide (Cu_2O) deposition 55
2.1.3.2 Chemical route 56
2.1.3.2.1 Polyaniline synthesis 56
2.1.3.2.2 Chemicals used 56
2.1.3.2.3 Electrode preparation 56
2.1.3.2.3.1 Preparation of the base C/PANI-based paste . . 56
2.1.3.2.3.2 Paste coating procedure on graphite 57
2.1.3.2.4 Synthesis of Zn-Doped Polyaniline (Zn/PANI) 57
2.1.3.2.4.1 Reagents and materials 58
2.1.3.2.4.2 Synthesis protocol 58
2.1.3.2.5 Synthesis of Zn-doped PANI nanocomposites 58
2.1.4 Photoelectrochemical reduction of CO_2 gas 59

2.1.4.1 Experimental setup for CO_2 reduction 59

2.1.4.2 Photoelectrochemical cell 60

2.1.4.3 Electrolyte solution 61

2.2 Characterization techniques 61

2.2.1 Scanning Electron Microscopy 61

2.2.2 Fourier-Transform Infrared Spectroscopy 62

2.2.3 UV-Visible-NIR Absorption Spectroscopy 63

2.2.4 X-Ray Diffraction 64

2.2.5 X-Ray Photoelectron Spectroscopy 65

2.2.6 Wavelength Dispersive X-Ray Fluorescence 65

2.2.7 Photoelectrochemical characterization 65

2.2.7.1 Linear and Cyclic Voltammetry (LSV and CV) 65

2.2.7.2 Chronoamperometry (Potentiostatic Mode) 66

2.2.7.3 Gas chromatography analysis 66

2.2.7.4 Electrochemical Impedance Spectroscopy 67

2.2.7.5 Tafel polarization analysis 67

3 Results and Discussions 68

3.1 Chemical composition of the substrate 68

3.2 Electropolymerization 69

3.2.1 Electrodeposition of polyaniline (PANI) on platinum 70

3.2.2 Electrodeposition of polyaniline (PANI) on graphite 71

3.2.3 Mechanism of PANI polymerization 71

3.3 Fourier Transform Infrared Spectroscopy(FT-IR) 72

3.4 Scanning Electron Microscopy (SEM) 73

3.5 Electron probe microanalysis (EPMA) 76

3.6 X-Ray Diffraction (XRD): 78

3.7 X-ray Photoelectron Spectroscopy (XPS) 79

3.8 UV-Visible 81

3.8.1 Optical band gap 82

3.9 Electrocatalytic activity assessment 84

3.10 Evolution of CO_2 reduction on different electrodes 86
3.10.0.1 Graphite electrode 86
3.10.0.2 HCl-Doped PANI thin films on Graphite electrode 88
3.10.0.3 Bilayer of Cu_2O on HCl-doped PANI on Graphite electrode . . 89
3.11 Gas Chromatography 92
3.12 Characterization of the chemically synthesized electrodes 94
3.12.1 Cyclic voltammetry analysis of chemically synthesized Zn-doped Polyaniline (Zn/PANI) under light irradiation 94
3.12.2 Linear Sweep Voltammetry analysis of chemically synthesized Zn-doped PANI Electrodes in CO_2-Free and CO_2-Saturated Environments 96
3.12.3 Chronoampermetry analysis of chemically synthesized Zn-doped PANI Electrodes 99
3.13 Electrokinetic evaluation through Tafel polarization analysis 100
3.14 Interfacial charge transport and photoelectrochemical impedance analysis 104
3.14.1 Electrochemical route 105
3.14.1.1 Nyquist 105
3.14.1.2 Bode 106
3.14.2 Chemical route 109
3.14.2.1 NYQUIST 109
3.14.2.2 Bode 110
3.15 Comparative evaluation of photoelectrocatalytic parameters 111
3.16 Conclusion 113

General conclusion **114**

Bibliography **116**

List of Tables

1.1 Different reduction products obtained from the photocatalytic reduction of CO_2 in an aqueous solution and the corresponding electrode potentials (vs. standard hydrogen electrode, 25 °C, pH = 7).[1] 33

2.1 Chemicals and reagents used 56

3.1 proportion of elements in grpahite substrate 69

3.2 Elemental composition of HCl-doped PANI using EDS analysis 76

3.3 Chemical composition of the layer by EPMA 77

3.4 Elemental composition (atomic %) of each bonding environment in PANI synthesized by chemical and electrochemical methods. 80

3.5 Electrokinetic parameters of the catalysts in the absence of CO_2 (illumination, 0.5 M K_2CO_3). 103

3.6 Electrokinetic parameters of the catalysts in the presence of CO_2 (illumination, 0.5 M K_2CO_3). 103

3.7 Comparison of Tafel slopes, charge transfer resistances, and chronoamperometric current plateaus ($V = -1.6$ V) for various catalysts under illumination in CO_2-saturated* 0.5 M K_2CO_3. 112

List of Figures

1.1 Global atmospheric concentrations of greenhouse gases [2] 21

1.2 Share of Global CO2 Emissions Attributed to Algeria (1916–2023) [3] 22

1.3 Global greenhouse gas emissions by sectors [2] 22

1.4 Global atmospheric CO_2 concentrations [4] 23

1.5 Global average temperature anomaly[5] 23

1.6 Common routes for CO_2 separation, capture and utilization[6] 24

1.7 Basic principles of catalytic CO_2 reduction. (a) Analogy diagram of natural photosynthesis and schematic of photocatalytic CO_2 reduction. (b) Schematic diagrams for electrocatalytic CO_2 reduction system. Photoelectrocatalytic systems: (c) photocathode + dark anode, (d) dark cathode + photoanode, (e) photocathode + photoanode, (f) solar cell + electrodes [7] 27

1.8 Continuous-flow PEC CO_2 reduction system [7] 29

1.9 Schematic diagram of evaluation parameters for photoelectrocatalytic CO_2 reduction. [7] 30

1.10 Mechanism of photocatalytic CO_2 reduction. [8] 35

1.11 Mechanism diagram of CO_2 reduction by Pt-TiO2 photocatalyst. [9] 36

1.12 Chemical structure and redox forms of PANI [10]. 40

1.13 Electronic structure and charge carrier formation (polaron, bipolaron) in doped PANI [11]. 42

1.14 Representative configurations of photoreactors for CO_2 photoreduction: Batch (a, e, f), Flow (b, c), and Recirculating (d) systems [12]. 43

1.15 Typical electrochemical cell configurations for CO_2 reduction: (A) H-type Cell (Three-electrode PEC Cell), (B) Flow Cell (GDE architecture), and (C) MEA system [13]. 44

1.16 Schematic of a typical CO_2RR to CO process at electrochemical reaction interface (reaction microenvironment). ET means electron transfer, and PET means proton–electron transfer. The dashed box represents the evolution of the same active site at different stage of CO_2RR [14]. 46

2.1 Cutting of graphite rods 52

2.2 Experimental setup for electrochemical polymerization 54

2.3 Preparation of the electrolyte solution 55

2.4 Steps for the preparation of copper(I) oxide (Cu_2O) coating: (a) preparation of $CuSO_4$ solution, (b) electrochemical deposition of Cu_2O onto the substrate. . . . 55

2.5 Stages of C/PANI paste preparation: (a) PVDF/NMP solution, (b) C/PANI composite powder, (c) paste during homogenization (d) final viscous paste. . . . 57

2.6 Manual spreading of the C/PANI paste on the graphite electrode 57

2.7 Schematic of the conventional electrochemical setup for CO_2 reduction 60

2.8 Schematic and visual representation of the three-electrode electrochemical cell . 61

2.9 Scanning Electron Microscope JEOL JSM 7610FPlus (CRTSE) 62

2.10 Thermo Nicolet FTIR Spectrometer (CRTSE) 63

2.11 CARY 5000 UV-Vis-NIR Spectrophotometer (VARIAN), CRTSE 63

2.12 Illustration of the XRD analysis principle and diffraction from crystallographic planes 64

2.13 Schematic of the gas chromatographic system setup [15]. 67

3.1 EDXRF peak of Carbon 68

3.2 Voltammogram of HCl-PANI electropolymerization on Platinum in a solution of 0.2 M aniline, 0.5 M HCl, at a scan rate of 20 mV/s 70

3.3 Voltammogram of HCl-PANI electropolymerization on graphite in a solution of 0.2 M aniline, 0.5 M HCl, at a scan rate of 20 mV/s 71

3.4 Mechanism of electropolymerization of polyaniline. 72

3.5 FTIR spectrum of HCl-Doped PANI. 73

3.6 SEM images of Hcl-Doped PANI powder. 74

3.7 SEM images of pure PANI powder. 74

3.8 SEM images of HCl-Doped PANI thin film deposited on graphite substrate. . . . 75

3.9 SEM images of Cu_2O/HCl-PANI thin film deposited on graphite 75

3.10 EDS spectra of HCl-Doped PANI deposited on graphite substrate. 76

3.11 Morphology of the layer obtained by EPMA. 77

3.12 characteristic peaks of the chemical elements present in the layer. 77

3.13 X-Ray diffraction distribution of Hcl-doped PANI, Zn-Doped PANI and PANI-30% Zn nanocomposite 78

3.14 XPS survey and high resolution spectra of PANI-HCl synthesized via chemical and electrochemical methods: (a) full survey spectra; high resolution C 1s (b,e), N 1s (c,f), and O 1s (d,g) spectra for PANI obtained by chemical method (b,c,d) and electrochemical method (e,f,g). 81

3.15 Reflexion spectra of powders: HCl-PANI, Zn-PANI, and PANI-Zn 30%. 82

3.16 Reflexion spectra of HCl-PANI/C_{gr} 82

3.17 Determination of the optical band gap of the different forms of PANI 83

3.18 Comparative voltammetric profiles of graphite-based electrodes modified with PANI or Cu_2O/HCl-PANI in alkaline (0.1 M NaOH) and carbonated (0.5 M K_2CO_3) electrolytes. 85

3.19 LSV curves of cylindrical graphite in 0.5 M K_2CO_3 electrolyte, recorded under sunlight illumination, with and without CO_2 saturation, at a scan rate of 10 $mV \cdot s^{-1}$ 86

3.20 CV curves of cylindrical graphite in 0.5 M K_2CO_3 electrolyte, under solar illumination, comparing the electrochemical response in the presence and absence of CO_2, at a scan rate of 10 $mV \cdot s^{-1}$ 87

3.21 Chronoamperometric response of graphite electrode in 0.5 M K_2CO_3 as a function of the applied potential under CO_2 atmosphere 87

3.22 LSV curves of HCl–PANI/graphite electrode in 0.5 M K_2CO_3 electrolyte, under sunlight illumination, in CO_2-saturated/free environments, at a scan rate of 10 $mV \cdot s^{-1}$ 88

3.23 CV curves of HCl–PANI/graphite electrode in 0.5 M K_2CO_3 electrolyte, under constant illumination, comparing the electrocatalytic response with and without CO_2 saturation 88

3.24 Chronoamperometric characterization of HCl–PANI/graphite electrode in 0.5 M K_2CO_3 electrolyte under CO_2 atmosphere as a function of applied potential . . . 89

3.25 LSV curves of Cu_2O/HCl–PANI electrode on graphite in 0.5 M K_2CO_3 electrolyte, under sunlight illumination, in the presence and absence of CO_2, at a scan rate of 10 $mV \cdot s^{-1}$ 89

3.26 CV curves of Cu_2O/HCl–PANI/graphite electrode in 0.5 M K_2CO_3 electrolyte, under solar illumination, comparing the electrocatalytic behavior with and without CO_2 90

3.27 Chronoamperometric profile of Cu_2O/HCl–PANI/graphite electrode in 0.5 M K_2CO_3 electrolyte under CO_2 atmosphere as a function of the applied potential 90

3.28 Characteristic peaks of a Gas Chromatograph of the electrolyte after CO2 reduction using PANI/Cgr as photocathode. 93

3.29 Characteristic peaks of a Gas Chromatograph of the electrolyte after CO2 reduction using Cu2O /PANI/Cgr as photocathode. 93

3.30 Cyclic voltammetry curves of PANI-based electrodes (undoped, 20% Zn, 30% Zn) in 0.5 M K_2CO_3 under illumination, in the absence of CO_2. 95

3.31 Cyclic voltammetry curves of PANI-based electrodes (undoped, 20% Zn, 30% Zn) in 0.5 M K_2CO_3 under illumination, in the presence of CO_2. 95

3.32 Linear sweep voltammetry of PANI-based electrodes (undoped, 20% Zn, 30% Zn) in 0.5 M K_2CO_3 under illumination, in the absence of CO_2. 96

3.33 Linear sweep voltammetry of PANI-based electrodes (undoped, 20% Zn, 30% Zn) in 0.5 M K_2CO_3 under illumination, in the presence of CO_2. 97

3.34 Chronoamperometric Response of PANI, PANI-20%Zn and PANI-30%Zn at -1.6 V 99

3.35 Overall Tafel polarization curves of HCl-doped PANI electrode in 0.5 M K_2CO_3 electrolyte 100

3.36 Tafel polarization behavior of Cu_2O/HCl–PANI hybrid electrode in 0.5 M K_2CO_3 electrolyte 101

3.37 Tafel polarization response of undoped PANI (chemically synthesized) electrode in 0.5 M K_2CO_3 electrolyte 101

3.38 Tafel polarization curves of 30% Zn–doped PANI electrode in 0.5 M K_2CO_3 electrolyte 102

3.39 Tafel polarization curves of 20% Zn–doped PANI electrode in 0.5 M K_2CO_3 electrolyte 102

3.40 Nyquist plot ($-Z''$ vs Z') of the HCl-doped PANI/graphite electrode in 0.5 M K_2CO_3 under CO_2 atmosphere. 105

3.41 Nyquist plot of Cu_2O-Hcl/PANI 105

3.42 Bode phase and impedance magnitude plots of HCl-doped PANI in 0.5 M K_2CO_3 under CO_2 atmosphere across the frequency domain (1 mHz–100 kHz). 106

3.43 Bode plot of Cu_2O/HCl-doped PANI electrode in 0.5 M K_2CO_3 under CO_2 atmosphere across the frequency domain (1 mHz–100 kHz). 106

3.44 Nyquist plots for pure PANIand PANI-30%Zn nanocomposite. 109

3.45 Bode plots for PANI/Cu_2O,PANI,and PANI/30%Zn nanocomposite. 110

List of acronyms

- **APS** : Ammonium peroxodisulfate
- **CCUS** : Carbon capture, utilization, and storage
- **CO_2RR** : Carbon dioxide Reduction Reaction
- **CA** : Chronoamperometry
- **CV** : Cyclic Voltammetry
- **EIS** : Electrochemical Impedance Spectroscopy
- **EDI Water** : Electrodeionized Water
- **EPMA** : Electron Probe Microanalysis
- **EB** : Emeraldine Base
- **ES** : Emeraldine Salt
- **FE** : Faradic Efficiency
- **FT-IR** : Fourier-Transform Infrared Spectroscopy
- **HOMO** : Highest Occupied Molecular Orbital
- **HER** : Hydrogen Evolution Reaction
- **ICPS** : Intrinsically conducting polymers
- **LSV** : Linear Sweep Voltammetry
- **LUMO** : Lowest Unoccupied Molecular Orbital
- **MEA** : Membrane electrode assemblies
- **NPs** : Nanoparticles
- **NMP** : N-Methyl-2-pyrrolidone
- **PANI** : Polyaniline
- **PVDF** : Polyvinylidene fluoride
- **PEC** : Photoelectrochemical cells
- **SEM** : Scanning Electron Microscopy
- **TON** : Turnover number
- **XRD** : X-ray Diffraction
- **XPS** : X-ray Photoelectron Spectroscopy

General introduction

“In nature, carbon dioxide is the end product of the oxidation of organic matter.
In the future, it may become the starting point for the synthesis of renewable fuels.”

Aresta, Michele. Carbon Dioxide as Chemical Feedstock, 2010

Humanity now stands at a critical juncture, shaped by an escalating climate crisis and an insatiable global demand for energy. Anthropogenic greenhouse gas (GHG) emissions, particularly those of carbon dioxide (CO_2), have disrupted the Earth’s radiative balance, intensifying the greenhouse effect and driving global warming beyond preindustrial thresholds. As of 2023, atmospheric CO_2 concentrations have reached 421 ppm—nearly 50% above preindustrial levels—resulting in the breach of the 1.5 °C global temperature anomaly for the first time in modern history [16, 17, 18]. The predominant contributor to this rise remains the combustion of fossil fuels, accounting for over 84% of global energy-related CO_2 emissions, augmented by land-use change and industrial processes [19].

In response, the scientific community has mobilized toward sustainable carbon management strategies that not only aim to limit CO_2 emissions but also to valorize CO_2 as a resource. Among the portfolio of CO_2 mitigation technologies, photoelectrocatalytic (PEC) reduction has emerged as a particularly promising approach due to its dual advantage of using sunlight—a clean, renewable energy source—and its ability to convert CO_2 into energy-rich, value-added products under ambient conditions. This process represents a biomimetic analogy to natural photosynthesis, wherein semiconducting materials absorb photons, generate charge carriers, and catalyze redox reactions at the solid–liquid interface.

Yet, CO_2 is one of the most thermodynamically stable molecules, with a high bond dissociation energy (C=O: 805 kJ/mol) [17], making its activation and conversion a formidable challenge. The development of efficient, robust, and selective catalysts capable of reducing the kinetic barriers associated with multi-electron CO_2 reduction pathways is, therefore, an essential prerequisite. Conductive polymers, particularly polyaniline (PANI), offer an intriguing platform in this regard. With its unique redox flexibility, controllable doping states, and excellent conductivity, PANI has demonstrated significant promise in facilitating charge transport and enhancing catalytic activity when interfaced with semiconductors or metals. Moreover, PANI’s low cost, chemical tunability, and environmental stability make it an attractive candidate for integration into PEC systems.

To further enhance charge separation and suppress recombination phenomena, hybrid photoelectrodes—composed of organic PANI matrices doped with inorganic semiconductors such as Cu_2O—have been explored as a means of constructing energetically favorable heterojunctions. These heterostructures promote synergistic interactions, enabling efficient charge transfer across interfaces and facilitating the formation of reaction intermediates necessary for CO_2 reduction.

This thesis is situated within the broader effort to develop sustainable PEC systems for CO_2 valorization. Specifically, it focuses on the preparation and characterization of hybrid photoelectrodes based on HCl-doped polyaniline, with or without copper(I) oxide decoration, deposited onto graphite substrates. These systems are evaluated for their photoelectrocatalytic performance in carbonate-based aqueous electrolytes under solar illumination. The work includes both electrochemical and physicochemical characterizations to establish structure–property–performance relationships and assess the stability, selectivity, and energy efficiency of the developed materials.

This dissertation is organized into three chapters:

Chapitre 1 : This chapter presents a detailed bibliographic review of the scientific and environmental context surrounding CO_2 emissions, carbon capture and utilization (CCU), and the fundamental principles of electrochemical and photoelectrochemical CO_2 reduction. It elaborates on the physicochemical properties of polyaniline, its doping mechanisms, charge transport phenomena, and its integration with inorganic semiconductors in hybrid electrode design.

Chapitre 2 : Here, the methodologies employed for the synthesis of PANI-based electrodes are described, including both chemical and electrochemical polymerization routes. The protocols for Cu_2O deposition, surface modification, and CO_2 photoelectroreduction experiments are presented. The chapter also details the instrumental techniques used for morphological, compositional, and electrochemical analyses.

Chapitre 3 : This chapter discusses the experimental results obtained from structural, spectroscopic, and electrochemical characterizations. The analysis includes XRD, SEM, XPS, UV-Vis, FTIR, CV, LSV, EIS, and gas chromatography, with emphasis on the influence of dopants on catalytic performance.

The thesis concludes with a general summary of the achieved outcomes and outlines potential directions for future research in the domain of conductive polymer-based photoelectrocatalysis.

Chapter 1

Theoretical background

1.1 Introduction

The greenhouse effect, sustained by infrared-absorbing gases like water vapor (H_2O), carbon dioxide (CO_2), and ozone (O_3), continues to maintain Earth's surface temperature approximately 30°C warmer than would otherwise occur naturally, but anthropogenic activities have dramatically amplified this effect through escalating emissions of long-lived greenhouse gases [20], with atmospheric CO_2 concentrations rising from 280 ppm preindustrially to 421 ppm in 2023 [16] (driven primarily by fossil fuel emissions exceeding 10 Pg C/yr [21] alongside land-use changes contributing 1.9 Pg C/yr [22]), methane (CH_4) increasing from 700 ppb to 1,911 ppb in 2022 [23] (attributed to fossil fuel leaks, agricultural activities, and thawing Arctic wetlands [24]), and nitrous oxide (N_2O) reaching 336 ppb in 2023 [25] (largely from synthetic fertilizer use and industrial processes), while synthetic compounds like CFCs - though declining by about 1% annually [26] due to the Montreal Protocol's success - continue to contribute to atmospheric warming [17] ; critically, current CO_2 emissions now surpass the absorption capacity of natural sinks by nearly 50%, revealing persistent gaps in our understanding of carbon cycle dynamics, and climate models increasingly highlight concerning feedback loops like permafrost methane release as global temperatures in 2023 exceeded 1.5°C above preindustrial levels for the first time, underscoring the urgent need for both emission reductions and enhanced scientific understanding of these complex atmospheric interactions.[27][6]

In response to these alarming trends, innovative carbon management strategies are urgently needed, not only to curb emissions but also to actively remove and convert atmospheric CO_2 into value-added products. The recycle of CO_2 through its conversion into fuel is considered as one of the best alternatives to tackle the energy and environmental issue. As CO_2 is thermodynamically very stable, it requires huge energy for its conversion to fuel. The energy required for CO_2 conversion could be in the form of thermal (photo-thermal-catalytic) , electrical (electro-catalytic) and solar (photocatalytic). As energy source, the electro and solar pathways are considered 'greener' compared to the thermocatalytic process.[28]

CO_2 is an extremely stable molecule; hence, an appropriate catalyst is required to facilitate its activation by lowering the energy barrier. Various catalysts, including metal-based systems and conducting polymers like polyaniline (PANi), have been identified to effectively lower this barrier and enhance CO_2 reduction efficiency via synergistic mechanisms. PANi is particularly notable for its versatile interaction with CO_2, cost-effectiveness, stability, and tunable properties, making it an excellent catalyst option for CO_2 reduction reactions (CO_2RR).[29]

1.2 GREEN HOUSE EFFECT

The greenhouse effect occurs when atmospheric gases likeCO_2, CH_4, N_2O and fluorinated gases absorb and re-emit solar radiation, trapping heat through their molecular structure. Unlike water vapor which responds quickly to temperature changes (condensing or evaporating), these non-condensing gases maintain stable concentrations and provide the primary radiative forcing that sustains the greenhouse effect. Without them, the effect would collapse as water vapor alone cannot drive long-term warming. Wastewater treatment plants (WWTPs) have emerged as significant GHG sources, emitting CO_2 (microbial respiration), CH_4 (anaerobic digestion) and N_2O (nitrification/denitrification) directly, plus indirect emissions from energy use and bio-solids transport. Other major contributors include fossil fuel combustion, industrial activities, agriculture (livestock, rice farming, fertilizers) and land-use changes, all driving global temperature rise.[30]

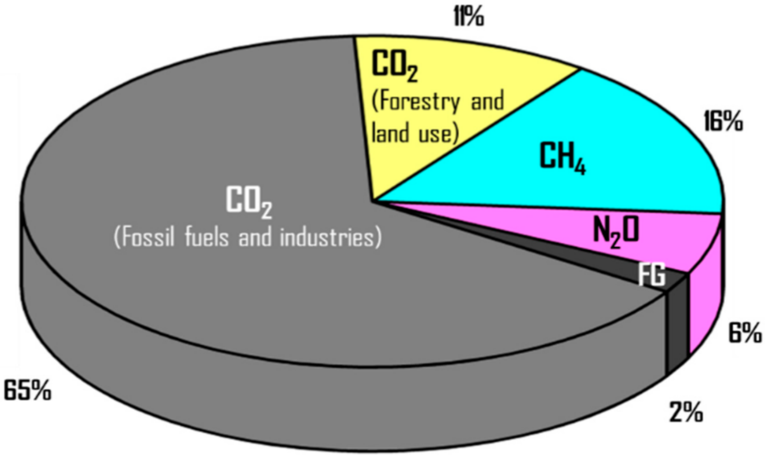

Figure 1.1: Global atmospheric concentrations of greenhouse gases [2]

1.3 Roots of Air Pollution and GHGs

Air emissions arise from both natural and anthropogenic sources. Natural processes contribute a variety of substances that are classified as air emissions. For instance, volcanic eruptions release significant quantities of carbon monoxide (CO), sulfur dioxide (SO_2), and particulate matter (ash). Methane emissions occur naturally through the biological processes of digestion in animals and the decomposition of organic matter. Additionally, radon gas is released as a result of radioactive decay within the Earth's crust, and wildfires produce smoke and carbon monoxide. Nevertheless, these natural sources are not the primary focus of social concern.

1.3.1 Anthropogenic Air Emissions

Anthropogenic sources are related to the production and combustion of various fuels. In recent years, human activities have been shown to contribute significantly to the increases in ground-level ozone (O_3) and greenhouse gases (GHGs). Approximately 95% of the nitrogen oxides (NOx) emitted from anthropogenic sources are the result of the combustion of fossil fuels in power generation facilities, internal combustion engines, residential heating and industrial processes[31]. Air emissions are the resultant byproducts of energy production and consumption; for example, methane combustion (CH_4) in the presence of pure oxygen (O_2) can be represented in a simplified chemical reaction format as follows:

$$CH_4 + 2O_2 \rightarrow CO_2 + 2H_2O + \text{heat} \tag{1.1}$$

1.3.2 Growing Population and Energy Consumption

Global population growth, particularly in developing nations, drives increasing air emissions as people pursue better lifestyles and transportation. While 20th century medical and agricultural advances enabled this growth (projected to reach 7.4-10.6 billion by 2050), it has significantly impacted CO_2 emissions - rising from 21.2 to 26.9 billion metric tons globally. This growth pattern shows regional variations: stable North American emissions, European reductions, and Asia's doubled output. Developing nations face particular challenges as both population growth and rising living standards increase energy demands.[32]

1.3.3 Global Air Emissions

before the 1980s, air pollution was mainly a local concern. strict national industrial controls in developed countries led to a significant reduction in air emissions and improved the air quality in urban areas. for example, the us clean air act of 1970 was passed to address the increasing concerns of air pollution. similar changes took place throughout the industrialized world at that time, and the ambient air quality has improved locally in developed countries. in a modern world, air emissions should be considered from a global perspective. while some people enjoy the comfort and speed of modern conveniences and luxuries provided by energy consumption, others are suffering from the resulting air emissions, with or without intention. there is no doubt that fossil fuel is and will remain the dominant source of global energy in the coming decades. the demand for fossil fuels is still growing, as is the output of air emissions.[33]

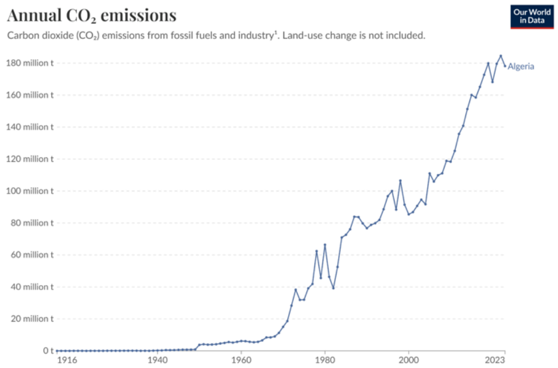

Figure 1.2: Share of Global CO2 Emissions Attributed to Algeria (1916–2023) [3]

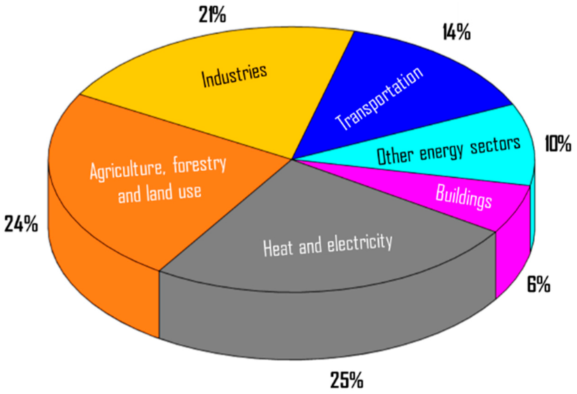

Figure 1.3: Global greenhouse gas emissions by sectors [2]

1.4 Capture and reduction of CO_2

The urgent need to reduce carbon emissions and advance carbon capture technologies has become a global priority for environmental and human health protection. Greenhouse gas concentrations - particularly CO_2, CH_4, and N_2O - continue rising due to fossil fuel combustion and industrial activities, with annual anthropogenic CO_2 emissions exceeding 565 gigatons. This has driven global temperatures up by 1.1°C since 1850, risking severe consequences including extreme weather, sea level rise, ecosystem collapse, and public health crises. While coal remains the second-largest primary energy source after oil, transitioning to renewables (solar, wind, tidal) and nuclear power is critical. Current carbon capture efforts focus on mitigating emissions from major sources like power plants (40 gigatons CO_2/year), though natural processes like photosynthesis (440 gigatons/year land-atmosphere exchange) help balance the carbon cycle. The development of efficient capture technologies must accelerate to address this complex challenge spanning energy production, industrial processes, and land use.[34]

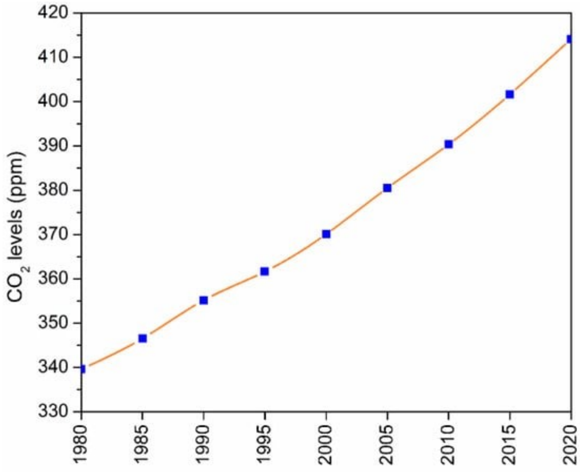

Figure 1.4: Global atmospheric CO_2 concentrations [4]

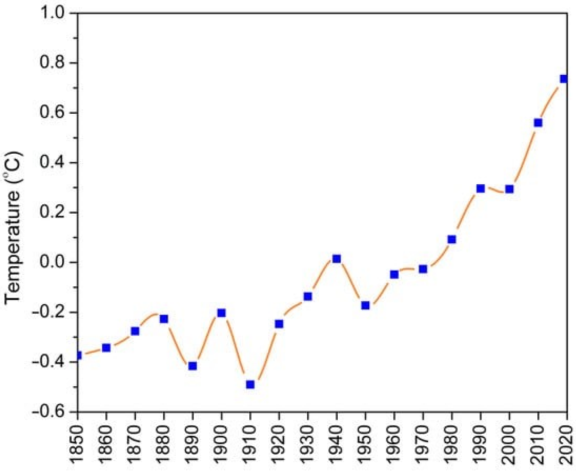

Figure 1.5: Global average temperature anomaly[5]

The growing urgency of climate change has propelled carbon capture, utilization, and storage (CCUS) technologies to the forefront of global climate action, as evidenced by the landmark commitments made during COP26 where 140 of 197 nations pledged to achieve net-zero emissions by 2050, alongside specific agreements to phase out coal, halt deforestation, and accelerate electric vehicle adoption. These ambitious targets - aimed at limiting global warming to 1.5°C - underscore the critical role of CCUS in mitigating anthropogenic emissions while acknowledging the need for parallel transitions in energy systems and land use. This comprehensive review synthesizes foundational and cutting-edge research to systematically evaluate recent advances in CCUS technologies, employing an evidence-based approach to identify knowledge gaps, analyze quantitative data on CO_2 valorization pathways, and provide actionable recommendations for future development. By critically examining the most relevant studies across capture methods, utilization potential, and storage solutions, we aim to advance both theoretical understanding and practical implementation of these vital climate mitigation strategies[35].

1.5 Carbon Capture Technologies

Carbon capture technologies have become globally critical as fossil fuel emissions increasingly threaten ecosystems, human health, and economic stability. These technologies support multiple UN Sustainable Development Goals while enabling the transition to net-zero emissions. The CCUS process involves four key phases:

- Capture from point sources (flue gases) using absorption, adsorption, or membrane separation.

- ∗ Compression for storage/transport.
- ∗ Geological sequestration in porous rock formations (onshore/offshore) capped by impermeable layers.
- ∗ utilization through conversion to chemicals, enhanced oil recovery, or direct applications (food/beverage processing, synthetic fuels).

Figure 1.6 illustrates major capture pathways (pre/post-combustion, oxyfuel, direct air) and technologies (chemical looping, cryogenic distillation, etc.).

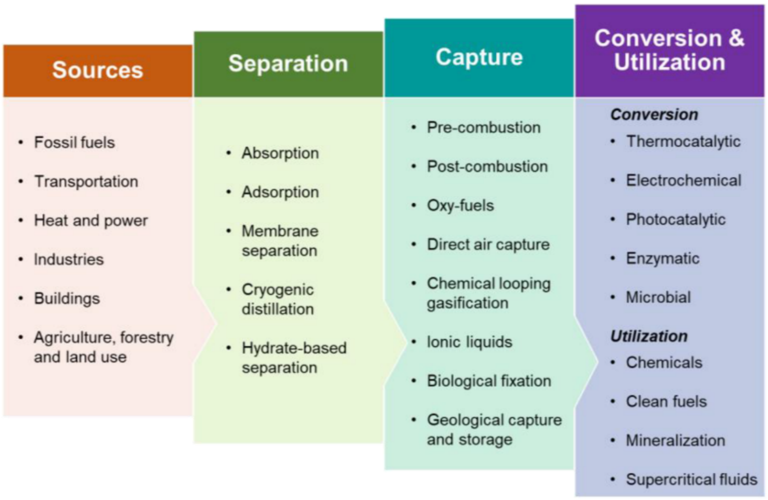

Figure 1.6: Common routes for CO_2 separation, capture and utilization[6]

1.6 Conversion of CO_2 into Value-Added Products

The recent trends in CO_2 utilization technologies have advanced significantly and shifted towards the fuel synthesis, production of carbonates, polycarbonates and different valuable chemicals such as formic acid, formaldehyde, methane, syngas, ethanol, methanol, dimethyl ether, urea and salicylic acid. Solar fuel involves the conversion of solar or other renewables to chemical energy; thus, a chemical energy carrier is produced. Fuels with high energy density make them apposite for energy storage and transportation. CO2 utilization has evolved as a suitable carbon-based solar fuel without distorting the existing infrastructures. The process involves the splitting of CO_2 into CO and O_2. CO can be processed with green H_2 to produce a wide range of clean fuels and chemicals via the Fischer–Tropsch process.

1.6.1 Conversion of CO_2 into Chemicals and Clean Fuels

Refineries traditionally rely on fossil-derived syngas, hydrogen, and hydrocarbons for chemical production, but CO_2 utilization now offers sustainable alternatives through multiple conversion pathways. Thermocatalytic methods dominate industrial applications, including hydrogenation, methanation and Fischer-Tropsch synthesis - with Fe/Na-ZSM-5 catalysts showing enhanced olefin selectivity and Co/Mn/Na/S systems achieving 54% C2-C4 yields at 240°C. The reverse water-gas shift reaction demonstrates 22.2 µmol CO/min/g productivity using MO_2C catalysts. Electrochemical approaches show promise, particularly bimetallic systems like Au/Cu for C^{2+} alcohols and CuIn hydroxides reaching 85% formate efficiency. Photocatalytic routes generate acetaldehyde (C-doped SnS_2), methanol (5.3 µmol/g/h with Mo-WO_3), and hydrocarbons via Cu-Zn oxides, while microbial conversion achieves iso-propanol (26.5 mg/L) and ethylene (718 µg/L/OD/h) through engineered microorganisms. Despite progress, challenges persist in light olefin selectivity for CO_2-based Fischer-Tropsch processes, though integrated thermochemical, electrochemical and biological approaches demonstrate growing potential for scalable CO_2 utilization.[6]

1.7 Electrolysis and photoelectrocatalysis of CO_2

1.7.1 Introduction to CO_2 Electrolysis and Photoelectrocatalysis:

Currently, the artificial methods for CO_2 conversion primarily consist of high-temperature catalytic hydrogenation, electrocatalytic reduction, photocatalytic conversion, and photoelectrocatalytic methods. Electrocatalytic reduction benefits from an ample supply of electrons, enabling multi-electron reduction processes that yield a variety of products. Furthermore, variations in the reduction medium (gas phase or liquid phase) and reaction temperature (high or low) can enhance the diversity of product types. However, if the external voltage is excessively high, it may trigger competitive hydrogen evolution reactions, which can decrease the Faraday efficiency during the electrocatalytic reduction process. Additionally, factors such as the type of electrode or catalyst and the voltage magnitude result in a lack of absolute selectivity for specific products in electrocatalytic reduction, often leading to a mixture of several substances. This presents a significant challenge in the CO_2 electrocatalytic reduction process. In contrast to the aforementioned technologies, photocatalytic CO_2 reduction effectively harnesses solar energy while mitigating the need for high-temperature and high-voltage conditions, thus offering promising applications. Nonetheless, photocatalysts typically exhibit limited solar energy utilization efficiency and low separation efficiency of photogenerated carriers, resulting in decreased overall efficiency for photocatalytic CO_2 reduction. Moreover, the frequent addition of sacrificial agents in liquid-solid photocatalytic systems increases economic costs. Additionally, the current catalytic efficiency in gas-solid photocatalytic systems for CO_2 reduction remains relatively low, thereby constraining the practical application of existing photocatalytic CO_2 reduction technologies. To address these challenges, researchers have proposed photoelectrocatalytic CO_2 reduction technology, which integrates the advantageous features of both photocatalysis and electrocatalysis.

A photoelectrocatalytic system can help separate charges by adjusting certain energy levels. This allows for the quick movement of multiple electrons and protons, which improves the efficiency of the chemical reactions needed to reduce CO_2 on the cathode, producing desired products more rapidly. Additionally, by fine-tuning the key steps in the CO_2 reduction process, we can influence which products are created. Photoelectrocatalysis can also overcome energy challenges by applying an external voltage, leading to better solar energy conversion compared to traditional photocatalysis. These advantages highlight the promising potential of photoelectrocatalytic CO_2 reduction technology.[36, 37]

1.7.2 Photocatalytic CO_2 reduction

The most common CO_2 conversion method is photosynthesis in natural world, which means that green plants or photosynthetic bacteria convert CO_2 in the air into oxygen and/or energy materials necessary for growth under light conditions. Photocatalytic (PC) reduction of CO_2 is similar to plant photosynthesis in Figure 1.7.a, which is that the electrons and holes on surface of photocatalyst respectively reduce CO_2 and oxidized water to produce oxygen under light irradiation. When the incident light energy is larger than the band gap (Eg), the electrons would be excited to conduction band (CB) while holes will be generated in valence band (VB), as shown in Figure 1.7.a. On the one hand, the photogenerated electrons and holes would recombine (volume recombination and surface recombination). On the other hand, the photogenerated electrons react with CO_2 adsorbed on the surface to generate CO, CH_4 and CH_3OH, etc., while photogenerated holes oxidize water to H^+ and O_2 .Over the years, researchers have developed and designed many types of photocatalysts, including metal oxides, metal chalcogenides, metal nitrides, metal phosphides, layered double hydroxides (LDHs) and non-metal semiconductors, etc. Although there are various photocatalytic materials, their practical application efficiency of CO_2 reduction is still not ideal. Therefore, researchers developed plentiful strategies of catalyst modification to optimize photocatalytic performance, including morphology and size control, crystal face control, doping, noble metal deposition, semiconductor recombination, dye sensitization, and defect construction, etc. To some extent, these modification strategies can improve efficiency of light utilization and carrier separation, thus enhancing the reactivity and product selectivity. However, a series of problems still exist in the practical application. For examples, many sacrificial agents usually need to be added in liquid-solid reaction system of photocatalytic CO_2 reduction that leads to increase the cost, while the catalytic efficiency is relatively low in the gas-solid reaction system, which further restricts the application of this technology. Therefore, it is necessary to develop new photocatalysts or new CO_2 reduction systems. Additionally, the studies about surface reaction process, absorption mechanism of solar energy, separation and migration of electrons/holes, are all conducive to elucidation of the surface microstructure and energy band structure of the catalyst, so as to improve the catalytic efficiency of CO_2 reduction[38, 39]

1.7.3 Electrocatalytic CO_2 reduction

The process of electrocatalytic (EC) CO_2 reduction is that using external electric field as the main energy source to induce redox reaction on electrodes (Figure 1.7.b). The H_2O is oxidized to produce oxygen and protons on anode. And the protons migrate to participate in CO_2 reduction on cathode through proton exchange membrane. The reaction process of electrocatalytic CO_2 reduction is controllable by adjusting voltage and reaction condition. Due to the sufficient electron source in the electrocatalytic reduction, it will simultaneously realize the multi electron reduction process, resulting in a variety of products. It should be noted that if the external voltage is too high, it will also lead to the competitive reaction of hydrogen evolution, which will lead to the reduction of Faraday efficiency of electrocatalytic CO_2 reduction. Moreover, the type of electrode or catalyst and the magnitude of external voltage would lead to the fact that the electrocatalytic reduction does not have absolute selectivity for a product, which usually includes a mixture of several substances[40]. Therefore, one of the main challenges is to improve product selectivity of electrocatalytic CO_2 reduction by optimizing the electrode or catalyst. At present, the technology of electrocatalytic CO_2 reduction is still not mature enough due to the obstacles such as low energy efficiency, poor reaction selectivity and total conversion rate.

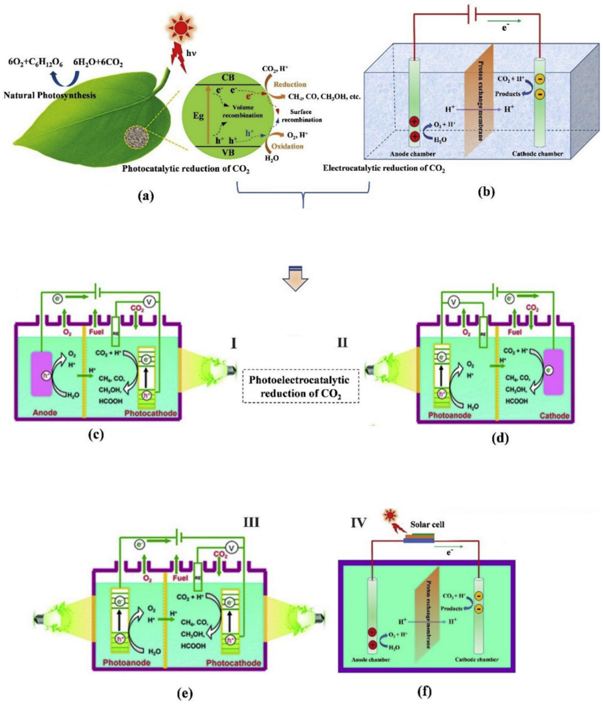

Figure 1.7: Basic principles of catalytic CO_2 reduction. (a) Analogy diagram of natural photosynthesis and schematic of photocatalytic CO_2 reduction. (b) Schematic diagrams for electrocatalytic CO_2 reduction system. Photoelectrocatalytic systems: (c) photocathode + dark anode, (d) dark cathode + photoanode, (e) photocathode + photoanode, (f) solar cell + electrodes [7]

1.7.4 Main systems and principle of photoelectrocatalytic CO_2 reduction

Due to the limitation of photocatalytic and electrocatalytic CO_2 reduction in practical application, the researchers combined the two technologies to develop photoelectrocatalytic (PEC) reduction of CO_2. The photoelectrocatalytic CO_2 reduction refers to the process that the semiconductor photoelectrode generates electrons by photoexcitation, and then the electrons migrate to the electrode surface under the guidance of external voltage to carry out the catalytic reduction of CO_2. The action of external electric field is helpful to promote the directional transfer of photogenerated electrons and holes, and thus enhancing the separation efficiency of photogenerated carriers to greatly improve the redox ability. Simultaneously, when the band position of photocatalyst is not conducive to CO_2 reduction and H_2O oxidation, the redox potentials can be adjusted by applying appropriate bias voltage in the photoreduction system. Compared to photocatalytic CO_2 reduction process, photoelectrocatalysis can realize the rapid transfer of electrons to reduce CO_2 on the photocathode at a lower overpotential, greatly enhancing reduction efficiency. Compared with single electrocatalysis, photoeletrocatalysis can use sunlight as the energy source to excite the generation of carriers, then participates in the oxidation-reduction reaction to finally realize the CO_2 reduction with low energy consumption. The whole process can reduce the input of external energy and realize the utilization of low-carbon clean and sustainable energy. The excellent photoelectrocatalytic CO_2 reduction system can not only use photocatalysis activity to excite and generate carriers under light conditions, effectively reducing the energy input of external electrons and energy consumption, but also use electrocatalytic activity to improve the electron-hole separation and transmission, greatly enhancing reduction efficiency. Most experiments of photoelectrocatalytic CO_2 reduction are mostly conducted in a three-electrode system including working electrode, counter electrode and reference electrode respectively. According to the different semiconductor materials of photoelectrode, the CO_2 reduction system can be divided into following categories (Figure 1.7c–e):

- dark anode and p-type photocathode
- dark cathode and n-type photoanode.
- P-type photocathode and n-type photoanode.

The p-type semiconductor photocathode not only works as a center of generating electrons and holes but also need to act as the catalyst for CO_2 activation to carry out reduction reaction. Generally, the p-type semiconductor photocathodes have negative CBs which are favourable for CO_2 reduction. But VB potentials of most p-type semiconductor are insufficient to oxidize water, which needs a higher bias potential generally to excite the reaction. Additionally, H_2 is usually generated with CO and HCOOH on p-type semiconductor photocathodes, affecting the selectivity of CO_2 reduction. The frequently-used p-type materials as photocathode including p-GaP, p-InP, p-CU_2O, p-CuO and p-CdTe, but which are generally expensive, toxic and/or unstable in aqueous solutions. Instead, the most n-type semiconductors (e.g., TiO_2, WO_3, ZnO, Fe_2O_3, and $BiVO_4$) that made of earth-abundant elements are generally low-toxic or nontoxic and/or also highly stable in aqueous solutions. Which makes the system (dark cathode and n-type photoanode) would be an attractive alternative. Furthermore, the combination of appropriate p-type and n-type semiconductors with matched band structure respectively as photocathode and photoanode to form Z-scheme heterojunction can realize efficient CO_2 reduction without external voltage. However, it is worth noting that not all of this kind PEC CO_2 reduction systems can avoid bias voltage. For instance, the system composed of an n-type TiO_2 photoanode and a p-type Si photocathode was still needed a bias voltage to promote CO_2 reduction. Additionally, a novel tandem device is developed by integrating a solar cell for supplying external voltage to promote CO_2 reduction reaction (Figure 1.7.f), also showing the excellent efficiency and promising potential. When the external bias voltage generated by the solar cell is high enough, the system can realize the unassisted CO_2 reduction and avoid the strict conditions that needs to form Z-scheme heterojunction. Recently, some researchers considered the challenges of CO_2 conversion in traditional aqueous solution such as serious mass transfer limitation stemmed from low solubility and slow diffusion of raw material CO_2 in water, developing a continuous-flow system for PEC CO_2 reduction by direct introduction of gas CO_2 onto the surface of catalysts, as shown in Figure 1.8. This new system shows an obvious advantage is that no limitations in CO_2 concentration exist due to solubility and diffusion through the double layer and competitive chemisorption of water is largely reduced.[41, 42, 43]

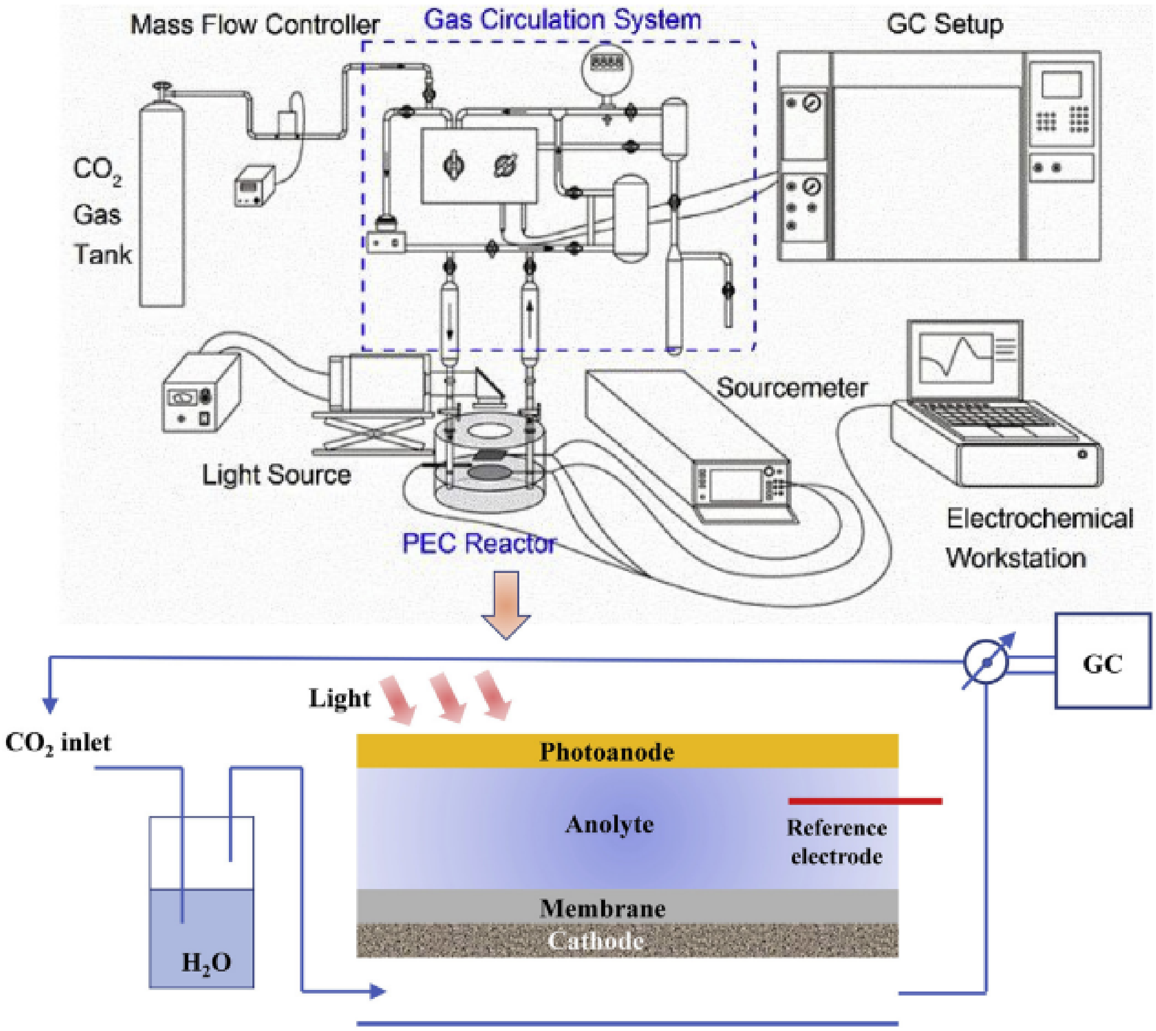

Figure 1.8: Continuous-flow PEC CO_2 reduction system [7]

1.7.5 Evaluation parameters for photoelectrocatalytic CO_2 reduction

The evaluation parameters for photocatalysis and electrocatalysis can combine to assess photoeletrocatalytic CO_2 reduction, as shown in Figure 1.9. Which mainly include product conversion rate, catalytic current density, turnover number (TON), turnover frequency (TOF), quantum yield (QY) and Faradaic efficiency (FE). The product conversion rate is generally calculated the yield per hour of per unit mass or per unit area on photoelectrode. The catalytic current density is also an important index to evaluate the reaction efficiency, which needs to be compared with the reference electrode (RE). TON and TOF can reflect the activity of catalytic active centers. The utilization and conversion efficiency of solar energy can be evaluated by calculating the QY. Additionally, the product selectivity can be assessed by calculating FE [44, 45].

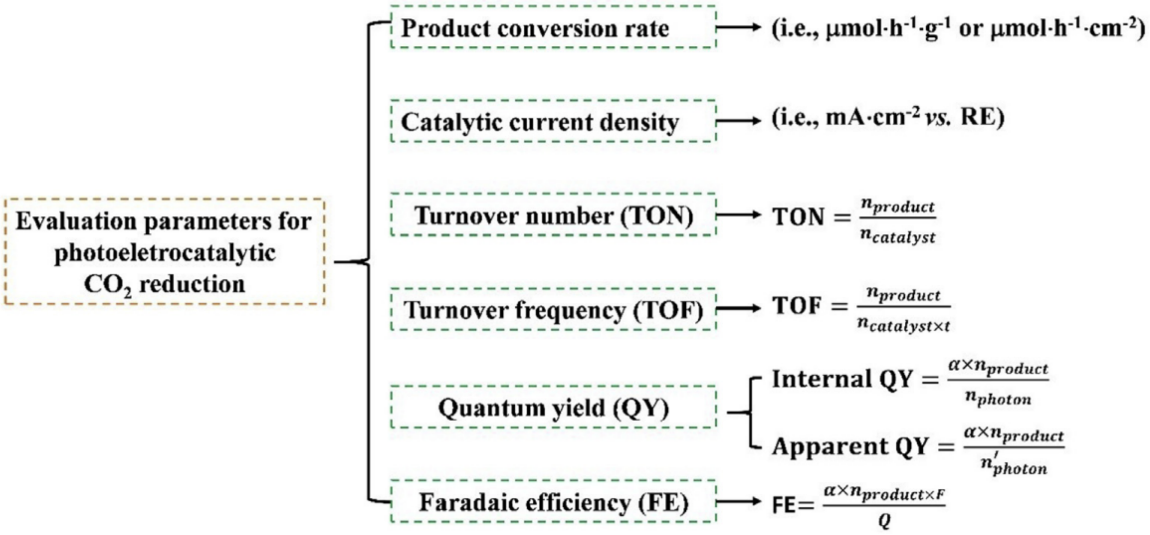

Figure 1.9: Schematic diagram of evaluation parameters for photoelectrocatalytic CO_2 reduction. [7]

1.8 Timeline of the development of electrolysis

1.8.1 Early Foundations of Electrolysis (18th - 19th Century)

The initial observation of the electrolysis phenomenon was made in 1785 by Martinus van Marum, who unintentionally triggered chemical reactions using an electrostatic generator. Although this instance signified the preliminary acknowledgment of electricity's capacity to facilitate chemical transformations, it lacked an underpinning theoretical framework. The authentic inception of electrochemistry transpired in 1800 when William Nicholson and Anthony Carlisle, capitalizing on Alessandro Volta's voltaic pile, successfully accomplished the electrolysis of water, resulting in its decomposition into hydrogen and oxygen. Johann Ritter independently performed analogous experiments, further substantiating the notion that electrical energy could catalyze chemical reactions [46, 47].

The creation of the voltaic pile represented a significant milestone by delivering a sustained electrical current, which was essential for methodical electrochemical explorations. Sir Humphry Davy subsequently employed this innovation to isolate highly reactive alkali metals such as potassium and sodium through electrolysis, thereby exemplifying the practical applicability of this methodology. This epoch also witnessed the formulation of Faraday's laws of electrolysis (1834), which established the quantitative correlation between the mass of substance deposited at an electrode and the total amount of electric charge traversing the electrolyte. These fundamental principles established the foundation for comprehending more intricate electrochemical processes, including the reduction of CO_2 [47].

1.8.2 First CO_2 Electrolysis Experiments (Mid-19th Century - Early 20th Century)

The inaugural documented endeavors to electrochemically reduce CO_2 can be traced back to the 19th century, coinciding with the emergent comprehension of electrochemical reactions. These preliminary experiments predominantly yielded carbon monoxide (CO) through the use of metallic cathodes, commonly zinc and copper, illustrating the simplicity inherent in the reaction pathways enabled by the catalysts available at that time.

Investigations during this period were primarily exploratory, constrained by a limited understanding of reaction mechanisms and the inherent challenge of overcoming CO_2's considerable thermodynamic stability. Notwithstanding these restrictions, these initial inquiries validated the fundamental feasibility of converting CO_2 into carbon-based products, albeit characterized by low efficiency and selectivity [46].

1.8.3 The Emergence of Catalyst Development (Early to Mid-20th Century)

The subsequent significant advancement in CO_2 electrolysis research transpired during the early to mid-20th century, propelled by progress in materials science and electrochemical methodologies. Researchers commenced systematic evaluations of various metallic electrodes, including silver, gold, platinum, and tin, for their catalytic efficacy.

One of the principal challenges during this timeframe was the management of elevated overpotentials and the attenuation of the hydrogen evolution reaction (HER), which frequently overshadowed CO_2 reduction processes. Investigative efforts revealed that silver and gold were conducive to the generation of CO, while tin exhibited a tendency to yield formate. These discoveries were crucial in recognizing that the choice of catalyst material significantly impacts product distribution and overall efficiency [13].

1.8.4 The Impact of the Energy Crisis (1970s - 1990s)

The global energy crises of the 1970s incited a resurgence of interest in alternative energy technologies, including CO_2 electroreduction. The investigation of semiconductor photoelectrodes emerged as a promising avenue, aiming to harness solar energy to diminish the electrical input requisite for CO_2 conversion. Semiconductor materials, including p-type GaP, GaAs, InP, CdTe, and Si, have been meticulously examined for their photoelectrochemical (PEC) properties. Upon exposure to illumination, these materials produced electron-hole pairs that facilitated the reduction of CO_2 into various products such as formic acid, formaldehyde, methanol, and carbon monoxide. Notwithstanding the promising theoretical frameworks, obstacles pertaining to efficiency, selectivity, and stability have impeded the widespread deployment of these technologies.

This era also witnessed the integration of gas diffusion electrodes (GDEs), which markedly enhanced the mass transport of CO_2 towards catalytic sites, thereby mitigating the solubility constraints associated with aqueous electrolysis. The combination of GDEs with flow cell architectures enabled the attainment of elevated current densities and augmented product yields [48].

1.8.5 Advancements in Catalysis and Reactor Design (Late 20th Century - Early 21st Century)

As the transition to the late 20th and early 21st centuries occurred, the domain of nanotechnology exerted a profound influence on the research surrounding CO_2 reduction. The inception of nanostructured catalysts, encompassing metal nanoparticles and carbon nanotubes, facilitated a substantial enhancement in catalytic surface area and improved electron transfer kinetics. These materials demonstrated superior efficiency and selectivity, attributable to their tailored electronic characteristics and high surface-area-to-volume ratios.

Reactor designs underwent significant evolution, incorporating membrane electrode assemblies (MEAs) to preserve ionic conductivity while facilitating efficient gas delivery. This technological advancement effectively addressed mass transport challenges while enabling continuous operation under conditions pertinent to industrial applications [13].

1.8.6 Modern Breakthroughs and Mechanistic Insights (21st Century - Present)

In recent years, there has been a notable surge of interest in machine learning and data-driven methodologies for optimizing catalysts. By capitalizing on computational techniques, investigators are now able to forecast catalyst behavior and engineer novel materials with atomic-level precision.

Furthermore, in situ spectroscopic methodologies, such as Raman and X-ray photoelectron spectroscopy (XPS), have rendered unprecedented insights into reaction intermediates and mechanistic pathways. For instance, surface-enhanced Raman spectroscopy (SERS) has successfully identified pivotal intermediates such as *COOH and *CO, elucidating pathways for the formation of multi-carbon products. Pioneering research continues to delve into the realm of single-atom catalysts (SACs) and metal-organic frameworks (MOFs) with the objective of achieving enhanced selectivity for multicarbon products such as ethylene and ethanol. These advanced materials, in conjunction with solid oxide electrolyzer cells (SOECs) designed for high-temperature CO_2 reduction, exemplify the transition from proof-of-concept investigations to practical and scalable implementations [49].

1.9 Factors influencing $\mathrm{CO_2}$ photocatalysis

The photocatalytic reduction of $\mathrm{CO_2}$ constitutes a highly promising methodology for alleviating GHG emissions while concurrently producing value-added chemical products. Photocatalysts are nanoparticles (NPs) with semiconducting features such as light absorption, charge transfer, and favourable electronic structure, among others. Photoactive NPs serve as catalysts in a variety of applications, including sustainable energy production and environmental remediation. When compared with bulk materials, photocatalysts have exceptional structures and a higher surface area to volume ratio, which boosts their actions. As a result, controlling the shape and size of photocatalytic materials in the nanoscale range allows for the creation and fabrication of materials appropriate for use in innovative applications.[50]

1.9.1 Metals for $\mathrm{CO_2}$ Photoreduction

Up to now, $\mathrm{CO_2}$ reduction catalysts could be divided into two categories: precious metal-based catalysts and precious metal-free catalysts. The precious metal-based catalysts showed excellent stability and redox properties in photocatalytic $\mathrm{CO_2}$ reduction, such as Pt, Ag, Pd, Ru,Rh, Au, and alloys. These catalysts have been widely applied to improve the selectivity of photocatalytic $\mathrm{CO_2}$ reduction products. In addition, the exposed crystal surface, particle size, and particle distribution greatly affect the activity and selectivity of photocatalytic CO_2 reduction. While the high cost of precious metal catalysts has limited their development for industrial applications, the search for low-cost, high-activity catalysts has become the focus of current research. The precious metal-free catalysts include Cu/CU_2O/CuO, Fe/Fe_2O_3, Ni/NiO, co-incorporated metal-organic framework , and carbon nanomaterials. Cu/Cu2O/CuO was recognized as an excellent catalyst with high activity.

1.9.1.1 Catalytic Reduction of CO_2 Reaction Mechanism

Due to the linear structure of CO_2, the energy required to cleave the C–O bond was much higher than that required to cleave the C–C, C–O, and C–H bonds. In addition, the relatively wide energy gap and electron affinity of CO_2 to a negative single-electron transfer redox potential. Therefore, different reaction pathways have been developed to reduce CO_2 at lower energies. In general, the photocatalytic CO_2 reduction process must follow the following four steps:

- the electrons on the photocatalyst VB are stimulated and transferred to its CB to generate a photogenerated charge, and the photogenerated charge could either be transferred separately to the photocatalyst surface for photocatalytic reaction or recombined to release photons or heat.
- the catalyst surface for CO_2 absorption.
- photogenerated electrons on the photocatalyst surface to convert CO_2 into fuel.
- desorption of photocatalyst products. A conductive potential that is more negative than the required standard potential and effective electron transfer to the CO_2-adsorbed semiconductor surface determine the efficiency of CO_2 reduction (Table 1.1).

Reaction	E^0_{redox} (vs. NHE)/V
$CO_2 + 2H^+ + 2e^- \rightarrow HCOOH$	-0.61
$CO_2 + 2H^+ + 2e^- \rightarrow CO + H_2O$	-0.53
$CO_2 + 4H^+ + 4e^- \rightarrow HCHO + H_2O$	-0.48
$CO_2 + 4H^+ + 4e^- \rightarrow CH_4 + 2H_2O$	-0.20
$CO_2 + 6H^+ + 6e^- \rightarrow CH_3OH + H_2O$	-0.38
$CO_2 + 8H^+ + 8e^- \rightarrow CH_4 + 2H_2O$	-0.24
$2CO_2 + 12H^+ + 12e^- \rightarrow C_2H_4 + 4H_2O$	-0.34
$2CO_2 + 12H^+ + 12e^- \rightarrow C_2H_5OH + 3H_2O$	-0.33
$2CO_2 + 14H^+ + 14e^- \rightarrow HCOOH + C_2H_6$	-0.27
$2H^+ + 2e^- \rightarrow H_2$	-0.42

Table 1.1: Different reduction products obtained from the photocatalytic reduction of CO_2 in an aqueous solution and the corresponding electrode potentials (vs. standard hydrogen electrode, 25 °C, pH = 7).[1]

The products obtained change with the change of reaction conditions and catalytic materials during the reduction process. The photon energy required for photoexcitation depends on the band gap of the photocatalyst. The edge position of the photocatalyst's energy band should match the relevant reaction's redox potential. The different reduction products and corresponding electrode potentials obtained from the photocatalytic reduction reaction of CO_2 in an aqueous solution are shown in Table 1.1. The ideal CO_2 photocatalytic reduction reaction must meet the requirement that the CB potential of photogenerated electrons is more negative than the potential of the reduction products/CO_2 (CH_4/CO_2, CH_3OH/CO_2, $HCHO/CO_2$, $HCOOH/CO_2$, or CO/CO_2), and the VB that generates holes is corrected than the potential of the oxidation reaction (O_2/H2O) of H_2O. To sum up, photocatalytic reduction of CO_2 must meet two conditions:

- photon energy is greater than or equal to band gap energy.
- The CB potential is more negative than the surface electron acceptor potential, and the VB potential is corrected than the surface electron donor potential.

In this way, the reaction process of photocatalytic reduction of CO_2 can be realized.

1.9.1.2 Mechanistic Role of Co-Catalysts in CO_2 Photocatalytic Reduction

In the process of photocatalytic CO_2 reduction, the co-catalyst plays three critical roles in participating in the reaction as follows:

- co-catalysts could reduce the activation energy or the reaction barrier on the semiconductor surface.
- co-catalysts could rapidly separate and migrate holes and electron pairs on semiconductor surfaces.
- co-catalysts could inhibit the side reactions in the photocatalytic reduction of CO_2 and improve the selectivity of the target product.

Photoexcited electrons could migrate through the photocatalyst conduction band to the co-catalyst surface to reduce CO_2 to CO, HCOOH, HCHO, CH_3OH, and CH_4 (from Figure 1.10). The excellent heterojunction structure between the co-catalyst and the semiconductor is vital for enhancing the migration of photogenerated carriers from the semiconductor to the co-catalyst.

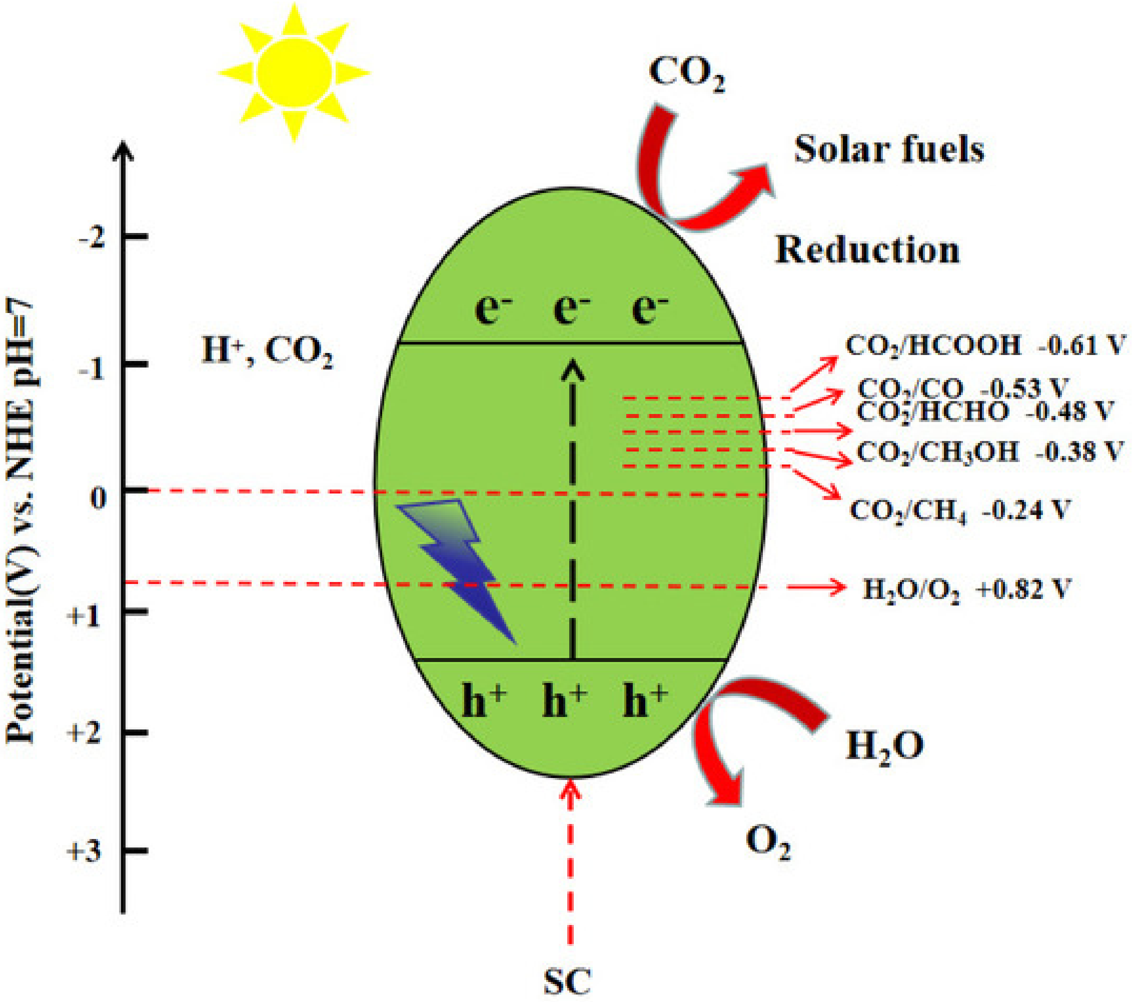

Figure 1.10: Mechanism of photocatalytic CO_2 reduction. [8]

In the process of photocatalytic CO_2 reduction, many factors affect the activity of the co-catalyst. For instance, elemental composition, crystal structure, exposed crystalline surface, and particle size. Excessive co-catalysts could have the following three problems:

- Excess co-catalyst could cover the active sites on the semiconductor surface and hinder the reduction of CO_2.
- Excess co-catalysts block sunlight and reduce light absorption, thus reducing the number of hole–electron pairs.
- Excessive amount of co-catalyst could cover the semiconductor surface unevenly, resulting in a larger catalyst size and thus lower catalytic activity. Therefore, finding the optimal amount of co-catalyst addition is necessary to maximize the photocatalyst activity.

1.9.1.3 Noble Metal-Based Co-Catalysts

Precious metal-based co-catalysts, such as Pt, Ag, Pd, Rh, Au, and alloys, have successfully improved the activity and selectivity of target products for photocatalytic CO_2 reduction in a range of photocatalyst systems. Noble metal co-catalysts improve the photocatalytic efficiency and enhance the selectivity of target products in the photocatalytic reduction of CO_2. However, the high cost of the precious metal itself limits its industrial development process.

▷ Pt-Based Co-Catalysts for Photocatalytic CO_2 Reduction:

Platinum (Pt) is a highly effective co-catalyst for photocatalytic CO_2 reduction due to its high work function (5.65 eV), which enhances electron extraction from semiconductors like TiO_2, improving charge separation and CH_4 production. Optimal Pt loading (0.2–0.6 wt%) maximizes activity, while excessive amounts lead to agglomeration and reduced efficiency. Compared to other noble metals (Au, Ag, Pd), Pt shows superior CH_4 selectivity but suffers from high cost and competing H_2 production. Methods like in situ synthesis, impregnation, and microwave-assisted deposition control Pt dispersion, with smaller nanoparticles (3–5 nm) offering the best performance.

- **Performance:**
  - ∗ Noble metals follow activity order: Pt > Pd > Au > Rh > Ag for CH_4 production.
  - ∗ Pt-loaded TiO_2 nanotubes (NTAs) achieve 25 ppm CH_4 vs. 3 ppm for pure TiO_2 under visible light.
  - ∗ Pt downside is that it promotes H_2O reduction to H_2, reducing CO_2 selectivity (56% → 39–45%).

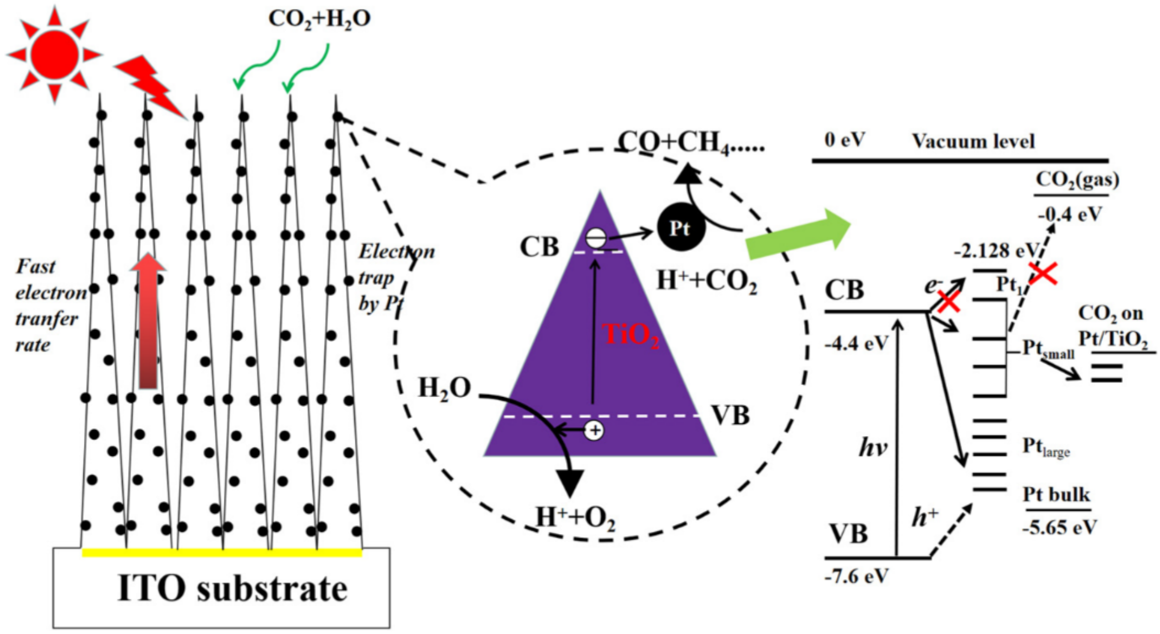

Figure 1.11: Mechanism diagram of CO_2 reduction by Pt-TiO2 photocatalyst. [9]

▷ Ag-Based Co-Catalysts:

Silver's low CO binding energy enhances CO desorption and selectivity in CO_2 reduction. At 5 wt% loading, Ag clusters form Schottky barriers that extend charge carrier lifetimes. The liquid-phase reduction method produces well-dispersed Ag nanoparticles that efficiently convert CO_2 to CO.

▷ Pd-Based Co-Catalysts:

Pd's crystalline structure significantly influences its CO_2 reduction performance. When supported on g-C_3N_4, Pd nanotubes demonstrated 80% product selectivity, far exceeding the 20% selectivity of Pd nanocrystals. DFT analysis verified the superior charge separation in nanotube configurations. Furthermore, researchers developed an efficient Nafion-coated Pd-TiO_2 photocatalyst capable of methane production.

- ▷ **Ru-Based Co-Catalysts:**

  Research has shown that the metal ruthenium (Ru) co-catalyst is capable of reducing carbon dioxide (CO_2). Baran et al. [51] successfully deposited Ru with a mass fraction of 1.0 onto the surface of nanocrystalline zinc sulfide (ZnS) through an impregnation process. The enhanced performance of Ru-loaded co-catalysts can be attributed to two primary factors:

  - ∗ the adsorption of photoexcited electrons by Ru, which improves charge separation efficiency,
  - ∗ the increased adsorption of CO_2 facilitated by Ru-loaded ZnS.

- ▷ **Alloy co-catalysts:**

  Au/Cu and Cu/Pt enhance photocatalytic CO_2 reduction. A 1.5% Au/Cu (1:2 ratio) on TiO_2 showed 97% CH_4 selectivity by facilitating electron transfer. Similarly, Cu/Pt on TiO_2 nanotubes achieved high hydrocarbon yields under solar light.

1.9.1.4 Non-Precious Metal Co-Catalysts:

- ▷ **Cu-Based Co-Catalysts:**

  Cu_2O clusters function as effective electron traps, significantly reducing charge recombination in photocatalytic systems. When loaded onto TiO_2, copper-based catalysts demonstrate superior performance for methanol (CH_3OH) production compared to silver-modified TiO_2, with isolated Cu(I) species identified as the primary active sites driving the reaction.

- ▷ **Ni-Based Co-Catalysts:**

  Nickel oxide (NiO) supported on $InTaO_4$ enhances visible-light-driven methanol synthesis by efficiently extracting photogenerated electrons. This configuration improves charge separation and boosts catalytic activity for CO_2 reduction to CH_3OH.

- ▷ **Graphene-Based Co-Catalysts:**

  Graphene serves dual roles as an electron reservoir (suppressing recombination) and a cocatalyst support. For example, reduced graphene oxide (RGO) combined with Pt-TiO_2 significantly increases methane yield (10.96 µmol m^{-2}) by improving charge transfer and active site dispersion.[52]

1.9.2 Semiconductors for CO_2 photoreduction

1.9.2.1 Organic semiconducting materials

Organic semiconducting materials represent a unique class of light-absorbing systems composed primarily of conjugated π-electron frameworks. Unlike their inorganic counterparts, these materials possess tunable optical and electronic properties governed by their molecular structure and substituent functional groups. Their low cost, solution processability, and synthetic modularity render them promising for sustainable energy conversion technologies, particularly in photoelectrocatalytic CO_2 reduction.

The performance of an organic semiconductor in CO_2 photoreduction is largely determined by its frontier molecular orbitals: the Highest Occupied Molecular Orbital (HOMO) and the

Lowest Unoccupied Molecular Orbital (LUMO). The position of the LUMO must be sufficiently negative relative to the reduction potential of CO_2 (e.g., $-0.52\,\mathrm{V}$ vs NHE for CO formation or $-0.38\,\mathrm{V}$ vs NHE for CH_3OH), enabling the thermodynamic feasibility of electron transfer to adsorbed CO_2 molecules.

Conjugated polymers such as polythiophene, poly(p-phenylene vinylene), and more notably polyaniline (PANI) have demonstrated visible-light responsiveness due to their extended π-systems. Their bandgaps (typically 1.5–2.8 eV) enable absorption in the visible range, facilitating solar energy harvesting.

From a charge transport perspective, the electrical conductivity (σ) of these materials is defined by the classical relation:

$$\sigma = ne\mu$$

where n is the charge carrier density, e is the elementary charge, and μ is the carrier mobility. These parameters are strongly influenced by protonic doping, often achieved using mineral acids such as HCl, which modulates the oxidation state of the polymer backbone and enhances its polaronic conductivity. Moreover, the photophysical mechanism enabling CO_2 reduction involves the following stages:

1) **Photoexcitation** of the conjugated backbone to generate electron-hole pairs.
2) **Charge separation** and directional transport of photogenerated electrons toward the polymer-electrolyte interface.
3) **Electrocatalytic reduction** of CO_2 via multi-step electron and proton transfer reactions.
4) **Product formation**, typically yielding alcohols or carbonyl compounds depending on selectivity and local environment.

What distinguishes organic semiconductors from many inorganic oxides is their structural flexibility and functionalizability, which can be exploited to incorporate co-catalysts or create heterojunctions for improved charge separation and catalytic selectivity. For instance, anchoring metal nanoparticles (e.g., Cu, Zn) onto PANI chains not only introduces new catalytic sites but also enhances interfacial electron mobility due to synergistic interactions between the π- conjugated network and the metallic domains .

1.9.3 Polyaniline

Polyaniline (PANI), one of the most prominent members of the family of intrinsically conducting polymers (ICPs), has the ability, after doping, to present a semi-conducting behavior due to its exceptional electronic, electrochemical, and physicochemical properties. Discovered in the 19th century, its potential was only fully realized in the 1980s when its protonated emeraldine form was identified as electrically conductive [53].

PANI is particularly attractive for energy and environmental applications due to:

- Its tunable electrical conductivity,
- environmental stability,

- low cost and ease of synthesis,
- reversible redox behavior, and facile doping/dedoping mechanisms.

These properties are closely related to the polymer's conjugated backbone, redox state, and protonation level. As such, it has found use in sensors, supercapacitors, batteries, corrosion protection, and more recently, as a highly promising catalyst support in **photoelectrocatalysis**.

1.9.3.1 Molecular structure and redox states of PANI

The fundamental backbone of polyaniline consists of repeating units derived from aniline ($C_6H_5NH_2$), linked through para-positioned nitrogen atoms. The general formula of a PANI chain can be written as:

$$[-\mathrm{C_6H_4} - \mathrm{NH}-]_n\,[-\mathrm{C_6H_4} = \mathrm{N}-]_m$$

Here, n and m define the ratio of reduced (amine, -NH-) to oxidized (imine, =N-) units, which determines the oxidation state of the polymer. The sum $n + m = 1$, and the degree of polymerization x typically ranges from tens to hundreds of repeating units [54].

PANI consists of monomer units built from reduced (y) and oxidized ($1 - y$) blocks and can exist in three well-defined oxidation states:

- **Leucoemeraldine (fully reduced, ($y = 1$)):** composed entirely of amine units, white to colorless in appearance, and electrically insulating.
- **Emeraldine base (EB) (half-oxidized, ($y = 0.5$)):** the most stable and technologically useful form, containing equal amounts of amine and imine groups; exhibits high conductivity upon protonic doping.
- **Pernigraniline (fully oxidized, ($y = 0$)):** composed entirely of imine units, violet in color, and non-conductive in its base form.

These transitions between redox states are reversible and can be induced chemically or electrochemically, which is essential for their function in redox catalysis. Upon protonic doping (typically with acids like HCl), the emeraldine base is converted to emeraldine salt (ES), introducing mobile charge carriers (polarons and bipolarons), thereby increasing its electrical conductivity by several orders of magnitude, from $\sim 10^{-6}$ S/cm (EB) to ~ 10 S/cm (ES) [55].

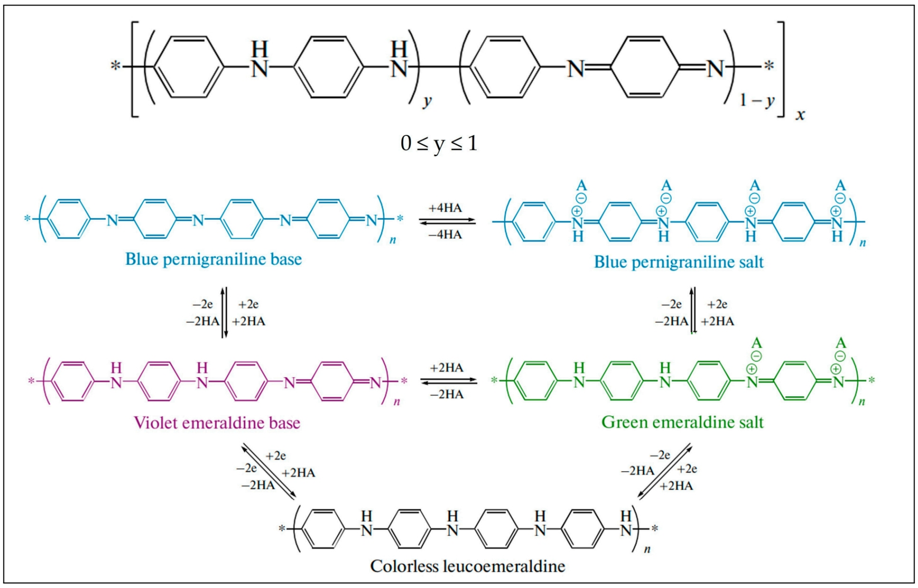

Figure 1.12: Chemical structure and redox forms of PANI [10].

The emeraldine salt possesses a bandgap in the range of 2.5 − 3.2 eV and exhibits **p-type** semiconducting behavior, making it suitable for visible-light-driven photocatalytic applications.

1.9.3.2 Theoretical considerations of PANI's synthesis

The synthesis of PANI constitutes a crucial step in tailoring its physicochemical properties, including morphology, oxidation state, chain length, and dopant incorporation — all of which significantly influence its electrocatalytic activity. Two principal routes have been extensively developed and refined over the past decades: **chemical oxidative polymerization** and **electrochemical polymerization**. Each method enables control over the final polymer's structure–function relationships, but through distinct mechanisms.

1.9.3.2.1 Chemical oxidative polymerization

This method involves the oxidation of aniline monomers in an acidic aqueous or organic medium using a strong oxidizing agent, typically ammonium persulfate (APS) according to [56]:

$$\text{Aniline} + \text{Oxidant} + \text{Acid} \rightarrow \text{PANI salt} + \text{by-products}$$

The reaction proceeds via a radical cation mechanism, with oxidative coupling at the para position, forming linear PANI chains. Key parameters such as **oxidant-to-monomer ratio**, **reaction pH**, **temperature**, and **dopant type** directly impact molecular weight, chain regularity, and doping level. The process is scalable, cost-effective, and particularly suited for bulk powder production.

1.9.3.2.2 Electrochemical polymerization

Electrochemical synthesis is especially relevant in applications involving PANI-based electrodes. It is conducted in a three-electrode configuration, immersed in an acidic electrolyte containing the aniline monomer. The polymerization is driven by cyclic voltammetry (CV), potentiostatic, or galvanostatic techniques. The resulting polymer morphology, redox behavior, and catalytic performance are critically shaped by several electrochemical parameters [19]:

- **Electrolyte pH and acid nature:** Strongly acidic environments ($pH < 2$) are essential to stabilize radical intermediates and maintain the polymer in its protonated (conducting) form.
- **Monomer concentration:** Excessive concentrations may lead to poor film uniformity and dense agglomeration.
- **Scan rate:** A low scan rate (e.g., 10–20 mV/s) favors a gradual and uniform film growth. Faster rates can cause non-uniform deposition and partial doping.
- **Number of cycles:** Determines the film thickness. While more cycles increase electroactive area, excessively thick layers can hinder charge transport and light absorption.
- **Nature and surface state of the working electrode:** Highly polished or pretreated substrates with good surface energy promote homogeneous nucleation and strong adherence of the polymer film.

1.9.3.3 Doping mechanism and charge transport in PANI

One of the most distinguishing features of PANI is its ability to be chemically or electrochemically **doped**, transitioning from an insulating to a conducting state. Doping in PANI is not achieved by traditional charge transfer (as in inorganic semiconductors), but rather by protonation of the imine nitrogen atoms in the polymer backbone in the presence of an acid.

$$\text{PANI (emeraldine base)} + H^+ \rightarrow \text{PANI (emeraldine salt)}$$

Protonic acids like HCl introduce localized positive charges along the conjugated chain, creating delocalized charge carriers, specifically: **polarons** (singly charged radical cations) and **bipolarons** (doubly charged species). These defect structures facilitate intra- and inter-chain hopping mechanisms, leading to metallic-like conductivity ($\sim 1 - 20$ S/cm) [11].

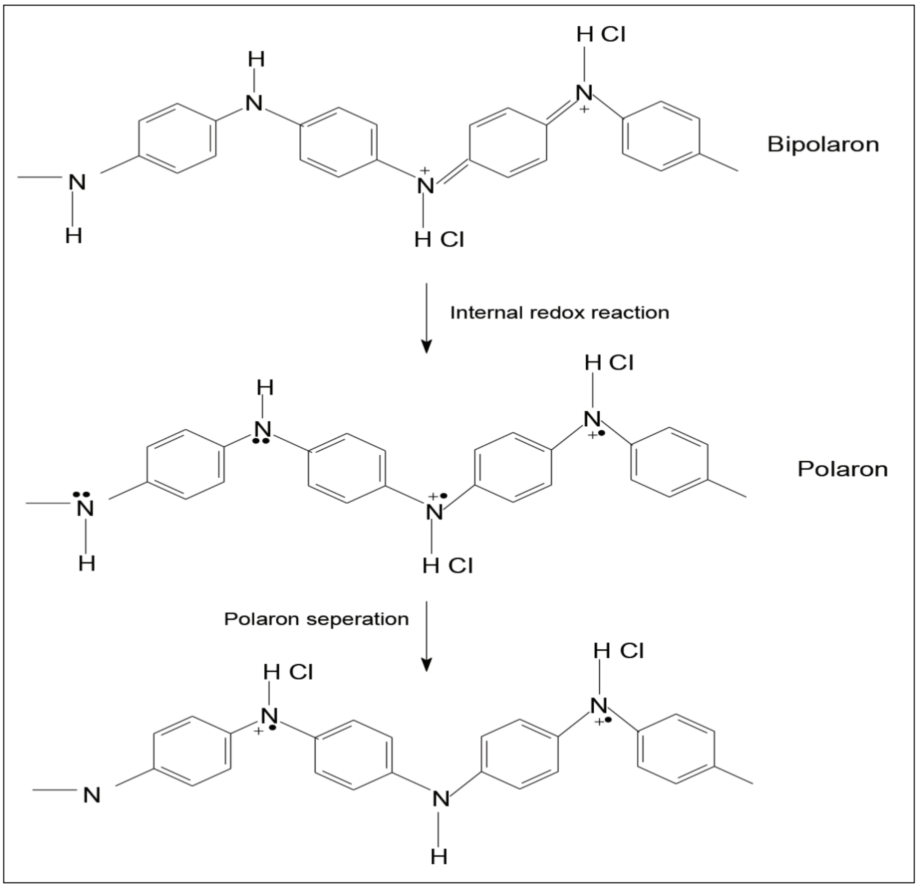

Figure 1.13: Electronic structure and charge carrier formation (polaron, bipolaron) in doped PANI [11].

1.10 Reactors for CO_2 photoreduction

The design and configuration of photoreactors exert a significant influence on the efficiency and stability of CO_2 photoreduction systems. The architecture of the reactor impacts critical parameters including mass transport, light utilization, and catalyst longevity.

1.10.1 Reactor typologies and their implications

The most prevalent photoreactor configurations include **batch**, **continuous-flow**, and **recirculating** systems—each with inherent advantages and limitations.

- **Batch photoreactors** are simple to construct and operate, often used in early-stage photocatalyst testing. However, they suffer from severe mass transport limitations and poorly controlled irradiance fields. They often lead to extrinsic kinetic models dominated by non-participating gases and are generally unsuitable for reliable upscaling.
- **Continuous-flow photoreactors** offer superior control over temperature, gas flow, and reactant residence time. Their configuration mitigates concentration gradients and facilitates inline monitoring of photoreduction intermediates. Moreover, the improved gas–solid contact at the illuminated surface area yields a significantly higher proportion of effective reagent interactions, enhancing intrinsic kinetic fidelity.

- **Recirculating reactors** serve as an intermediate system, enhancing contact time and providing improved mixing, albeit at the cost of more complex control schemes and difficulty in isolating time-dependent kinetic data.

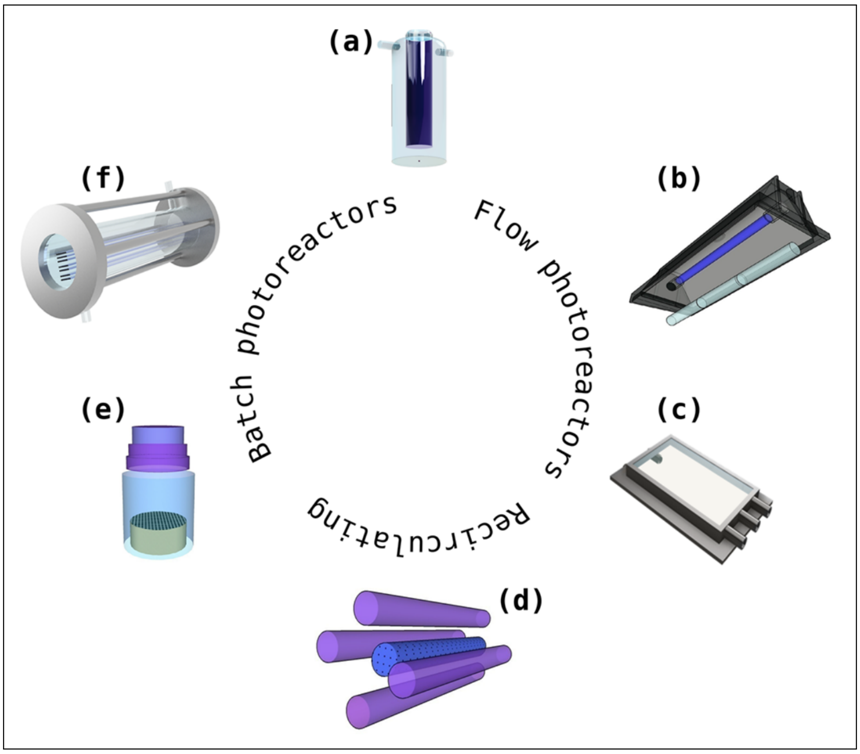

Figure 1.14: Representative configurations of photoreactors for CO_2 photoreduction: Batch (a, e, f), Flow (b, c), and Recirculating (d) systems [12].

1.10.2 Reactor Geometry and Light Distribution

The geometry of the reactor governs both the photonic and hydrodynamic environment. For instance, annular reactors with UV lamps centered in quartz sleeves are widely used; yet studies reveal that **non-annular geometries**—where the light source directly contacts the liquid surface—significantly outperform annular configurations. In particular, Koci et al. [45] reported that reducing the lamp-to-liquid surface distance from 5 cm to 2 cm increased the photoreduction yields of CH_4 and CH_3OH by 2.5× and 4×, respectively [12].

Photonic efficiency is further affected by the **distribution of the liquid phase volume**. Volumes exceeding the irradiated zone lead to inefficient light use, while insufficient volumes can limit catalyst suspension homogeneity. The requirement for **perfect mixing** is often unmet in laboratory-scale annular designs, which can result in sedimentation of photocatalyst particles and reduced reaction zones.

1.10.3 Twin reactor systems

Recent advancements propose the use of **twin photoreactors**, incorporating two distinct compartments (gas and liquid) separated by a Nafion membrane, each housing dedicated catalysts for water oxidation and CO_2 reduction respectively. This Z-scheme architecture allows for independent optimization of the thermodynamic and kinetic environments of each half-reaction, improving overall quantum efficiency and minimizing back reactions.

For instance, Wang et al. [37] demonstrated that separating CO_2 photoreduction from H_2 evolution spatially and catalytically enhanced both reaction rates and CO_2-to-CH_3OH yield by mitigating competitive processes and stabilizing electron transfer across phases.

1.10.4 Integration with PANI-based photoelectrodes

In the context of PANI-based photoelectrodes, specialized designs are required to maintain optimal interfacial contact and light penetration. The most suitable configurations include:

- **Three-electrode PEC cells** with a PANI working electrode illuminated through a quartz window.
- **Membrane-Electrode Assemblies (MEA)** to spatially separate oxidation and reduction half-cells while facilitating ionic transfer.
- **Gas Diffusion Electrode (GDE) architectures**, where the triple-phase boundary is directly accessible by gaseous CO_2, enhancing selectivity and desorption dynamics.

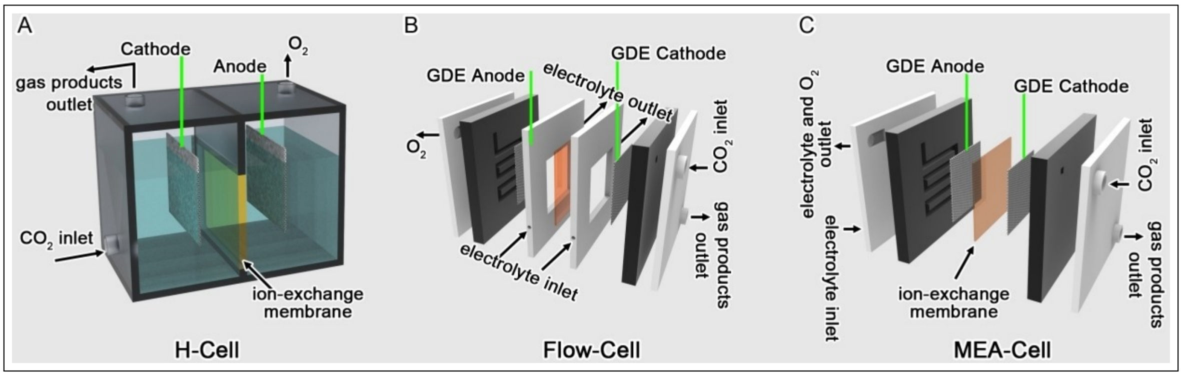

Figure 1.15: Typical electrochemical cell configurations for CO_2 reduction: (A) H-type Cell (Three-electrode PEC Cell), (B) Flow Cell (GDE architecture), and (C) MEA system [13].

1.11 Challenges of CO_2 electrolysis

Despite extensive progress in catalyst and system development, the practical implementation of CO_2 electrolysis remains hindered by interdependent challenges: selectivity, stability, and efficiency. These challenges are intimately tied to the nature of the catalyst, the electrolyte environment, mass transport limitations, and cell architecture.

1.11.1 Selectivity

In electrocatalytic CO_2 reduction (CO_2RR), selectivity denotes the system's capacity to steer the reaction pathway toward a specific product — CO, HCOOH, CH_4, C_2H_4, ethanol, etc. — over a range of competing and parallel pathways. From a mechanistic standpoint, it is the most challenging parameter to optimize due to the confluence of thermodynamics, surface kinetics, electronic structure of the catalyst, electrolyte environment, and mass transport effects. Crucially, selectivity must not be approached merely as a performance metric, but rather as a dynamic, multi-scale design criterion for any viable CO_2-to-chemical conversion system.

1.11.1.1 Thermodynamic and kinetic foundations

The electrochemical reduction of CO_2 encompasses a series of proton-coupled electron transfer (PCET) steps. Thermodynamically, these reactions are endergonic at standard conditions and require overpotentials to proceed at appreciable rates. Theoretical free energy changes for key two-electron products are [12]:

$$
\begin{aligned}
\mathrm{CO_2 + 2H^+ + 2e^- \rightarrow CO + H_2O} \quad & \Delta G^\circ \approx +257\ \mathrm{kJ/mol} \\
\mathrm{CO_2 + 2H^+ + 2e^- \rightarrow HCOOH} \quad & \Delta G^\circ \approx +174\ \mathrm{kJ/mol} \\
\mathrm{2H^+ + 2e^- \rightarrow H_2} \quad & \Delta G^\circ \approx 0\ \mathrm{kJ/mol}
\end{aligned}
$$

These values underscore why the hydrogen evolution reaction (HER) often dominates, particularly when protons or water are abundantly available and the catalyst lacks specificity for $^*CO_2$-derived intermediates.

The complexity of CO_2RR stems from the proximity of reaction intermediates on the energy landscape. Multiple products, such as CO, HCOOH, CH_4, and C_2H_4, proceed through shared or closely related adsorbed species (*COOH, *CO, *CHO). Consequently, fine control over adsorption energetics is essential.

1.11.1.2 Intermediate binding energetics

A pivotal criterion in designing selective catalysts is optimal binding strength for reaction intermediates. The Sabatier principle stipulates that the free energy of adsorption (ΔG_{ads}) of key species must lie within an optimal window: too weak leads to poor activation, while too strong causes poisoning or kinetic hindrance. Notably [57]:

- Au and Ag possess moderate *CO adsorption energies, thus favoring CO evolution with high Faradaic efficiency (FE up to 90%).
- Cu binds *CO strongly enough to enable C–C coupling, making it uniquely capable of generating multi-carbon products (C_2H_4, C_2H_5OH).
- Fe, Ni, and Pt exhibit strong hydrogen binding, thus favoring HER under identical conditions.

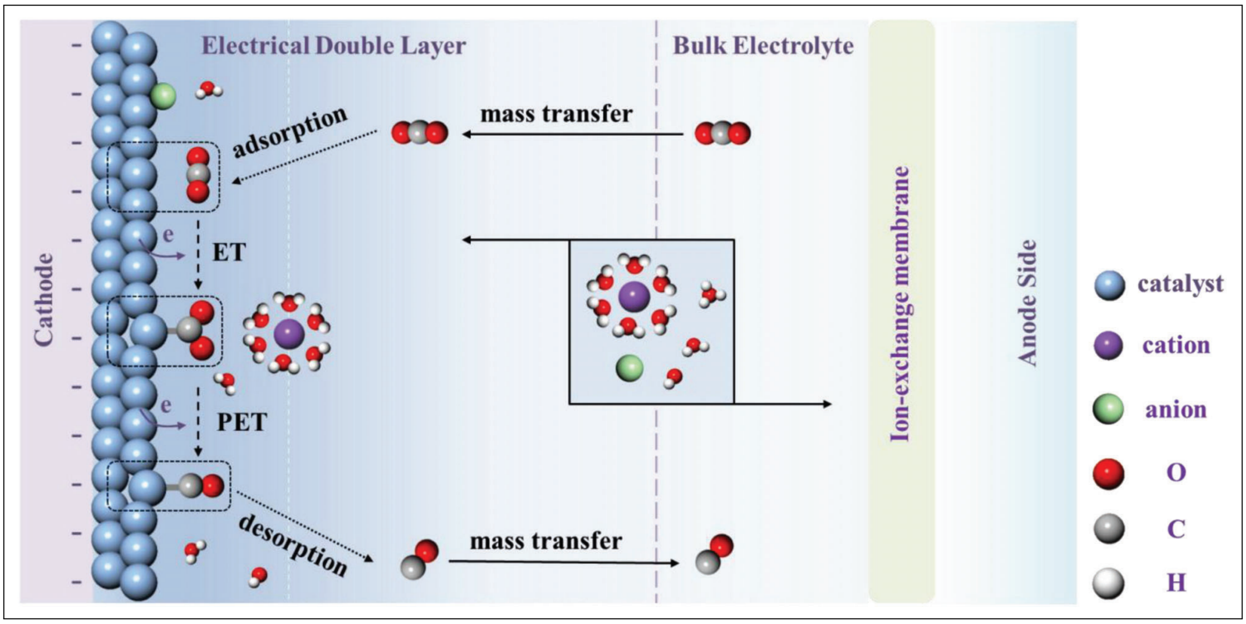

Figure 1.16: Schematic of a typical CO_2RR to CO process at electrochemical reaction interface (reaction microenvironment). ET means electron transfer, and PET means proton–electron transfer. The dashed box represents the evolution of the same active site at different stage of CO_2RR [14].

In this context, PANI-based systems offer a tunable platform: their redox-active imine/amine backbone modulates the electronic density of embedded catalytic sites, while the extended π-conjugation framework can stabilize transition states via electrostatic, π–π, or hydrogen bonding interactions. For instance, a Cu–PANI composite has been reported to shift *COOH binding by over 0.2 eV relative to bare Cu, thereby altering product selectivity toward HCOOH or ethanol [56].

1.11.1.3 Suppression of the Hydrogen Evolution Reaction

HER is a major competing pathway in aqueous electrolysis and poses a persistent challenge to selective CO_2RR. Strategies to suppress it include:

- Engineering hydrophobic catalyst layers to limit water availability,
- Local pH tuning to inhibit proton reduction,
- Introducing metal cations (e.g., K^+, Cs^+) to displace protons at the Helmholtz plane,
- Utilizing non-aqueous or metal-cation-free electrolytes.

Monteiro et al. [58] demonstrated nearly complete suppression of HER in acidic electrolytes by maintaining high local CO_2 availability and employing weakly hydrated cations (Cs^+), enabling CO FEs >90% at 100–200 mA·cm^{-2}. This is directly relevant to your work with photoactive polymer matrices: the hydrophilicity and ion transport characteristics of doped PANI films influence local proton activity and can be tuned to suppress HER in favor of CO_2RR.

1.11.1.4 Faradaic Efficiency and quantitative descriptors

Faradaic efficiency (FE) remains the principal metric for selectivity. For a given product i:

$$\mathrm{FE}_i = \frac{z_i n_i F}{Q_{\text{total}}} \times 100$$

Where:

- z_i = number of electrons required per mole of product i
- n_i = number of moles of product i formed
- F = Faraday constant
- Q_{total} = total charge passed during electrolysis

However, FE alone is insufficient. It should be correlated with turnover frequency (TOF), selectivity ratio (e.g., CO/H_2), and product distribution profiles over a range of potentials. This multi-metric approach is essential when evaluating polymer-based photocathodes, which can exhibit complex, light-modulated selectivity behaviors [13].

1.11.1.5 Selectivity modulation via PANI Matrix Engineering

PANI's functionality in CO_2RR selectivity extends beyond its conductivity. Its protonation state (ES vs. EB), dopant type, and morphological order (e.g., nanofibers, films, or composites) critically affect [53]:

- Local ionic conductivity and pH buffering,
- Adsorption strength of CO_2-derived intermediates,
- Stabilization of metal co-catalysts (e.g., Cu, Zn, Sn) via N coordination,
- Charge transfer dynamics at the electrode/electrolyte interface.

For instance, Zn-doped PANI exhibits enhanced selectivity toward HCOOH due to Zn's oxophilic nature and its ability to stabilize *OCHO intermediates. In contrast, Cu–PANI systems are more likely to favor CO or C_2+ products depending on the surface oxidation state and polymer–metal charge transfer dynamics.

Moreover, under illumination, photoexcited PANI generates localized electric fields and surface dipoles that modulate reaction pathways. While being absent in conventional electrocatalysts, these effects offer an underexplored route for enhancing selectivity through photochemical field-driven intermediate control.

1.11.2 Stability

It is fair to say that stability is not a monolithic descriptor but a multi-scale property emerging from the interplay between active site robustness, structural integrity of the catalyst matrix, the evolution of the electrochemical microenvironment, and the mechanical and chemical endurance of the overall device.

1.11.2.1 Mechanisms of catalyst and electrode degradation

(i) Intrinsic Degradation of PANI Matrix

Polyaniline (PANI), owing to its π-conjugated backbone and variable oxidation states, undergoes repeated protonation/deprotonation and redox transitions during CO_2RR. This repeated cycling can result in [59]:

- Overoxidation and chain scission at anodic potentials > 0.8 V vs. RHE, leading to quinonoid formation, ring opening, and irreversible loss of conjugation and conductivity.
- Volume stress from hydration and swelling, especially under fluctuating local pH, causes mechanical delamination and microcracking.
- Redox hysteresis and electronic disorder from repeated electron transfers, leading to localized charge trapping and diminished conductivity over time.

These degradation modes are intensified in the presence of metal co-catalysts, as these can engage in redox transformations (e.g., $Cu^0 \leftrightarrow Cu^{2+}$), generating additional oxidative or coordinative stress on the polymer framework.

(ii) Atomic Migration and Surface Reconstruction

Metallic or single-atom catalytic centers embedded within or supported on PANI can undergo structural evolution driven by surface energy minimization and local potential fluctuations. According to thermodynamic analysis, the Gibbs free energy of a nanoparticle system is given by [41]:

$$G = H - TS + \gamma A$$

where γ is the surface energy and A the surface area. Nanoparticles with high curvature (e.g., < 20 nm) are thermodynamically unstable, prone to:

- Ostwald ripening and coalescence, reducing the number of catalytically active sites.
- Dissolution–redeposition cycles, particularly under open circuit or dynamic potential conditions.
- Elemental redistribution and detachment from supports, especially under long-term operation in flow cells.

(iii) Coordination Environment Breakdown

In metal–nitrogen–carbon (M–N–C) motifs (e.g., Fe–N_4 embedded in PANI), radical species or local alkalization can cause ligand displacement, converting single-atom active sites into inactive aggregates or leached ions [60].

5.2.2 Reaction Microenvironment and Electrolyte-Induced Destabilization

Beyond the catalyst, long-term operation of CO_2RR induces drastic local transformations at the electrode–electrolyte interface. These include [61]:

- **Carbonate precipitation:**

  $$CO_2 + OH^- \rightarrow HCO_3^-; \quad HCO_3^- + OH^- \rightarrow CO_3^{2-}$$

  leading to K_2CO_3 deposits that block pores and inhibit gas diffusion.
- **Electrolyte flooding**, especially in GDE-based systems, where loss of hydrophobicity allows water to replace gas at the triple-phase boundary (TPB), drastically reducing CO_2 availability.
- **Accumulation of reaction products and impurities**, including CO, alcohols, oligomers, and heavy metals (Fe^{2+}, Zn^{2+}), which adsorb irreversibly and poison active sites.
- **Bubbles and hydrodynamics** also play a crucial role: gas evolution can block reactive surfaces or alter pressure gradients, disturbing the interfacial electric field and mass transport dynamics.

1.11.2.2 Strategies for enhancing stability in PANI-based systems

Given these vulnerabilities, engineering durable PANI-based electrodes for CO_2RR demands a multifaceted approach [60]:

Molecular-level stabilization:

- Covalent grafting of PANI to substrates (e.g., FTO, carbon cloth, graphene oxide) reduces delamination.
- Copolymerization with hydrophobic moieties (e.g., fluorinated monomers) enhances resistance to overhydration and swelling.

Encapsulation of active sites:

- Use of thin protective layers (e.g., TiO_2, carbon shells) around metal nanoparticles preserves structure and prevents leaching, while allowing electron transfer.

- *Example:* Encapsulated Cu nanocrystals with Al_2O_3 demonstrate superior resistance to sintering and oxidation.

Reaction environment control:

- Employing buffer-rich or periodically refreshed electrolytes minimizes carbonate build-up.
- Use of alternating ON–OFF electrolysis regimes allows *in situ* reoxidation or surface healing of Cu, known to enhance selectivity toward C_2+ products.

Advanced electrolyte designs:

- Operating in acidic or solid-state media suppresses carbonate formation.
- Use of ionic liquids or hydrophobic electrolytes can improve interface stability and CO_2 solubility.

1.11.3 Efficiency

The efficiency of the electrochemical reduction of carbon dioxide (CO_2RR) encapsulates the interplay between thermodynamic driving force, kinetic selectivity, and systemic losses across the device architecture. At its core, efficiency is a multidimensional figure of merit, whose optimization is essential for transitioning laboratory-scale processes into economically viable and industrially scalable technologies.

Three primary metrics quantify this efficiency: Faradaic efficiency (FE), current density (j), and energy efficiency (EE). While Faradaic efficiency provides insights into selectivity, current density indicates catalytic activity, and energy efficiency (the most integrative metric) encompasses both, along with voltage losses in the system. A competitive CO_2RR system must meet all three criteria concurrently — a challenge exacerbated by the inherently low solubility of CO_2 in aqueous media ($\sim$33 mM at 25 °C and 1 atm), mass transport barriers, and competing reactions such as the hydrogen evolution reaction (HER) [37].

In polyaniline (PANI)-based photocathodes, FE is highly sensitive to the oxidation state and protonation degree of the polymer backbone. The emeraldine salt (ES) form exhibits optimal conductivity and redox activity, but its performance is susceptible to deprotonation at alkaline interfacial pH — a common occurrence under CO_2RR operation. This leads to a non-uniform spatial distribution of active sites, which reduces FE and promotes parasitic HER pathways.

1.11.3.1 Overpotential Challenges

The electrolyte environment plays a pivotal role. For example, systems operated in acidic media using Cs_2SO_4 (pH $\approx$ 4) showed a 30% higher energy efficiency compared to neutral $KHCO_3$, thanks to reduced ohmic resistance (234.4×10^{-4} S·m^2·mol^{-1}) and higher ionic conductivity. Monteiro *et al.* [58] demonstrated that switching from $KHCO_3$ to Cs_2SO_4 could save up to 1343 USD per ton of CO produced at 200 mA·cm^{-2}, based on electricity costs.

1.11.3.2 Current Density: A Bottleneck for Industrial Translation

While Faradaic efficiency (FE) assesses how effectively electrons are utilized, current density (j) quantifies the rate of product formation. Industrial feasibility mandates $j > 200$ mA·cm^{-2}, a threshold routinely unmet in classical H-type cells, where j often remains < 20 mA·cm^{-2}. Integration with gas diffusion electrodes (GDEs)—which operate at the triple-phase boundary—has enabled current densities up to 1 A·cm^{-2} in CO production, albeit at higher cell voltages and the risk of electrode flooding [62].

For PANI-based systems, the challenge lies in the intrinsic trade-off between polymer porosity (which aids ion transport) and hydrophilicity (which impedes CO_2 gas diffusion). Swelling-induced changes to the electrode morphology further complicate stable current delivery. Engineering hierarchical architectures — electrospun mats, 3D scaffolds, and hybrid supports — remains essential to maintain high j while preserving CO_2RR selectivity.

1.11.3.3 Strategies to Enhance Efficiency in PANI-Based Systems

To meet the simultaneous demands of high FE, j, and EE in PANI-based photocathodes, an integrative strategy is required [63]:

- **Electronic Band Alignment:** Co-polymerization with narrow-gap monomers or doping with heteroatoms (e.g., N, S, or P) to tune the HOMO–LUMO levels and improve electron injection toward CO_2RR potentials.
- **Metal Hybridization:** Incorporating Cu, Sn, or single-atom catalysts (e.g., Fe–N_4) into the PANI matrix to localize active sites and enhance multielectron transfer kinetics.
- **Photoelectrochemical Coupling:** Using PANI as a sensitizer or hole-transport layer in tandem cells (e.g., with $BiVO_4$ or TiO_2) to increase photon absorption and drive bias-free or low-bias CO_2RR.
- **Membrane Engineering:** Deployment of high-conductivity anion exchange membranes (AEMs) that minimize crossover, stabilize pH, and reduce parasitic voltage losses.
- **Reactor Design:** Using MEA (membrane electrode assembly) configurations shortens ionic pathways, minimizes ohmic losses, and enhances system-level EE and j.

These approaches must be validated using *operando* diagnostics — electrochemical impedance spectroscopy (EIS), *in situ* Raman, and transient photovoltage mapping — to correlate structural evolution with device performance across varying operating regimes.

Chapter 2

Experimental study

This chapter provides a concise overview of the experimental procedures, electrodes, and reagents employed in the development of the structures forming the basis of this study. We begin by detailing the processes used to prepare the graphite-based cathodes and the fabrication of thin films and catalyst pastes composed of doped polyaniline (PANI). This is followed by a brief description of the characterization tools and techniques used throughout this work, all directed toward the photoelectrochemical reduction of CO2 into value-added products.

2.1 Synthesis of PANI/C_{gr} structures

2.1.1 Substrate preparation

Graphite (Cgr) rods were used as conductive substrates. Large graphite rods were cut into cylindrical shapes measuring 9 cm in length and 1 cm in diameter using a metal saw. This step is illustrated in Figure 2.1.

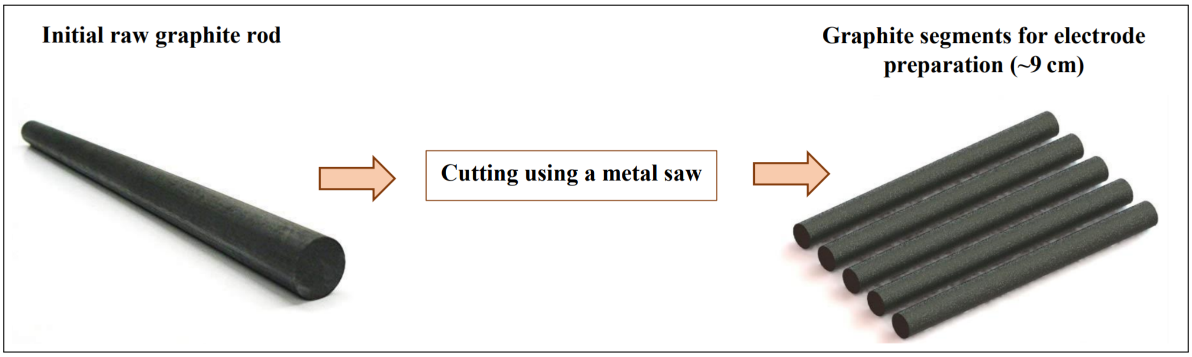

Figure 2.1: Cutting of graphite rods

2.1.2 Cleaning of the graphite substrates

Proper surface cleaning of the substrate is a critical step to eliminate any residual grease, dust, or surface contaminants before its use as a conductive support for cathode fabrication. This process is essential to ensure strong adhesion and uniform thickness of the deposited film. The cleaning procedure adopted was as follows:

1) Rinsing with soapy water;
2) Immersion in diluted nitric acid and ultrasonic agitation for 15–20 minutes;
3) Thorough rinsing with deionized water;
4) Ultrasonic cleaning in acetone for 15–20 minutes;
5) Ultrasonic cleaning in ethanol for 15–20 minutes;
6) Final rinsing with deionized water (EDI) for 15–20 minutes;
7) Drying under nitrogen gas flow (N_2).

After cleaning, the graphite substrates were ready to be used as conductive supports for catalyst deposition, specifically of HCl-doped polyaniline (PANI).

2.1.3 Preparation of thin films for electrodes

Two distinct fabrication methods were used for the preparation of PANI-based electrodes: a **chemical route** and an **electrochemical route**. Both approaches rely on the oxidative polymerization of aniline monomer in acidic media.

2.1.3.1 Electrochemical route

2.1.3.1.1 Electropolymerization

Polyaniline deposition was achieved via electropolymerization of the aniline monomer directly onto the graphite substrate surface. It's a process that involves the electrochemical oxidation via cyclic voltammetry (CV) which enables the formation of nanostructured PANI films (HCl-PANI/Cgr) with good homogeneity, adhesion, and reproducibility.
The CV experiments were conducted using an AUTOLAB potentiostat controlled via the NOVA 2.1 software, serving as the voltage source (Fig. 2.2). The electrochemical cell was composed of an aqueous electrolyte containing the monomer (aniline), the dopant (HCl), and the solvent (H_2O), arranged in a three-electrode configuration: the working electrode (C_{gr}), a reference electrode (Ag/AgCl), and a counter electrode (Pt wire). The CV was performed in the potential window of -0.2 V to $+1.0$ V vs Ag/AgCl, at a scan rate of 20 mV/s.

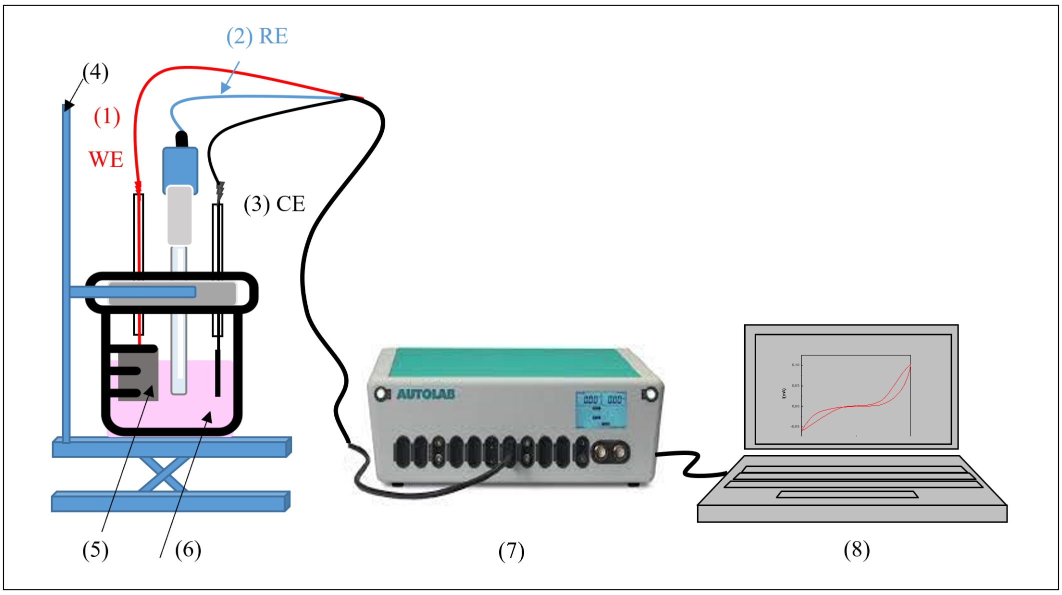

Figure 2.2: Experimental setup for electrochemical polymerization

1) Working electrode (C_{gr})
2) Reference electrode (Ag/AgCl)
3) Counter electrode (Pt)
4) Electrode support
5) Substrate surface for deposition
6) Electrolytic solution (HCl/aniline)
7) Autolab potentiostat/galvanostat
8) Laptop with NOVA software for control and data acquisition

2.1.3.1.2 Preparation of the Electrolyte Solution

The electrolyte solution used for PANI electropolymerization was composed of:

- **Aniline monomer** (0.2 M), molecular formula: $C_6H_5NH_2$;
- **Solvent:** Deionized water (H_2O);
- **Dopant:** Hydrochloric acid (HCl, 0.5 M).

Figure 2.3: Preparation of the electrolyte solution

2.1.3.1.3 Surface modification of the substrates by copper(I) oxide (Cu_2O) deposition

Inside an analytical balance, exactly 4 g of copper(II) sulfate ($CuSO_4$) is weighed and carefully transferred into a beaker using a spatula. This mass is then poured into a 50 mL volumetric flask and diluted to the calibration mark with deionized water (EDI). The mixture is stirred thoroughly to obtain a homogeneous electrolyte solution.

The Cu_2O deposition is carried out using a standard three-electrode electrochemical setup, consisting of a working electrode (graphite substrate), a 0.5 M $CuSO_4$ electrolyte solution, and a potentiostat/galvanostat to apply a current density of 1.5 $mA \cdot cm^{-2}$ for a duration of 100 seconds. The entire setup is connected as illustrated in the following figure:

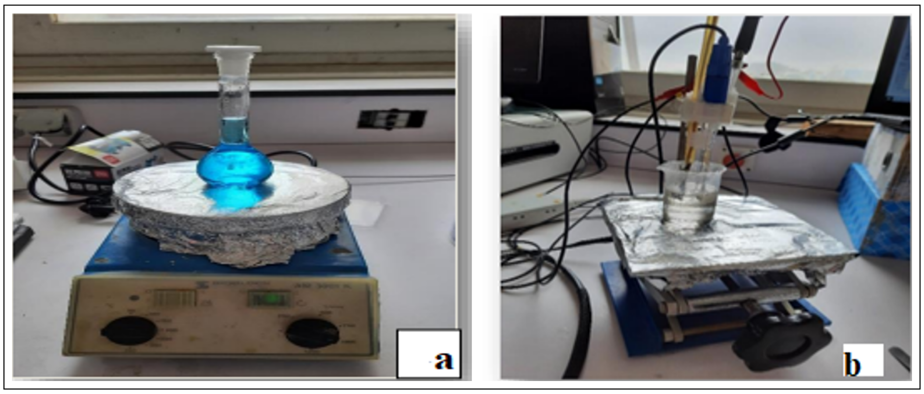

Figure 2.4: Steps for the preparation of copper(I) oxide (Cu_2O) coating: (a) preparation of $CuSO_4$ solution, (b) electrochemical deposition of Cu_2O onto the substrate.

2.1.3.2 Chemical route

2.1.3.2.1 Polyaniline synthesis

Two solutions were made by adding 1.82 ml of aniline monomer and 5.71 g of ammonium peroxodisulfate in two 100 ml solutions containing 1 M methanol and 0.4 M acetic acid, respectively. Then the aniline solution and the oxidizer solution were placed in an ice bath at 0 °C to cool for 30 min. Then these two solutions were mixed and stirred rapidly for 30 s, left for 16 h at 0 °C. The final product was dried at 70 °C for 12 h after being filtered and washed with deionized water. Finally, the powder was ground to obtain dark green polyaniline nanotubes [64, 65].

2.1.3.2.2 Chemicals used

Four chemical reagents were employed for the preparation of the composite films illustrated in table 2.1

Materials	**Purity %**	**Company**
Aniline, $C_6H_5NH_2$	99.5	Sigma-Aldrich
Ammonium peroxodisulfate, $H_8N_2O_8S_2$	98	Aldrich Chemical
Methanol, CH_4O	99.5	Fisher
Acetic acid, $C_2H_4O_2$	100	Fisher

Table 2.1: Chemicals and reagents used

2.1.3.2.3 Electrode preparation

2.1.3.2.3.1 Preparation of the base C/PANI-based paste

To prepare the composite slurry, 2.5 mL of N-methyl-2-pyrrolidone (NMP) was added to a vial containing 30 mg of polyvinylidene fluoride (PVDF). The mixture was heated to 70 °C with constant stirring until the PVDF binder was completely dissolved. Separately, 15 mg of carbon black and 270 mg of dried PANI powder were mixed and ground using a mortar and pestle until a homogeneous blend was obtained. This powder mixture was then introduced into the PVDF/NMP solution and stirred at room temperature for 24 hours. The resulting slurry was then subjected to a thermal treatment at 60 °C for 3 hours, followed by another 3 hours at 80 °C. This produced a low-viscosity mixture. An additional thermal step of 6 hours at the same temperatures was applied to further increase the viscosity, optimizing the rheological properties for film deposition. The full process is illustrated in Figure 2.5.

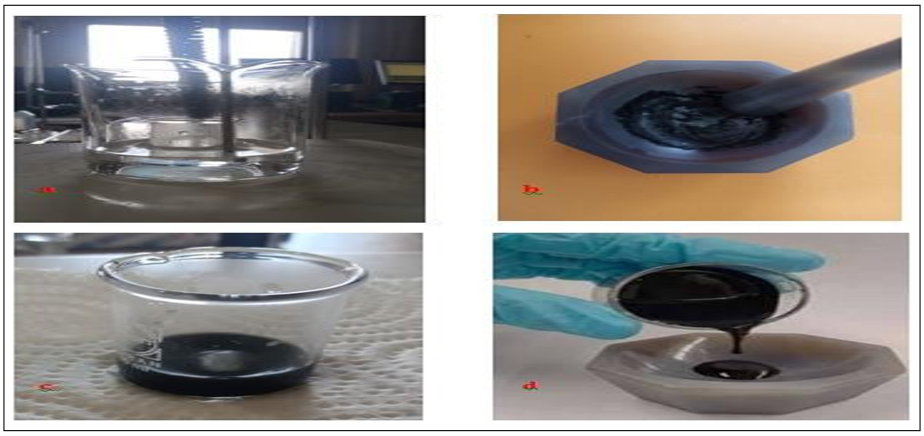

Figure 2.5: Stages of C/PANI paste preparation: (a) PVDF/NMP solution, (b) C/PANI composite powder, (c) paste during homogenization (d) final viscous paste.

2.1.3.2.3.2 Paste coating procedure on graphite

The working electrodes used for electrochemical characterization were prepared via this route by manually coating the graphite substrates with the C/PANI paste using a fine brush. The coated electrodes were then dried in an oven for 48 hours. This fabrication step is shown in Figure 2.6.

Figure 2.6: Manual spreading of the C/PANI paste on the graphite electrode

2.1.3.2.4 Synthesis of Zn-Doped Polyaniline (Zn/PANI)

To explore the effect of Zn^{2+} incorporation on the physicochemical and electrocatalytic properties of polyaniline, Zn-doped PANI (Zn/PANI) was synthesized via a controlled in situ chemical oxidative polymerization in acidic medium.

2.1.3.2.4.1 Reagents and materials

- Aniline monomer ($C_6H_5NH_2$)
- Hydrochloric acid (HCl, 1 M) – for protonation of aniline
- Ammonium persulfate (APS, $(NH_4)_2S_2O_8$) – oxidizing agent
- Zinc nitrate hexahydrate ($Zn(NO_3)_2 \cdot 6H_2O$) – Zn^{2+} source
- Distilled water
- Ethanol – washing solvent
- Magnetic stirrer
- Ice bath

2.1.3.2.4.2 Synthesis protocol

Step 1 – Preparation of the Acidic Aniline Medium
1 mL of aniline was introduced into 100 mL of 1 M HCl under continuous magnetic stirring. The solution was immediately cooled to 0–5 °C in an ice bath to suppress spontaneous polymerization and maintain kinetic control over chain growth.

Step 2 – Preparation of the Oxidant/Zn Precursor Solution
In parallel, 2.5 g of APS and 0.5 g of $Zn(NO_3)_2 \cdot 6H_2O$ were completely dissolved in 50 mL of distilled water. This solution was also cooled to 0–5 °C to ensure consistent thermal conditions across both reactive media.

Step 3 – In Situ Oxidative Polymerization and Zn Doping
The cold APS/Zn^{2+} solution was added dropwise to the aniline-HCl solution over time under vigorous magnetic stirring, while maintaining the reaction temperature strictly between 0 and 5 °C. The polymerization process was allowed to proceed for 4 to 6 hours. A progressive color change to dark green was observed, indicating the formation of the Zn-doped polyaniline in its emeraldine salt form.

Step 4 – Isolation, Purification, and Drying
The resulting precipitate was collected by vacuum filtration, washed thoroughly with distilled water to remove residual oxidant and ions, followed by multiple rinses with ethanol to facilitate dehydration and remove organic by-products. The final product was dried under vacuum at 60 °C for 12–24 hours to ensure complete removal of solvents and obtain the Zn/PANI powder in its dry state.

2.1.3.2.5 Synthesis of Zn-doped PANI nanocomposites

In order to investigate the effect of Zn incorporation on the physicochemical and photoelectrocatalytic properties of polyaniline, two Zn-doped PANI nanocomposites were prepared with Zn loadings of 20 wt% and 30 wt%, respectively, relative to the total composite mass.

The preparation route was based on the same procedure described for the undoped PANI paste formulation, with the modification consisting of the introduction of metallic Zn powder into the dry composite matrix prior to dispersion. The detailed preparation steps are as follows:

- **Weighing and dry mixing:** The required quantities of chemically synthesized PANI, Zn powder (purity ≥99.9%, particle size <75 µm), activated carbon (AC), and PVDF were calculated according to the targeted mass ratios:

  *For **30%** Zn–PANI composite:*

  - PANI: 55 wt%
  - Zn: 30 wt%
  - AC: 5 wt%
  - PVDF: 10 wt%

  *For **20%** Zn–PANI composite:*

  - PANI: 60 wt%
  - Zn: 20 wt%
  - AC: 5 wt%
  - PVDF: 10 wt%

  The dry powders were initially homogenized using an agate mortar and pestle to ensure intimate mixing and uniform dispersion of Zn particles within the PANI matrix.

- **Dispersion in solvent:** The powder mixture was gradually introduced into an appropriate volume of N-methyl-2-pyrrolidone (NMP) under vigorous magnetic stirring to ensure uniform dispersion. Stirring was maintained at room temperature for approximately 4 hours until a viscous, homogeneous slurry was obtained.

- **Optimization of viscosity and paste homogenization:** The final rheology of the suspension was adjusted by incrementally adding small amounts of NMP until optimal viscosity was achieved for electrode casting. The mixture was then subjected to mild thermal treatment at 60 °C for 30 minutes to eliminate potential agglomerates and improve the wetting of polymer chains.

- **Application onto graphite substrates:** The resulting Zn–PANI paste was applied onto pre-cleaned cylindrical graphite substrates (Cgr) using a drop-casting method. The electrodes were subsequently dried at 60 °C under vacuum for 2 hours to ensure solvent removal and good film adhesion.

2.1.4 Photoelectrochemical reduction of CO_2 gas

In this part of our work, we focused on evaluating the photoelectrochemical performance of the pre-developed structures, aiming to use them as photocatalysts. The different prepared samples were tested as photoelectrodes for the reduction of protons into di-hydrogen by the photoelectrocatalytic water splitting [66, 67, 68].

2.1.4.1 Experimental setup for CO_2 reduction

To perform CO_2 reduction through photoelectrocatalysis, a dedicated experimental system was necessary to facilitate both water splitting and CO_2 photoreduction. The setup includes:

1) a photoelectrochemical (PEC) cell or reactor equipped with a sampling port;
2) a CO_2 gas supply system;
3) an AUTOLAB PGSTAT302N potentiostat/galvanostat interfaced with NOVA 2.1 software for data acquisition.

CO_2-saturated aqueous solutions of sodium bicarbonate ($NaHCO_3$) or potassium bicarbonate ($KHCO_3$) are commonly used as electrolytes in PEC CO_2 reduction studies. Excessively high bicarbonate concentrations can screen the electric field and promote the hydrogen evolution reaction (HER) over CO_2 conversion. Hence, bicarbonate solutions in the range of $0.1 - 0.5$ M are generally preferred. In this setup, CO_2 was introduced into our cell via tubing connected to a CO_2 gas cylinder, in a configuration following a conventional three-electrode arrangement, as illustrated in Figure 2.7.

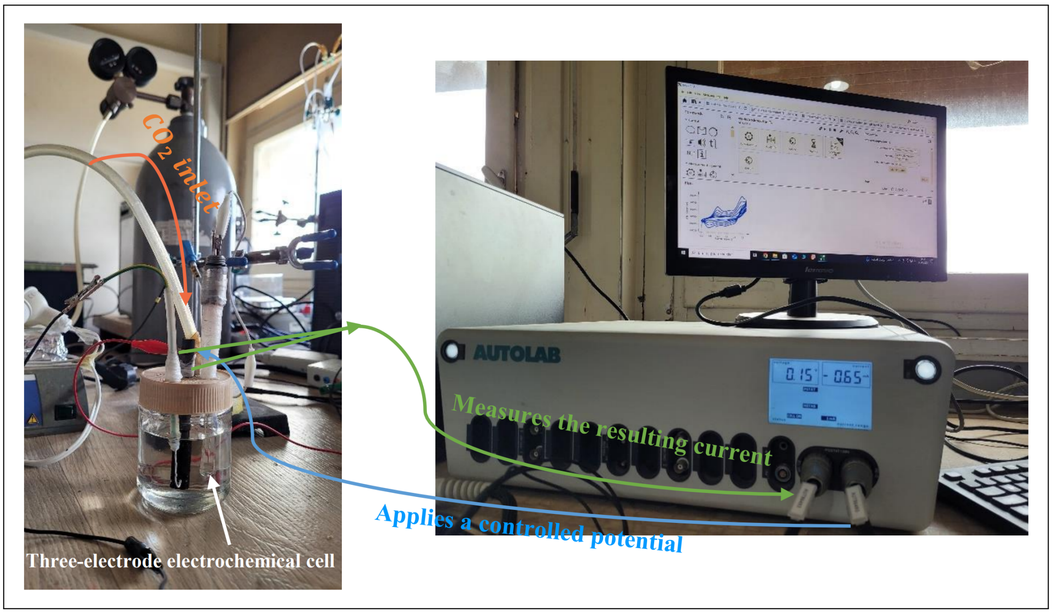

Figure 2.7: Schematic of the conventional electrochemical setup for CO_2 reduction

2.1.4.2 Photoelectrochemical cell

The PEC cell was made of Pyrex glass with a 150 mL capacity, sufficient to maintain stable concentrations of electroactive species throughout the experiment. The cell was equipped with a lid allowing the insertion of three electrodes and a gas inlet tube. For photocatalytic activation, the cell was irradiated with natural sunlight (daylight). The three-electrode configuration included:

- **Reference electrode:** Ag/AgCl electrode, immersed in a capillary filled with supporting electrolyte, used for measuring electrode potentials.
- **Counter electrode:** A platinum wire positioned parallel to the working electrode to ensure uniform current distribution.
- **Working electrode:** The photoelectrodes, fabricated as thin films of PANI-based catalytic materials.

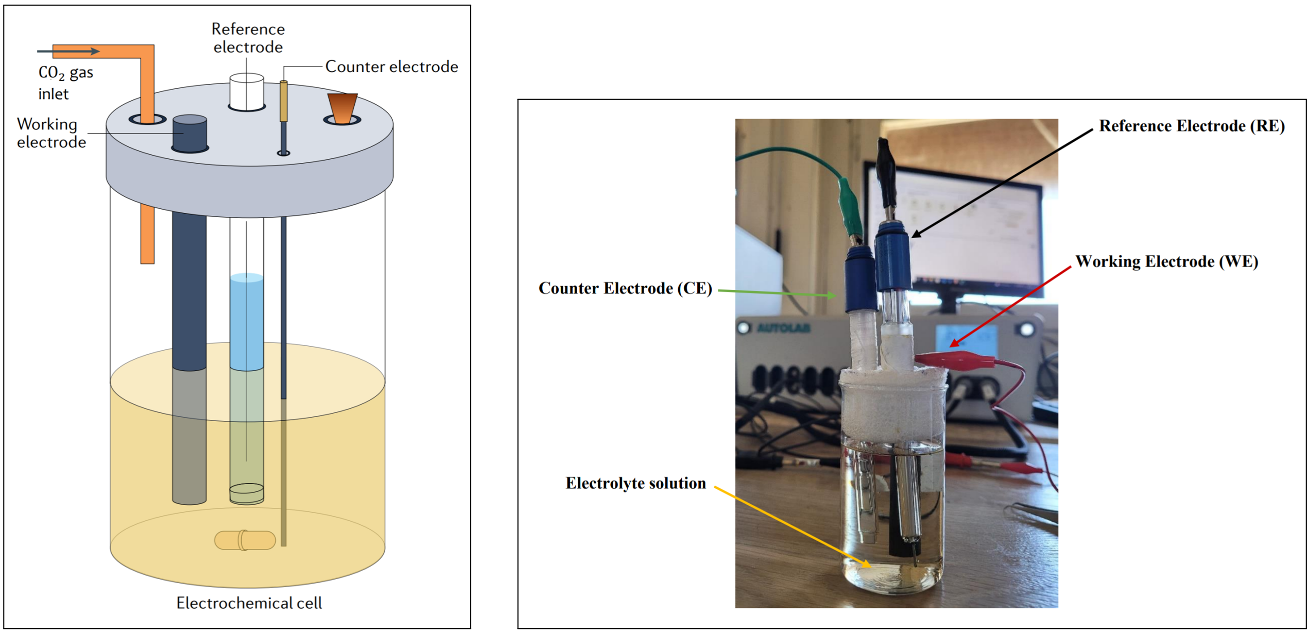

(a) Schematic representation of the cell [69].

(b) Experimental photo of the cell

Figure 2.8: Schematic and visual representation of the three-electrode electrochemical cell

2.1.4.3 Electrolyte solution

The **electrolyte** used for the PEC study was a 0.5 M aqueous potassium carbonate (K_2CO_3) solution (prepared by dissolving 27.6 g of K_2CO_3 in 400 mL of deionized water). The pH of the resulting solution was measured to be approximately 10. Prior to electrolysis, the electrolyte was saturated with CO_2 gas for 30 minutes. After gas bubbling, the CO_2 inlet tube was removed and the cell was sealed immediately to minimize gas loss. All PEC measurements were carried out under ambient laboratory conditions, with an applied potential ranging from -1.5 V to +0.5 V and a scan rate of 10 mV/s. The liquid-phase products were analyzed using gas chromatography (GC) equipped with a thermal conductivity detector (TCD).

2.2 Characterization techniques

Multiple analytical techniques were employed to characterize the structural, morphological, optical, and chemical properties of the synthesized materials. Below is a brief description of each method used, including its working principle and purpose in this study.

2.2.1 Scanning Electron Microscopy

SEM is a powerful technique for analyzing the surface morphology and chemical composition of most solid materials (particularly when equipped with a microprobe). It is primarily based on the detection of secondary electrons emitted from the sample surface when irradiated by a focused beam of primary electrons. These electron–matter interactions generate high-resolution images of the surface topography.
To investigate the surface morphology of the synthesized samples, we used a field-emission SEM

(FE-SEM) model JEOL JSM 7610FPlus, at CRTSE. This instrument offers a lateral resolution below 5 nm and a large depth of field [70]. An SEM is composed of an electron gun and a column that focuses the electron beam, a sample stage for multi-axis positioning, and detectors that collect and analyze the emitted radiation. The entire system operates under vacuum conditions. Note that for quantitative vertical dimensional analysis, cross-sectional imaging is necessary [71].

Figure 2.9: Scanning Electron Microscope JEOL JSM 7610FPlus (CRTSE)

2.2.2 Fourier-Transform Infrared Spectroscopy

FTIR spectroscopy is a non-destructive analytical technique used to identify the functional groups and chemical bonds present in a material. It provides direct insight into the molecular structure of chemical compounds in solid, liquid, or gaseous phases [72, 73].
FTIR measurements were performed using a Thermo Nicolet Nexus spectrometer (Figure 2.10) within the spectral range of 400–4000 cm^{-1} at a resolution of 4 cm^{-1} [62, 74]. Samples were placed at the Brewster angle to minimize reflection losses at surfaces and interfaces. Data acquisition and processing were carried out using OMNIC software.

Figure 2.10: Thermo Nicolet FTIR Spectrometer (CRTSE)

2.2.3 UV-Visible-NIR Absorption Spectroscopy

UV–vis–NIR absorption spectroscopy is a fundamental technique for investigating the optical properties of thin films. It provides information about light absorption and transmission, band gap energy (E_g), and, in some cases, film thickness. The principle of the method relies on the interaction of light with the sample, where absorption in the UV-Vis-NIR range induces transitions in the electronic structure of atoms, ions, or molecules.
Furthermore, UV–Vis spectroscopy reveals characteristic absorption bands for each form. For example:

- **Leucoemeraldine:** $\sim 320\ nm$ (π–π^* transitions)
- **Emeraldine base:** $\sim 600\ nm$ (benzenoid to quinoid transition).
- **Emeraldine salt:** $\sim 420\ nm$ and a polaron band at $\sim 800\ nm$.

Reflectance spectra were recorded using a CARY 5000 UV-Vis-NIR spectrophotometer (VARIAN) at CRTSE (Figure 2.11). The setup includes a light source, monochromator, and detector. Deuterium and tungsten lamps are used for UV and visible regions, respectively. Spectral analysis is performed by dispersing polychromatic radiation according to wavelength [75].

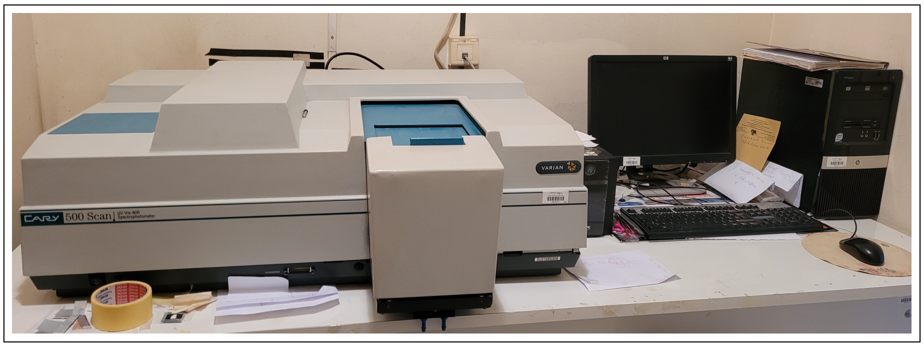

Figure 2.11: CARY 5000 UV-Vis-NIR Spectrophotometer (VARIAN), CRTSE

2.2.4 X-Ray Diffraction

XRD is a widely used technique to analyze the crystalline structure of materials. It is based on the elastic scattering of monochromatic X-rays by a crystalline sample. When X-rays interact with the periodic atomic planes, they are diffracted in specific directions, producing a diffraction pattern characteristic of the crystal structure.
The fundamental relationship governing the angular positions of X-ray diffraction peaks is described by **Bragg's Law**, which relates the incident wavelength to the crystal lattice spacing:

$$n\lambda = 2d\sin\theta \tag{2.1}$$

This equation captures the condition for constructive interference of X-rays scattered by periodic atomic planes within a crystalline material. When the path difference between rays reflected from successive planes equals an integer multiple of the wavelength, a diffraction peak is observed [76, 77].

Where:

- n is a positive integer representing the diffraction order.
- λ is the wavelength of the incident X-ray beam.
- d is the interplanar spacing between adjacent atomic layers.
- θ is the Bragg angle, defined as the angle between the incident ray and the crystallographic plane.

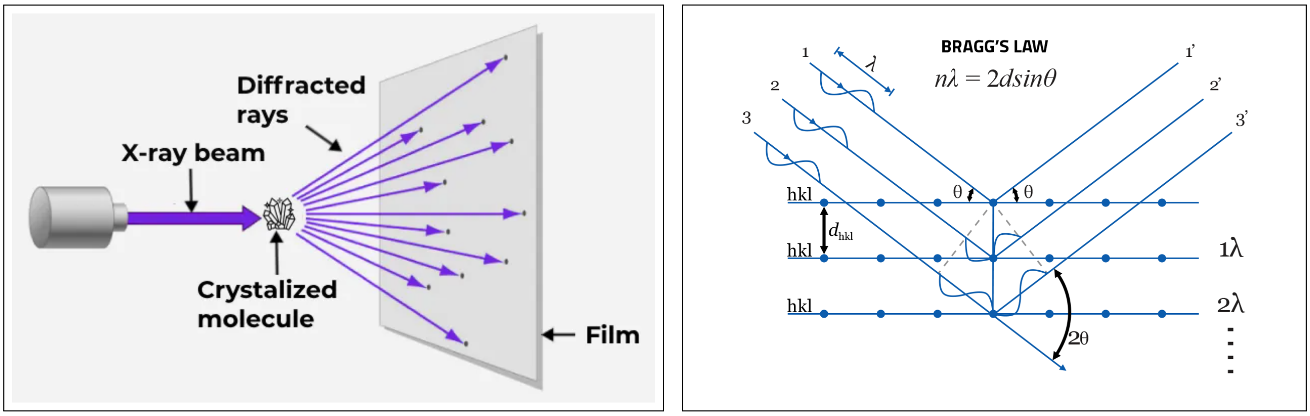

(a) Principle of XRD analysis [76].

(b) Diffraction from a family of crystallographic planes (hkl) [77].

Figure 2.12: Illustration of the XRD analysis principle and diffraction from crystallographic planes

XRD is extensively used in materials science, solid-state physics, and structural biology [78]. Phase identification is carried out by comparing the sample's diffraction pattern with standard reference data. The analysis typically focuses on the first 20 to 30 most intense diffraction peaks, listed by decreasing interplanar spacing (d) and relative intensity (I) [79, 80, 51].

2.2.5 X-Ray Photoelectron Spectroscopy

XPS is based on the photoemission effect. Upon irradiation with X-ray photons, atoms in a solid emit photoelectrons due to the photoelectric effect. The kinetic energy (E_k) of these emitted electrons is analyzed to determine the elemental composition, chemical state, and electronic structure of the surface.
XPS is both qualitative and quantitative, capable of identifying elements and estimating their concentrations at the material's surface.

2.2.6 Wavelength Dispersive X-Ray Fluorescence

WD-XRF Spectroscopy is a non-destructive, multi-elemental analytical technique that enables the accurate identification and quantification of the overall chemical composition of a sample. Its analytical range spans from boron (Z = 5) to uranium (Z = 92), with detection limits ranging from a few parts per million (ppm) up to 100%. This method offers significant advantages, including minimal sample preparation, rapid analysis, and above all high reproducibility. The measurements in this study were carried out at the CRNA, ensuring standardized and traceable analytical conditions.
The technique operates by bombarding the sample with primary X-rays, which eject inner-shell electrons, ionizing the atom. A higher-energy electron then fills the vacancy, emitting secondary (characteristic) X-rays in the process. The emitted radiation is analyzed to determine the qualitative and quantitative elemental composition.
The technique is based on the following principle: the sample is irradiated with a beam of primary X-rays, which excites the atoms of the constituent elements, resulting in the ejection of inner-shell electrons (close to the nucleus). The atom becomes ionized, and an electron from a higher-energy shell subsequently fills the vacancy. In doing so, it loses energy by emitting a photon in the X-ray region, an event known as X-ray fluorescence. The energy of the emitted secondary X-ray is element-specific and thus characteristic of the emitting atom. By analyzing this secondary X-ray radiation, it is possible to determine both the elemental composition and the corresponding mass concentrations of the elements present in the sample.

2.2.7 Photoelectrochemical characterization

Photoelectrochemical characterization is based on the measurement and analysis of the photocurrent. The principle involves irradiating the active layer with monochromatic light and extracting the resulting photocurrent using a phase-sensitive detection technique. The photocurrent is defined as the difference between the current measured under illumination and the current measured in the dark.

2.2.7.1 Linear and Cyclic Voltammetry (LSV and CV)

Voltammetry is an electroanalytical technique that measures the electron flux resulting from the oxidation or reduction of analytes in solution, as induced by a controlled variation of the potential difference between two specific electrodes. Cyclic voltammetry involves the repeated application of a linearly time-varying potential (E) to the working electrode, scanning between two predefined potential limits. The resulting current–potential curves, known as voltammograms, provide detailed information about the electrochemical behavior of the system—such as the real surface area of the electrode, the kinetics and mechanisms of interfacial electrochemical reactions (particularly at the electrocatalyst/electrolyte interface), and electrode stability over multiple potential cycles.

In this work, cyclic voltammograms were recorded at a scan rate of 10 $mV \cdot s^{-1}$ over a potential window ranging from $+0.5\ V$ to $-1.5\ V$ vs Ag/AgCl. Measurements were carried out under dark, UV, and visible light conditions. In parallel, linear sweep voltammetry was employed to estimate the onset potential for the electrochemical reactions. This technique is broadly applicable across various electrode materials and electrolyte systems [81].

As mentioned previously, all photoelectrochemical experiments were conducted using an AUTOLAB PGSTAT302N Potentiostat/Galvanostat system, controlled via NOVA 2.1 software, which facilitates full data acquisition and experimental control. A visible-light lamps were employed to perform illumination-based electrochemical measurements.

2.2.7.2 Chronoamperometry (Potentiostatic Mode)

Chronoamperometric studies, conducted under an applied constant potential, are primarily used to evaluate electrocatalytic activity, monitor the evolution of the electrode surface, and assess the long-term stability of molecular or composite catalysts. In this method, a fixed potential is applied to the working electrode relative to a reference electrode, and the resulting current is recorded as a function of time. The technique is straightforward to implement using a laboratory Potentiostat.

2.2.7.3 Gas chromatography analysis

The identification and quantification of both reaction products and residual reactants were performed using gas chromatography (GC). A Flame Ionization Detector (FID) was employed to detect organic compounds such as methanol and methane [75, 82]. The gas chromatograph system consists of:

- A SHIMADZU GC-2014 chromatograph, operated via a microcomputer interface;
- An analytical column packed with DEGS (diethylene glycol succinate);
- Detector temperature: 160 °C;
- Column temperature: 100 °C;
- Carrier gas: Argon, at a flow rate of 0.9 L/min.

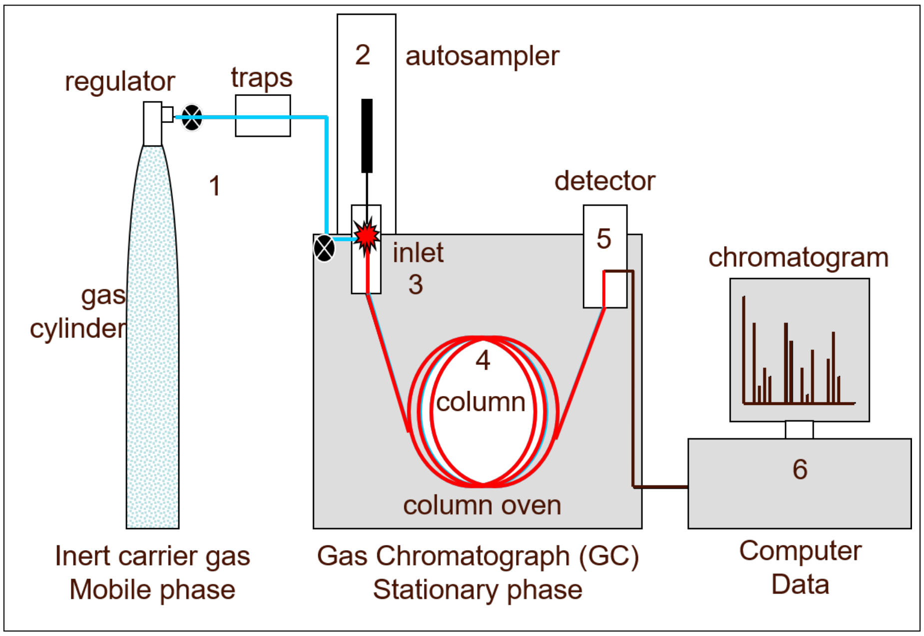

Figure 2.13: Schematic of the gas chromatographic system setup [15].

2.2.7.4 Electrochemical Impedance Spectroscopy

EIS is a powerful frequency-domain technique employed to investigate the interfacial charge transfer processes, capacitive behavior, and ionic diffusion mechanisms within the photoelectrochemical system. The impedance response is measured by applying a small amplitude sinusoidal voltage perturbation (typically 5–10 mV) over a broad frequency range, here from 100 kHz to 1 mHz, at the open-circuit potential under both dark and illuminated conditions.

The obtained data are represented in the form of Nyquist and Bode plots.

2.2.7.5 Tafel polarization analysis

Tafel analysis is a steady-state electrochemical technique that enables the extraction of key kinetic parameters related to the cathodic (reductive) reaction, especially useful in assessing electrocatalytic activity toward CO_2 reduction. It involves recording the polarization curve (plotting the logarithm of the current density (log |I|) versus the applied potential (E)) in the region where the system deviates from equilibrium.

The Tafel plot allows the determination of:

- Corrosion potential ($\mathrm{E_{corr}}$) and corrosion current density ($\mathrm{i_{corr}}$) — derived from the intersection of anodic and cathodic branches, particularly relevant when assessing the material's stability under operating conditions,
- Polarization resistance ($\mathrm{R_p}$) — extracted from the slope around $\mathrm{E_{corr}}$, inversely related to reaction kinetics.

These parameters were deduced by applying tangent fits to the linear portions of the anodic and cathodic branches of the Tafel curve.

Chapter 3

Results and Discussions

Part A: Characterization of the catalyst and electrodes

In this initial section of the chapter, we present the various characterization techniques employed to identify the synthesized electrocatalyst—-namely, polyaniline (PANI)—-and to confirm the successful formation of the desired material prior to its integration into electrode fabrication. As outlined in the previous chapter, two types of electrodes were developed: the first involved electrochemically synthesized HCl-doped PANI thin films; the second consisted of a slurry-cast formulation composed of chemically synthesized PANI powder blended with carbon black and polyvinylidene fluoride (PVDF), subsequently deposited onto cylindrical graphite rods.

3.1 Chemical composition of the substrate

The selection of a material is based particularly on its corrosion resistance, as it is essential that it retains its electrochemical properties during its use. This also implies special attention to the substrate on which the material is deposited. With this in mind, our choice was graphite due to its good electrical conductivity and excellent lubricating properties. The graphite used is in a cylindrical form and in a state of high purity, as confirmed by EDXRF analysis (Figure 3.1). This analysis reveals a composition dominated by carbon, along with traces of calcium, manganese, iron, nickel, strontium, and zirconium. table 3.1 gives the proportions of these elements.

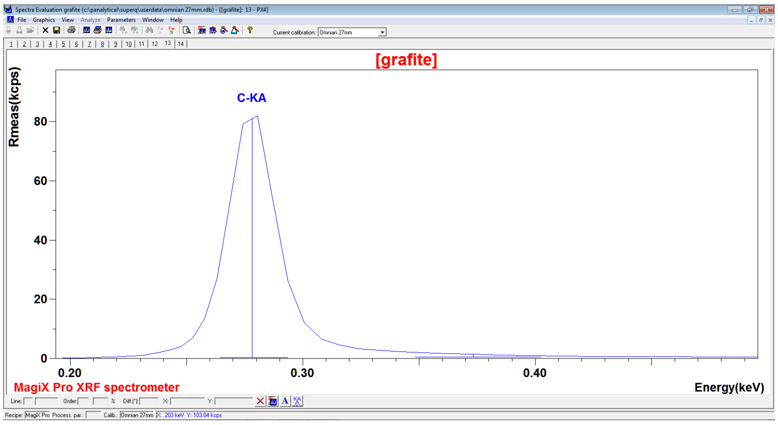
Spectra Evaluation grafite (c:\panalytical\superq\userdata\omnian 27mm.rdb) - [[grafite]: 13 - PX4]

Current calibration: Omnian 27mm

Recipe: MagiX Pro Process. par.: Calib.: Omnian 27mm X: .203 keV Y: 103.04 kcps

Figure 3.1: EDXRF peak of Carbon

Element	C	O	F	Na	Mg
Percentage	76.956%	17.321%	1.295%	1.238%	0.144%
Element	Al	Si	P	S	Cl
Percentage	0.177%	0.462%	0.037%	0.315%	1.403%
Element	K	Ca	Fe	Ni	Cu
Percentage	0.103%	0.117%	0.105%	0.042%	0.139%
Element	Zn	Pb			
Percentage	0.111%	0.035%			

Table 3.1: proportion of elements in grpahite substrate .

3.2 Electropolymerization

Electropolymerization is an efficient and straightforward treatment method, particularly well-suited for the development of polymeric films such as polyaniline (PANI). Electrochemistry thus proves to be an ideal approach for material functionalization. PANI can be synthesized through two processes: one chemical and the other electrochemical, both based on the oxidation of aniline in an acidic medium. In the context of our work, the electrochemical route was adopted. For this purpose, cyclic voltammograms were recorded using an Autolab NOVA 2.1 potentiostat/galvanostat, serving as a current or voltage source. The measurements were carried out in an electrochemical cell consisting of a working electrode, a counter electrode, and a reference electrode.

The electro-polymerization of PANI on graphite and platinum surfaces was carried out by cyclic voltammetry using a solution containing the aniline monomer (0.2M), hydrochloric acid (0.5M), and a solvent. The system's response was recorded in the form of a voltammogram, within a potential range of -0.2 to 0.9 V (Ag/AgCl), at a scan rate of 20 mV/s. On all voltammograms.

3.2.1 Electrodeposition of polyaniline (PANI) on platinum

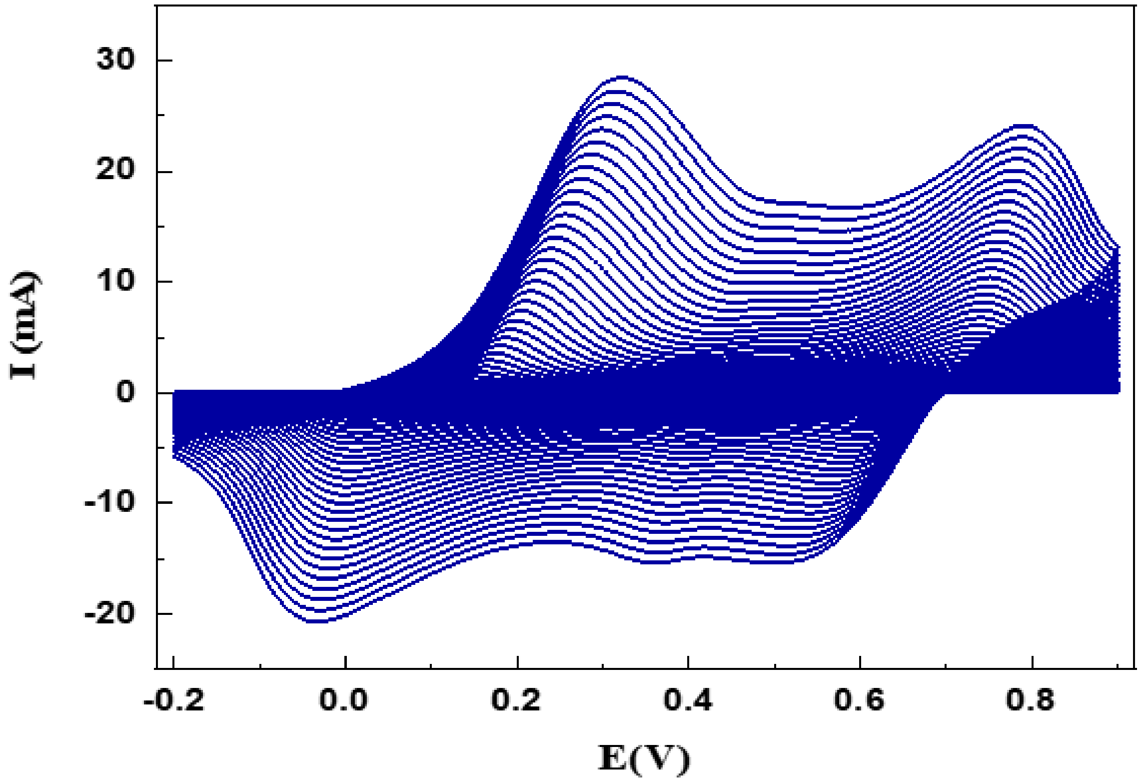

Figure 3.2: Voltammogram of HCl-PANI electropolymerization on Platinum in a solution of 0.2 M aniline, 0.5 M HCl, at a scan rate of 20 mV/s

It is well known that the cyclic voltammograms of PANI recorded in an acidic medium usually show redox peaks corresponding to a series of redox transitions. PANI mainly has three distinguishable oxidation states, namely, the fully reduced (leucoemeraldine), the half-oxidized (emeraldine) and the fully oxidized (pernigraniline) state, with virtually an infinite number of possible oxidation states existing in between. Therefore, in principle, PANI can exist in a continuum of oxidation states ranging from a completely reduced to a completely oxidized form.

Analysis of the voltammogram shown in figure 3.2 reveals three redox peak pairs, centered around 0.2 V, 0.5 V, and 0.75 V respectively, whose intensity increases with the number of cycles. This behavior is consistent with data reported in the literature.[61, 83]

- The oxidation peak at 0.2 V corresponds to the transition of PANI in a leucoemeraldine state to an intermediate oxidation state (leucoemeraldine radical cation), resulting from electron loss.
- The peak at 0.5 V is attributed to the conversion of PANI in the form of emeraldine radical cation into emeraldine, with a benzoquinone-like structure
- The peak at 0.75 V reflects the complete transition from the intermediate state to a fully oxidized state of PANI, characterized by enhanced electron loss. (the transformation of the cation of the pernigraniline radical to pernigraniline)

From the first cycle onward, a visible color change of the electrode is observed, indicating the progressive deposition of a polymer film on its surface.

3.2.2 Electrodeposition of polyaniline (PANI) on graphite

During the positive potential sweep, an increase in current is observed, corresponding to the oxidation of aniline to a radical cation, followed by a reduction of the formed polymer around 0.4V (vs. Ag/AgCl).

Notably, as the number of cycles increases, which indicates the growth of the PANI layer, the current associated with the oxidation and reduction peaks also increases, causing a small shift of the oxidation peak toward higher anodic potentials, and the reduction peak toward lower potentials. This is due to the electroactivity of polyaniline in this solution, confirming the deposition of the polymer on the electrode. This deposition is visually evidenced by the formation of a dark green layer, characteristic of polyaniline in its conductive emeraldine salt form.These observations are in agreement with the data from the literature, particularly those reported by SNAUWAERT et al[84],Regarding the oxidation transitions of PANI. In general, polyaniline chains are composed of structural units of the quinoid and benzenoid types, which can transform into each other through redox reactions.

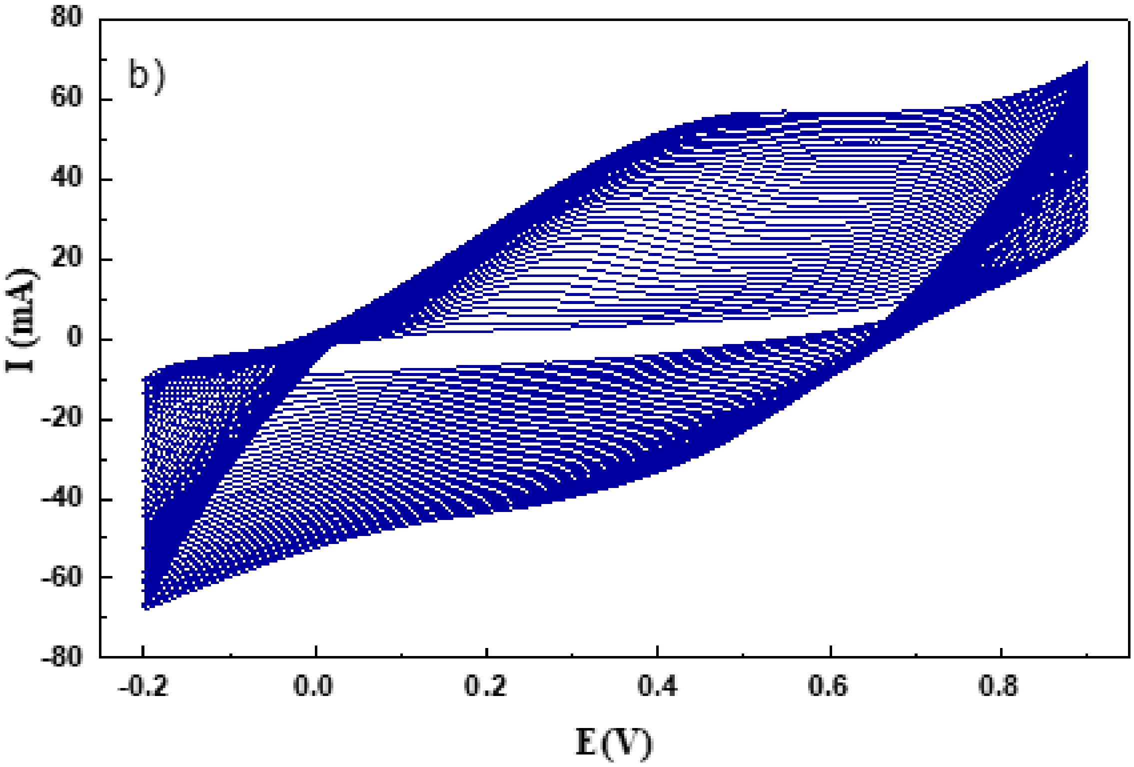

Figure 3.3: Voltammogram of HCl-PANI electropolymerization on graphite in a solution of 0.2 M aniline, 0.5 M HCl, at a scan rate of 20 mV/s

3.2.3 Mechanism of PANI polymerization

The mechanism of electrochemical polymerization of polyaniline (PANI) is based on a polycondensation reaction involving several successive steps. The first step consists of the electrochemical oxidation of the aniline monomer at the working electrode surface, leading to the formation of cationic radicals via a shift in the nitrogen electron level. These reactive species adsorb onto the electrode surface and initiate the growth process.

In the next step, these radical cations react with the most reactive resonance forms of aniline, giving rise to dimers. These dimers are then electrochemically re-oxidized to produce new cationic radicals, which can couple with other activated monomers or oligomers, thus progressively forming trimers, tetramers, and increasingly longer chains (see Figure 3.4).

When the oligomers reach a certain critical size and become insoluble in the reaction medium, they precipitate onto the electrode, forming an adherent polymer film. This deposition continues as long as the applied potential remains above the polymerization threshold. However, the increasing thickness of the film induces a growing ohmic drop between the imposed potential and the actual potential at the electrode/solution interface. When this drop becomes sufficient to lower the effective potential below that required for the oxidation of aniline, polymerization naturally stops.

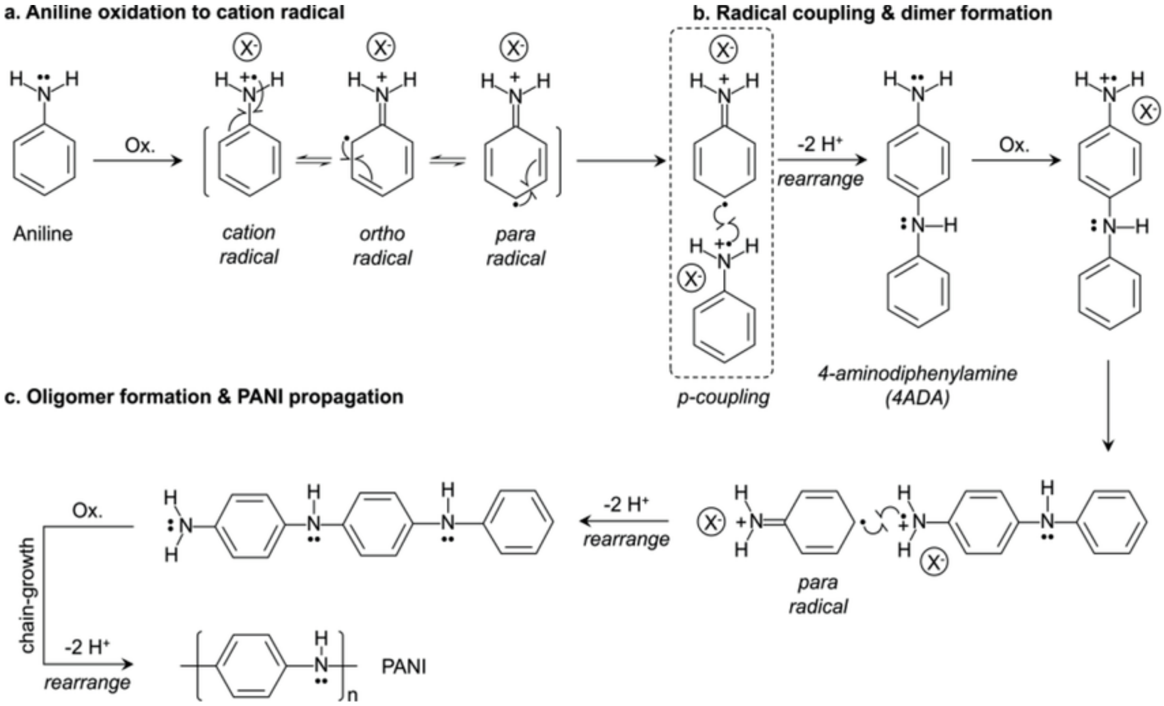

Figure 3.4: Mechanism of electropolymerization of polyaniline.

3.3 Fourier Transform Infrared Spectroscopy(FT-IR)

The synthesized polyaniline was characterized by Fourier Transform Infrared Spectroscopy (FTIR), as illustrated in Figure 3.5. The analyses were carried out on a pellet obtained by vacuum compression of a homogeneous mixture of finely ground PANI and potassium bromide (KBr). This mixture was pressed to form a pellet with a diameter of 13mm and a thickness of approximately 1mm, suitable for FTIR analysis.

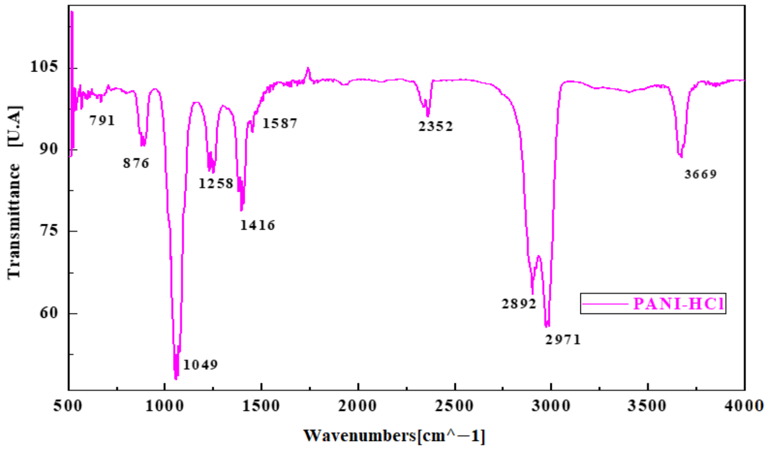

Figure 3.5: FTIR spectrum of HCl-Doped PANI.

The analysis of the FTIR spectrum reveals the main absorption bands characteristic of the vibrations of functional groups in polyaniline in its emeraldine base form. These bands confirm the structure of the synthesized polymer:

- The bands located at 1495 $cm{-}1$ and 1587 $cm{-}1$ are associated with the vibrations of the benzenoid diamine units (N–B–N) and the quinoid diamine units (N=Q=N), respectively [85], indicating that the PANI is partially doped [59].
- The bands around 1239 $cm{-}1$ and 1302 $cm{-}1$ correspond to deformation vibrations of C–N and C–H bonds, characteristic of secondary aromatic amines [86, 87].
- The band at 1126 $cm{-}1$ is attributed to deformation vibrations of the benzenoid or quinoid ring bearing a C–H bond [59, 88].
- The band observed at 3447 $cm{-}1$ corresponds to the stretching vibrations of the N–H bond.
- Finally, the bands in the region 812–876 $cm{-}1$ are related to out-of-plane deformation vibrations of C–H bonds, characteristic of para-disubstitution on aromatic rings.

All of these bands confirm the successful synthesis of polyaniline, consistent with its expected structure and the literature data.

3.4 Scanning Electron Microscopy (SEM)

Figures below show the SEM images at different magnifications of PANI and HCl-doped PANI powders prepared both chemically and electrochemically, as well as HCl-doped PANI and PANI/CU_2O both deposited on graphite substrates.

Figure 3.6.a and 3.6.b presents SEM images of HCl-doped polyaniline (PANI) powder obtained synthesised electrochemically. From Figure 3.6.a, a homogeneous distribution of particles on the substrate surface is observed At 1000x magnification. These particles exhibit a rough granular texture with moderate agglomeration, forming a compact and porous layer. This uniform distribution indicates controlled growth of PANI during electropolymerization.

When zooming in at 10000x magnification, The structure becomes more distinct, revealing short tubular or fibrillary nano-aggregates characteristic of a high specific surface area (Figure 3.6.b). The irregular and porous surface ensures optimal accessibility to active sites. The dense agglomeration of grains promotes good connectivity between particles, thereby facilitating charge transfer and enhancing electronic conductivity within the electrode. This interconnected nanogranular morphology is well-suited for electrocatalytic applications

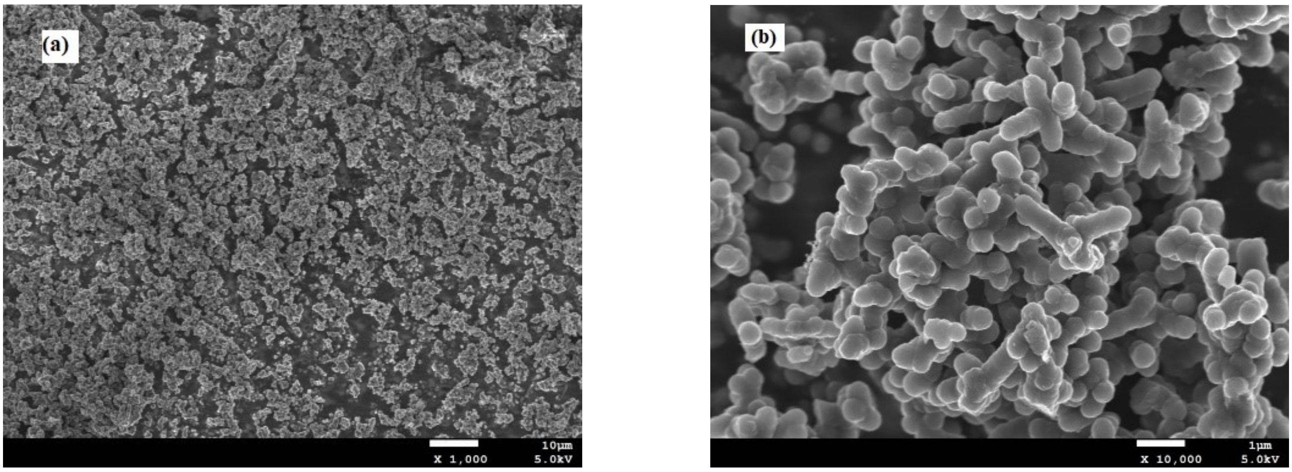

Figure 3.6: SEM images of Hcl-Doped PANI powder.

Regarding the PANI powder synthesized via the chemical route, shown in Figures 3.7.a and 3.7.b, it exhibits a dense nanogranular morphology characteristic of PANI. The surface consists of tightly packed submicron sized particles, predominantly spheroidal to irregular in shape. Their compact arrangement and low porosity give the material a rough texture.

This structural organization suggests rapid growth or intense nucleation. Despite relatively uniform grain size, the significant agglomeration observed could reduce accessible porosity while enhancing electronic conductivity through multiple interparticle contact points.

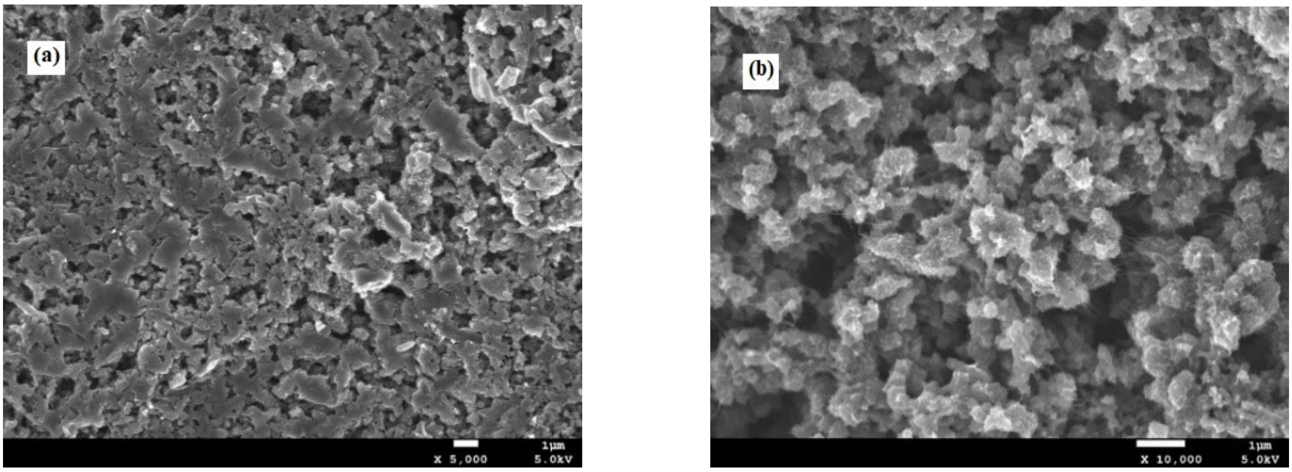

Figure 3.7: SEM images of pure PANI powder.

Figures 3.8.a and 3.8.b demonstrate HCl-doped polyaniline thin films deposited on graphite, showing globally homogeneous surfaces composed of dense, porous networks. The continuous films consist of well distributed agglomerated particles, indicating homogeneous polymerization. Figure 3.8.b clearly displays HCl-PANI forming porous nanofibrous/nanowire structures that create 3D interconnected networks, a hallmark of well structured conductive nanomaterials that enhance both conductivity and active surface area. This morphology proves particularly advantageous for electrochemical applications like photocatalysis.

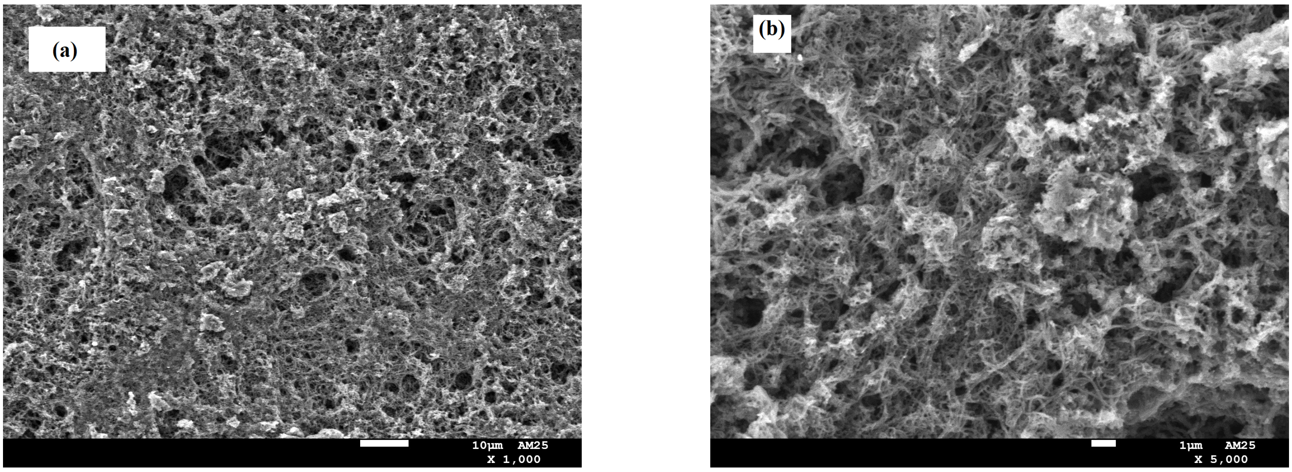

Figure 3.8: SEM images of HCl-Doped PANI thin film deposited on graphite substrate.

To improve performance, the polymer surfaces were modified by electrochemical deposition of Cu_2O, a semiconductor with a direct band gap of 2,34eV. This material, valued for its chemical stability, low cost, and compatibility with both organic and aqueous environments, is a promising candidate for the electrochemical reduction of CO_2 [89, 90]. The SEM images after Cu_2O deposition (3.9.a and 3.9.b) reveal a homogeneous coverage of the substrate by fine white nanoparticles corresponding to Cu_2O. However, the appearance of the resulting thin films strongly depends on the nature of the substrate surface. More specifically, the figures highlight a porous and spongy structure, consisting of a complex and interconnected network. This texture, characteristic of polyaniline films, presents a high specific surface area, making the composite particularly suitable for electrochemical applications such as photocatalysis.

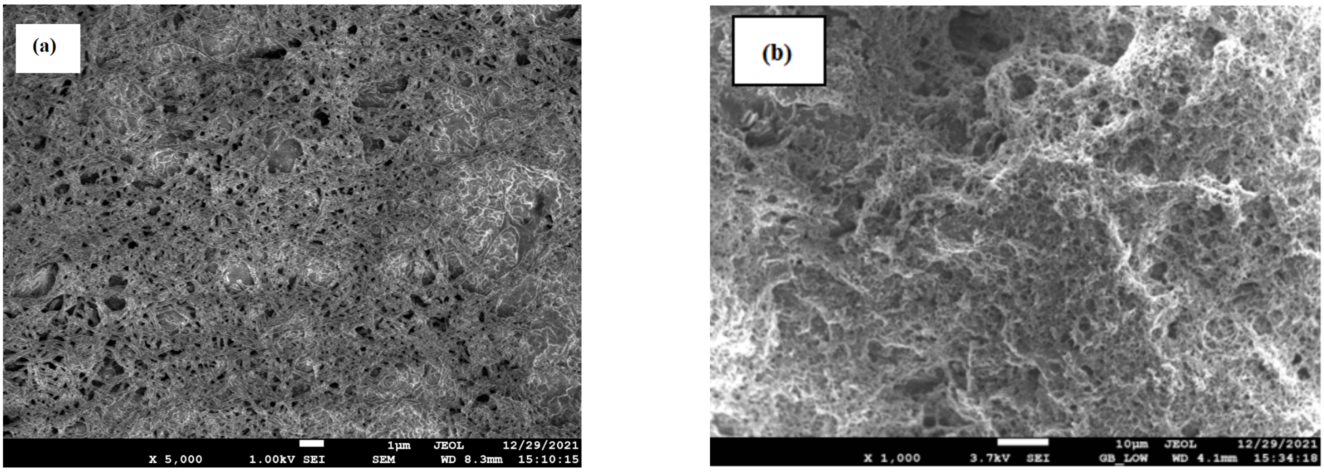

Figure 3.9: SEM images of Cu_2O/HCl-PANI thin film deposited on graphite .

The Energy Dispersive X-ray Spectroscopy spectrum shown in figure 3.10 corresponds to the surface analysis of our HCl-doped pani deposited on a graphite substrate. The dominant carbon peak is attributed to both the graphite substrate and the organic backbone of PANI. The presence of nitrogen and oxygen confirms the characteristic functional groups of the polyaniline structure. Notably, chlorine is also detected in the spectrum, which is consistent with the known doping of PANI using hydrochloric acid. The incorporation of Cl^- ions plays a key role in enhancing the conductivity of the polymer. The elemental composition derived from the EDS analysis is presented in the table 3.2.

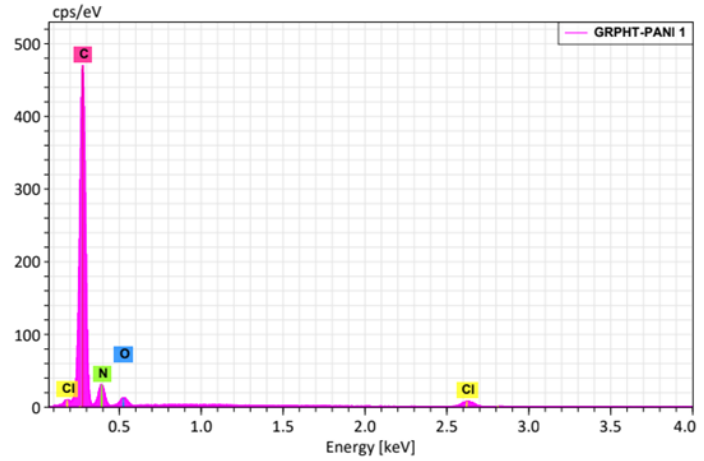

Figure 3.10: EDS spectra of HCl-Doped PANI deposited on graphite substrate.

Table 3.2: Elemental composition of HCl-doped PANI using EDS analysis

Element	Mass [%]	Atom [%]
Carbon	73.60	80.81
Nitrogen	13.87	13.05
Chlorine	9.29	3.45
Oxygen	3.25	2.68
Total	100.00	100.00

3.5 Electron probe microanalysis (EPMA)

Three chemical composition analyses were performed by electron probe microanalysis (EPMA) on our samples to confirm the composition of the deposited layers. Unlike the EDS technique, which provides a localized analysis, EPMA allows the determination of the volumetric composition of the deposits, thus offering a more representative characterization.

Figure 3.11 illustrates the morphology of the layer analyzed by EPMA on a selected area, obtained from three different tests. Figure 3.12 shows the characteristic spectra of the elements present in the deposit. The results of the chemical composition of HCl-doped polyaniline are summarized in Table 3.3 below.

The chemical analysis by EPMA confirms that the layer obtained by electrodeposition corresponds to the doped form of polyaniline, emeraldine salt. The presence of carbon and nitrogen is observed, with respective atomic concentrations of 25.5556% and 67.7996%, originating from the aniline monomer. Chlorine, resulting from doping with hydrochloric acid, is detected at an atomic concentration of 1.3362%. Finally, the presence of oxygen, at 5.3086%, is attributed to the water contained in the electrolytic solution.

Table 3.3: Chemical composition of the layer by EPMA

Element	**Mass %**	**Atomic %**
C	62.414	67.7996
N	27.444	25.5556
O	6.511	5.3086
Cl	3.631	1.3362

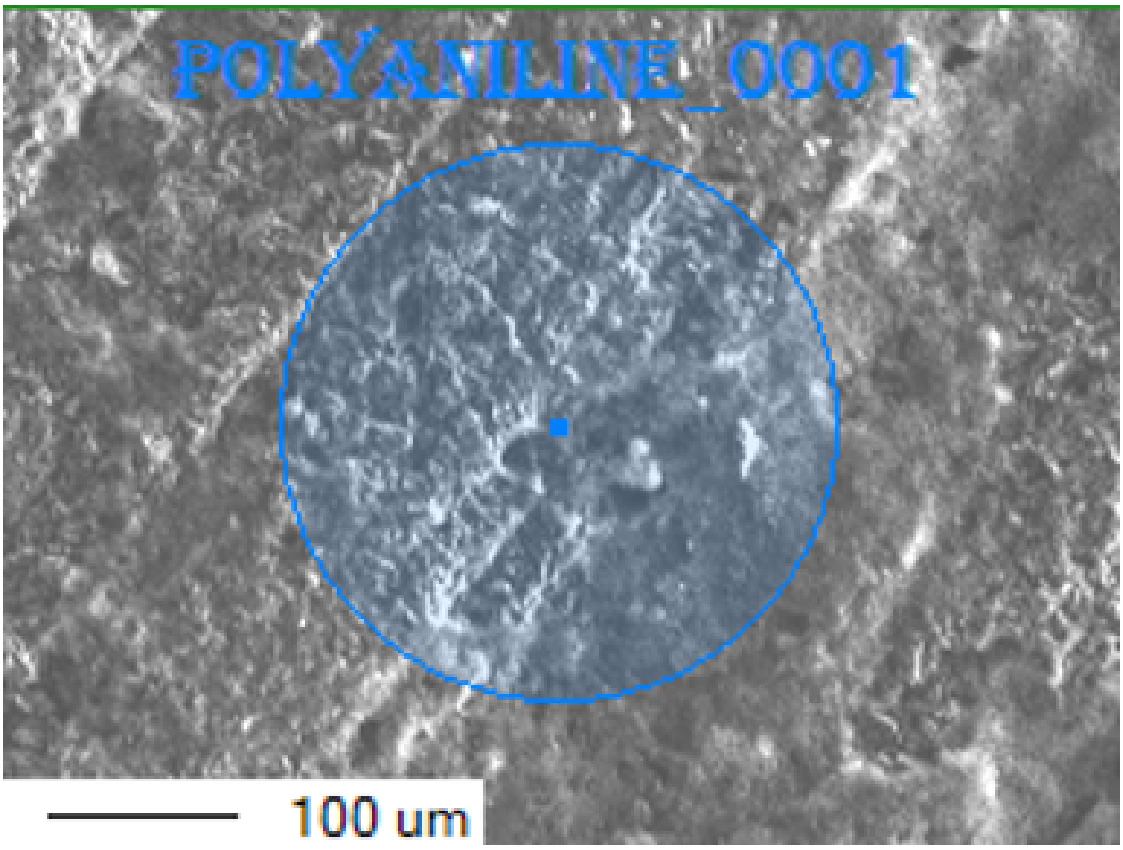

Figure 3.11: Morphology of the layer obtained by EPMA.

.

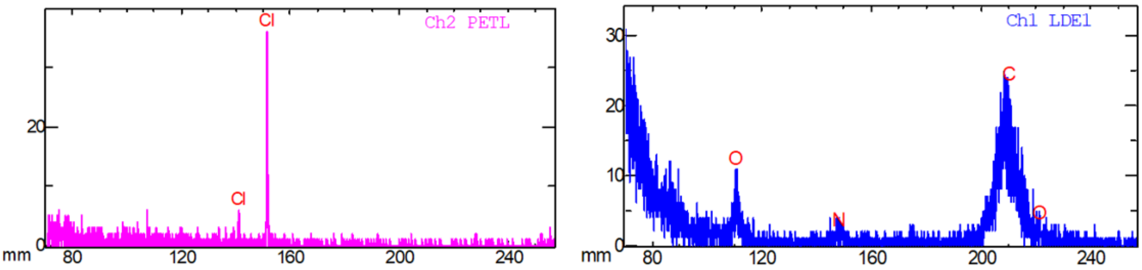

Figure 3.12: characteristic peaks of the chemical elements present in the layer.

3.6 X-Ray Diffraction (XRD):

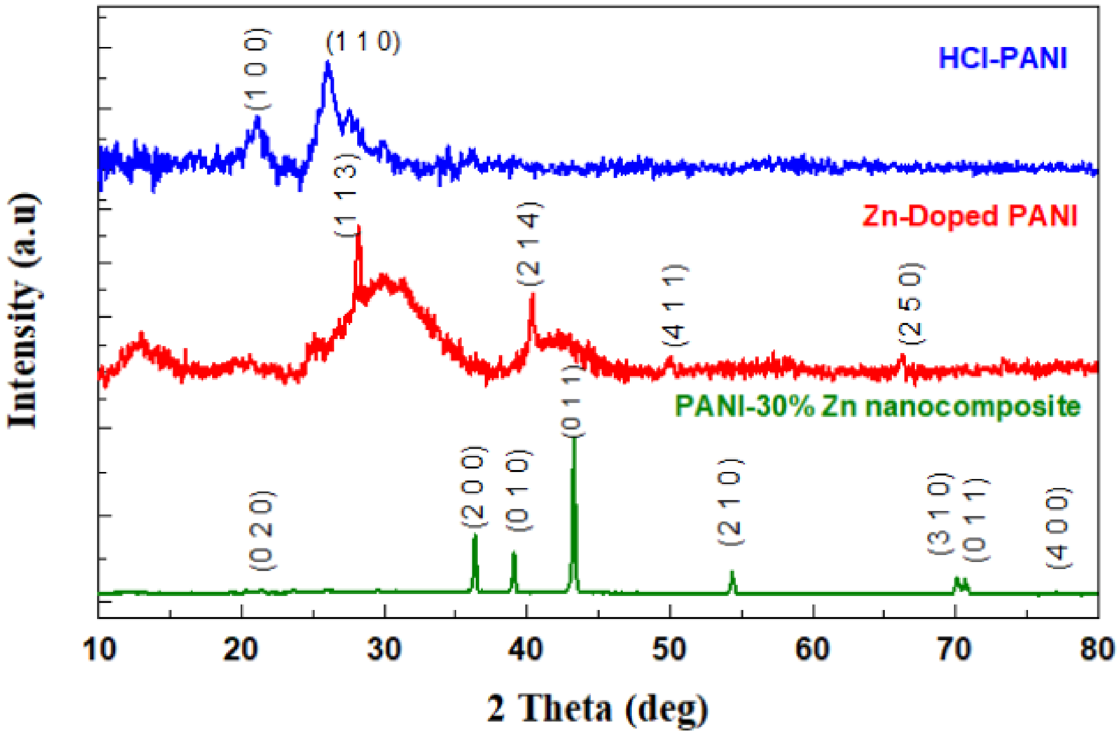

Figure 3.13: X-Ray diffraction distribution of Hcl-doped PANI, Zn-Doped PANI and PANI-30% Zn nanocomposite

X-ray diffraction (XRD) analysis was performed to investigate the structural characteristics of HCl-doped PANI, Zn-doped PANI, and the PANI–30%Zn nanocomposite. The XRD pattern of HCl-doped PANI displays features characteristic of a semi crystalline polymer in its emeraldine salt form, with a broad hump at around $2\theta = 20,97^\circ$, with a calculated d-spacing of 4.24 Å, associated with the parallel periodicity of the polymer chains. and a sharper peak at $2\theta = 25,95^\circ$, with a calculated d spacing of 3.43 Å, indicating a well ordered arrangement of polymer chains with perpendicular periodicity. These peaks correspond to the (100) and (110) planes of the PAni chains. This partial crystallinity, estimated at 24.14%, reflects the coexistence of disordered regions and more ordered chain alignments resulting from chain folding or helical structuring. [91, 92]

The XRD pattern of Zn-doped PANI exhibits broad peaks at $2\theta = 12.5^\circ, 20.6^\circ$ and 25°, characteristic of semi crystalline PANI. These humps reflect the polymer's disordered structure. The Range of these features confirms the coexistence of amorphous regions and short range crystalline domains, typical of conducting polymers synthesized via oxidative routes.

several other well defined peaks emerge at specific angles ($2\theta = 28,2^\circ$,$40,1^\circ$, 50°, and 66.2°). These distinct peaks, corresponding to an orthorhombic crystalline phase identified as the $Zn_4N_{24}C_{16}$ (Reference Code 96-711-5195), provide compelling evidence for the formation of a zinc-PANI coordination complex rather than simple physical mixing, stemming from the chemical synthesis of this sample which resulted in an interaction between the zinc ions and the pani matrix.The total crystallinity of Zn-doped PANI is revealed to be around 38.9%.[93]

The XRD pattern of the PANI-30‘% Zn nanocomposite exhibits sharp, intense diffraction peaks, indicative of a highly crystalline material. These peaks were indexed to a hexagonal structure, matching the standard JCPDS reference for metallic zinc (JCPDS 04-0831), confirming the presence of crystalline Zn as the dominant phase. The well-defined peaks at $2\theta = 36.33°(200), 39.02°(010), 43.25°(011), 54.35°(210), 70.10°(310), 70.67°(011)$, and 77.08° (400) correspond to the hexagonal close-packed (hcp) lattice of metallic zinc, demonstrating that the crystalline structure of Zn remains unmodified despite its integration into the PANI matrix, a direct result of the mechanical powder mixing synthesis method.

In contrast, a broad, low-intensity peak centered at $2\theta \sim 21°$ is attributed to the semi crystalline nature of PANI, attributed to the parallel periodicity of the PANi chains, and specifically assigned to the (020) crystallographic plane in literature[94]. The obvious difference in peak sharpness between the metallic Zn and PANI phases suggests either :

- a higher relative abundance of crystalline Zn compared to ordered PANI domains.
- the inherently amorphous character of PANI in this composite.

Collectively, the XRD data confirm the successful formation of a nanocomposite comprising crystalline metallic zinc embedded within a semi-crystalline PANI matrix. The coexistence of sharp Zn reflections and a broad PANI hump highlights the composite's dual phase nature, where Zn retains its crystallinity while PANI adopts a predominantly disordered structure. [95]

3.7 X-ray Photoelectron Spectroscopy (XPS)

X-ray photoelectron spectroscopy (XPS) was employed to investigate the surface chemical composition and electronic structure of PANI synthesized via chemical and electrochemical methods, as shown in Figure 3.14 and quantified in table 3.4. The full XPS survey spectra confirm the presence of key elements typical of polyaniline-based materials, namely carbon (C 1s), nitrogen (N 1s), and oxygen (O 1s), along with minor contributions from sulfur (S 2p), likely originating from synthesis precursors or residual dopants.Both materials exhibit comparable elemental compositions, confirming the successful formation of doped polyaniline structures by both synthetic routes. A more detailed analysis of the high resolution spectra provides critical insights into the chemical environment of the surface functional groups.

The C 1s spectra of PANI prepared by chemical synthesis (Figure 3.14.b) display three distinct components: $C-C/C-H$ bonds at $\sim$ 284.7 eV, C-O bonds at $\sim$ 286.1 eV, and O-C=O bonds at $\sim$ 288.5 eV [96, 97]. The predominant presence of $C-C/C-H$ species (69.34%) suggests a well preserved conjugated backbone, essential for maintaining good electrical conductivity [98]. In contrast, PANI-HCl obtained by electrochemical synthesis (Figure 3.14.e) exhibits a significantly higher fraction of oxygenated carbon species ($C-O$: 30.28%), reflecting an increased degree of surface oxidation. Such oxygen functionalities can enhance the hydrophilicity of the material and promote stronger interactions with CO_2 molecules, thereby facilitating their activation and conversion [99].

The N 1s spectra provide further evidence of structural differences between the two materials. For the chemically synthesized PANI (figure 3.14.c), the dominant peak at $\sim$ 399.8 eV corresponds to imine nitrogen (=N-), representing 71.19% of the total nitrogen content. This high proportion of imine species indicates a relatively ordered, semi-oxidized emeraldine form of PANI, which is highly conductive and electroactive [100, 101]. The presence of amine nitrogen ($-NH-$, 14.93%) and protonated nitrogen species (N^+, 13.89%) indicates partial oxidation and self-doping of PANI, generating intrinsic charge carriers critical for electrocatalytic activity [102]. In contrast, the electrochemically synthesized PANI-HCl (Figure 3.14.f) exhibits a more balanced distribution of nitrogen species, with a lower proportion of imine nitrogen (48.06%) and increased contributions from both amine (34.64%) and protonated nitrogen (17.30%) species. The higher content of N^+ sites is particularly beneficial for CO_2 reduction, as these positively charged centers can act as active sites for the stabilization of reaction intermediates [103].

The O 1s spectra (Figures 3.14.d and 3.14.g) reveal additional differences in surface chemistry. The chemically synthesized PANI shows a significant proportion of physisorbed water species ($H-O-H$: 32.91%) and $C=O$ groups (46.39%), with a smaller contribution from $C-O-N$ species (20.69%) [104, 105]. In contrast, the electrochemically synthesized PANI-HCl exhibits a substantial enrichment in $C-O-N$ functionalities (53.16%) and a reduced presence of water species (14.78%). This increase in oxygen-nitrogen bonded species suggests enhanced surface reactivity and potential formation of more active sites for CO_2 binding and reduction [57].

The quantitative data summarized in Table 3.4 clearly highlight the distinct surface chemistries imparted by the two synthesis methods. The chemically synthesized PANI maintains a highly conjugated structure with limited surface oxidation, while the electrochemical approach introduces a greater degree of functionalization, particularly in terms of oxygenated and protonated nitrogen species. These variations are expected to significantly influence the electrocatalytic behavior of the materials, with the electrochemically synthesized PANI-HCl potentially offering enhanced catalytic activity for CO_2 reduction due to its higher density of active surface functionalities and improved wettability.

Table 3.4: Elemental composition (atomic %) of each bonding environment in PANI synthesized by chemical and electrochemical methods.

	C 1s			N 1s			O 1s		
	C–C	C–O	O=C–O	=N–	–NH–	N^+	C–O–N	C=O	H–O–H
PANI Chemical method	69.34	11.26	19.40	71.19	14.93	13.89	20.69	46.39	32.91
PANI Electrochemical method	52.98	30.28	16.74	48.06	34.64	17.30	53.16	32.05	14.78

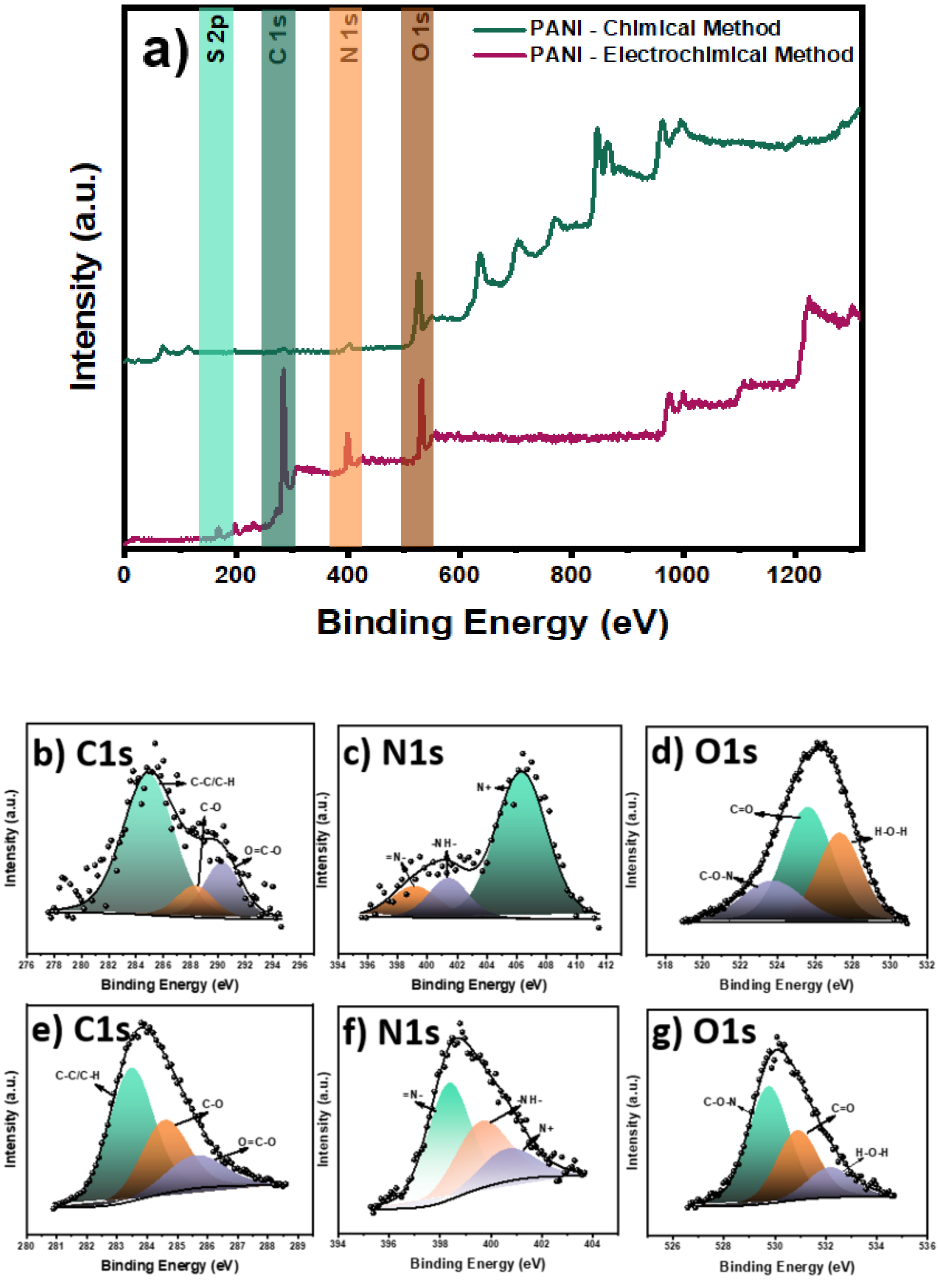

Figure 3.14: XPS survey and high resolution spectra of PANI-HCl synthesized via chemical and electrochemical methods: (a) full survey spectra; high resolution C 1s (b,e), N 1s (c,f), and O 1s (d,g) spectra for PANI obtained by chemical method (b,c,d) and electrochemical method (e,f,g).

3.8 UV-Visible

UV-Visible spectrophotometry is a technique used to study groups of atoms capable of absorbing electromagnetic radiation. Depending on the range of absorbed wavelengths, several domains are distinguished: ultraviolet (200–400 nm), visible (400–750 nm), and near-infrared (750–1400 nm).

Reflectance measurements were carried out using a UV-visible-near infrared spectrophotometer (CARY 500 - VARIAN type, CRTSE, Algiers), capable of analyzing total reflectance over a wavelength range from 300 to 2500 nm. Analysis of the powders' reflectance spectra, presented in Figures 3.15 and 3.16, reveals the presence of interference fringes, attributed to multiple reflections occurring at the powder's surface.

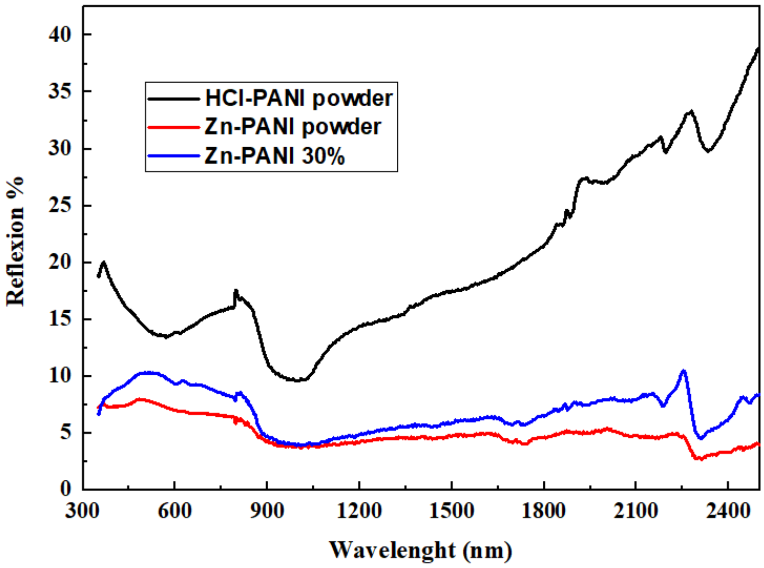

Figure 3.15: Reflexion spectra of powders: HCl-PANI, Zn-PANI, and PANI-Zn 30%.

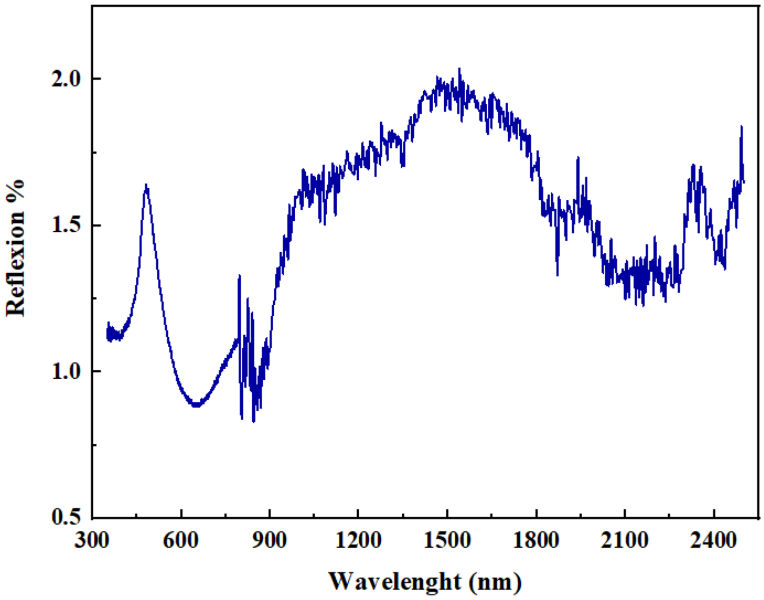

Figure 3.16: Reflexion spectra of HCl-PANI/C_{gr}

3.8.1 Optical band gap

The band gap energy of a semiconductor describes the energy needed to excite an electron from the valence band to the conduction band. An accurate determination of the bandgap energy is crucial in predicting photo physical and photochemical properties of semiconductors. In particular, this parameter is often referred to when photocatalytic properties of semiconductors are discussed The absorption coefficient (α), at the corresponding wavelengths, is calculated using the Schuster-Kubelka-Munk function[106]:

$$\alpha = \frac{(1-R)^2}{2R} \tag{3.1}$$

where R is the reflection. The photon absorption in many amorphous materials is found to obey the Tauc relation, which is of the form:

$$(h\nu)^n = A.(h\nu - E_g) \tag{3.2}$$

Where $h\nu$ is the energy of the incident photon :

$$h\nu(eV) = h.c = \frac{1240}{\lambda(nm)} \tag{3.3}$$

E_g is the optical energy band gap, A is a constant known as the disorder parameter which is nearly independent of the photon energy parameter, and n is the power coefficient with the value that is determined by the type of possible electronic transitions. For the direct and indirect allowed transition = 2 or ½ , respectively. Figure 3.17 shows the reflectance spectrum transformed according to equation (3.2) plotted against the photon energy.

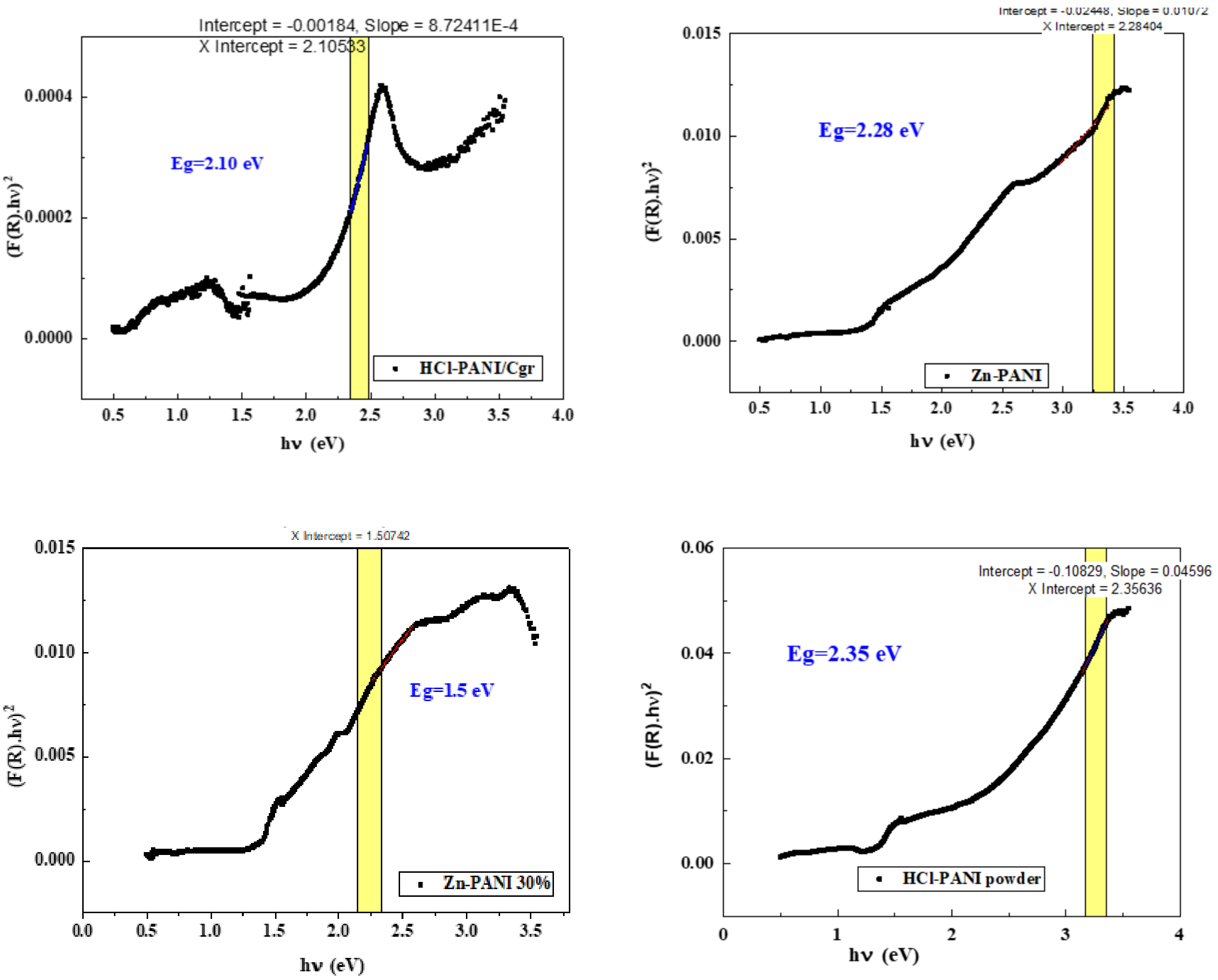

Figure 3.17: Determination of the optical band gap of the different forms of PANI

The x-axis intersection point of the linear fit in the Tauc plot provides an estimate of the band gap energy. The analysis of the obtained optical gap values shows a range from 1.5 to 2.35 eV. These results are consistent with values reported in the literature. This band gap value is very satisfactory based on research conducted for the application of our electrodes in CO_2 conversion.[107]

Part B: Electrochemical characterization and application in the electroreduction of CO_2

3.9 Electrocatalytic activity assessment

The performance of the various prepared electrodes for electrocatalytic CO_2 reduction was evaluated using a multi-technique electrochemical approach combining linear sweep voltammetry (LSV), cyclic voltammetry (CV), and chronoamperometry. This integrated methodology enabled a detailed investigation of the CO_2 electroreduction process.

- **Linear Sweep Voltammetry:** This technique provides critical insights into the electrocatalytic and photoelectrocatalytic behavior of the materials, particularly within the context of the CO_2 reduction reaction (CO_2RR).
- **Cyclic Voltammetry:** CV is especially useful for identifying the onset potential of CO_2 reduction and detecting the electrochemical signature associated with this process.
- **Chronoamperometry:** This method is employed to assess the operational stability of the electrodes and the reaction kinetics by applying a constant potential while monitoring the current variation over time.

All measurements were conducted over a potential range of [-1.5 V to +0.5 V] at a scan rate of 10 $mV \cdot s^{-1}$, using an Autolab potentiostat/galvanostat controlled via NOVA 2.1 software, under ambient temperature conditions.

The Figures 3.18a–3.18d illustrate the electrochemical behavior of graphite electrodes modified with thin layers of hydrochloric acid-doped polyaniline (HCl-PANI), copper(I) oxide (Cu_2O)/HCl-PANI and $\text{PANI}_{\text{undoped paste}}$ (chemically synthesized) . The electrochemical responses were recorded in two distinct electrolytic environments: an alkaline 0.1 M NaOH solution and a 0.5 M K_2CO_3 solution.

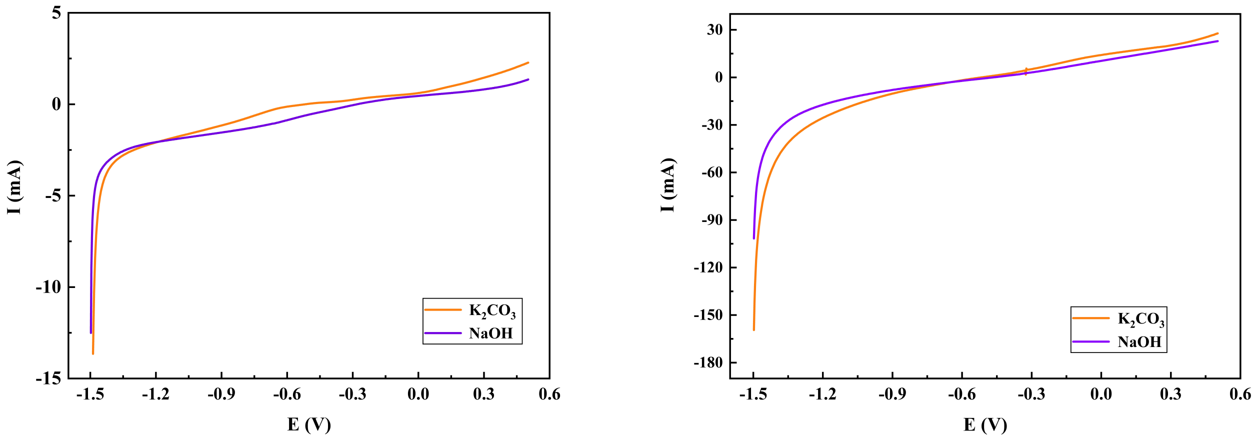

(a) LSV of chemically synthesized PANI (undoped paste).

(b) LSV of Cu_2O/HCl doped PANI-modified graphite electrode.

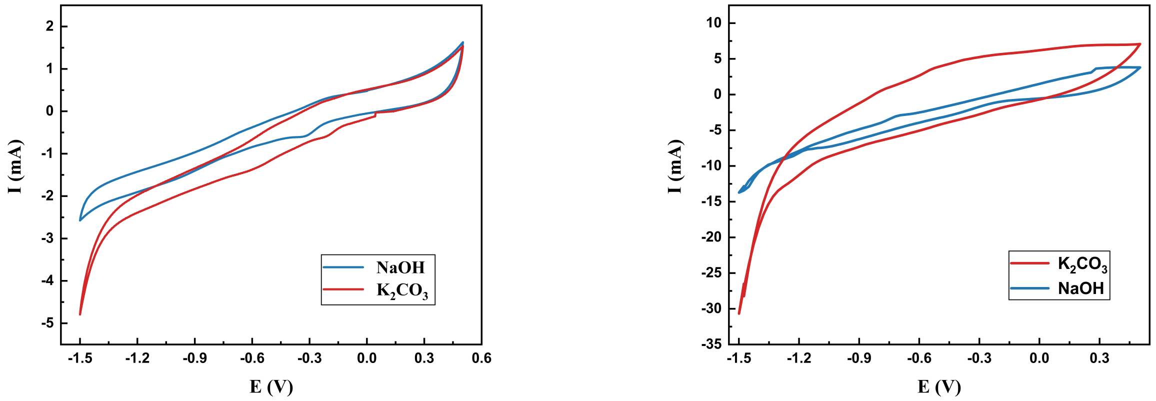

(c) CV of chemically synthesized PANI (undoped paste).

(d) CV of HCl doped PANI-modified graphite electrode.

Figure 3.18: Comparative voltammetric profiles of graphite-based electrodes modified with PANI or Cu_2O/HCl-PANI in alkaline (0.1 M NaOH) and carbonated (0.5 M K_2CO_3) electrolytes.

The analysis of the voltammograms revealed that the electrochemical behavior of PANI varies significantly with the nature of the electrolyte. In particular, the use of K_2CO_3 allows the system to mimic realistic operating conditions where CO_2 is present—either as an industrial emission or from ambient air. In aqueous media, carbonate ions ($CO_3{}^{2-}$) are in equilibrium with dissolved carbon dioxide via the following reaction:

$$CO_3^{2-} + 2H^+ \rightleftharpoons CO_2 + H_2O \tag{3}$$

Accordingly, the presence of $CO_3{}^{2-}$ ions—supplied by potassium carbonate (K_2CO_3)—ensures an equilibrium concentration of CO_2 within the solution, enabling CO_2 reduction without the need for direct gas-phase CO_2 injection.

The voltammetric curves shown in Figure 3.18 clearly demonstrate distinct behaviors in the alkaline and carbonate electrolytes, suggesting that PANI acts as an electrocatalytically active material in the presence of K_2CO_3, facilitating CO_2 conversion. However, no well-defined current peaks were observed, which may suggest that CO_2 reduction proceeds via diffuse mechanisms or through complex multi-step pathways.

3.10 Evolution of CO_2 reduction on different electrodes

To assess the electrocatalytic performance of the different photocathodes used as working electrodes, we performed (I–V) characterizations (both linear and cyclic) as well as chronoamperometric measurements (I–t). These techniques aimed to evaluate the electrocatalytic activity via voltammetry and the long-term stability of the materials through chronoamperometry. This comprehensive analysis enabled the comparative ranking of electrode performance for CO_2 electroreduction.

Comparative analysis of electrode performance

3.10.0.1 Graphite electrode

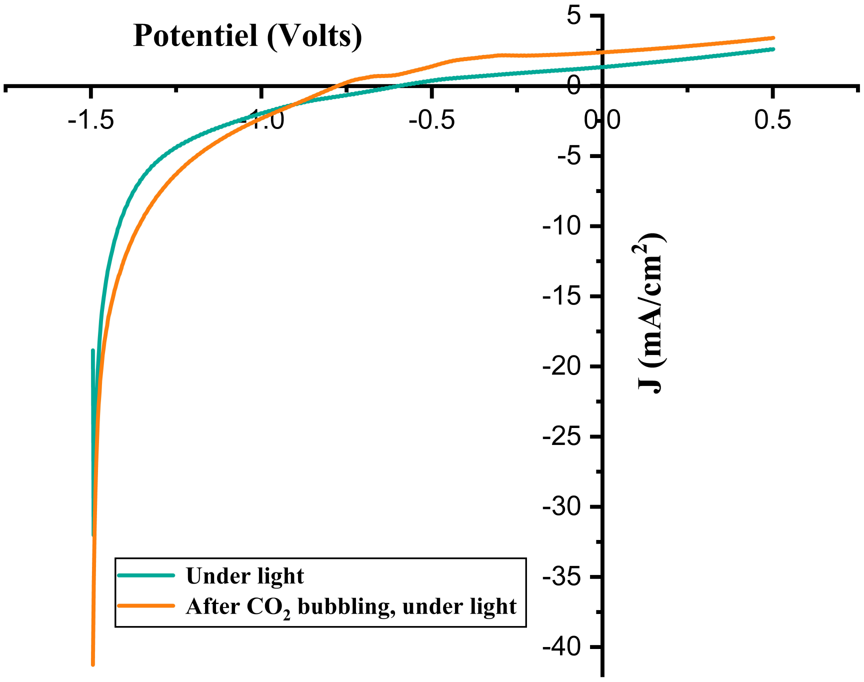

Figure 3.19: LSV curves of cylindrical graphite in 0.5 M K_2CO_3 electrolyte, recorded under sunlight illumination, with and without CO_2 saturation, at a scan rate of 10 mV · s^{-1}

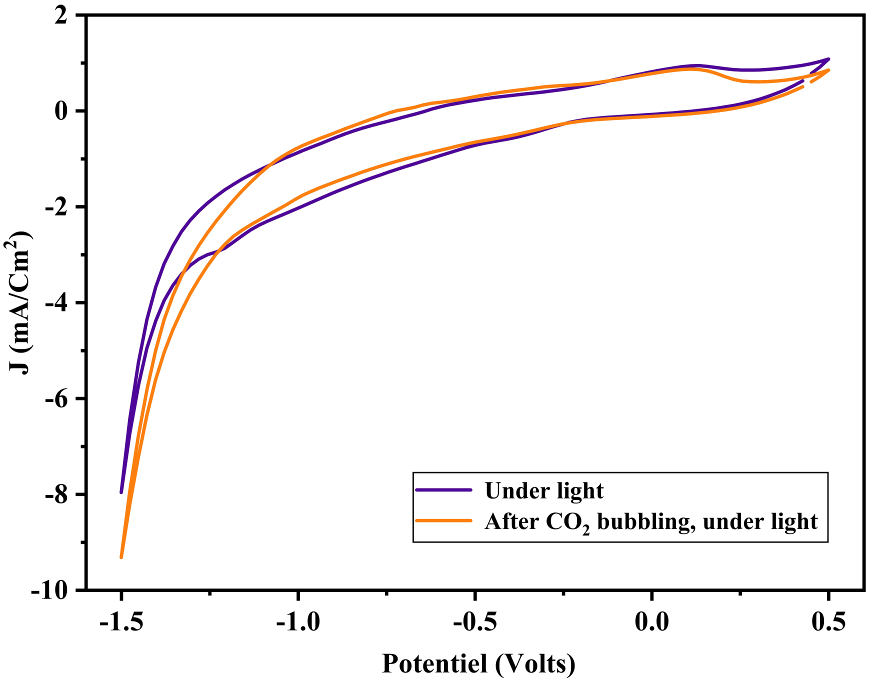

Figure 3.20: CV curves of cylindrical graphite in 0.5 M K_2CO_3 electrolyte, under solar illumination, comparing the electrochemical response in the presence and absence of CO_2, at a scan rate of 10 mV · s^{-1}

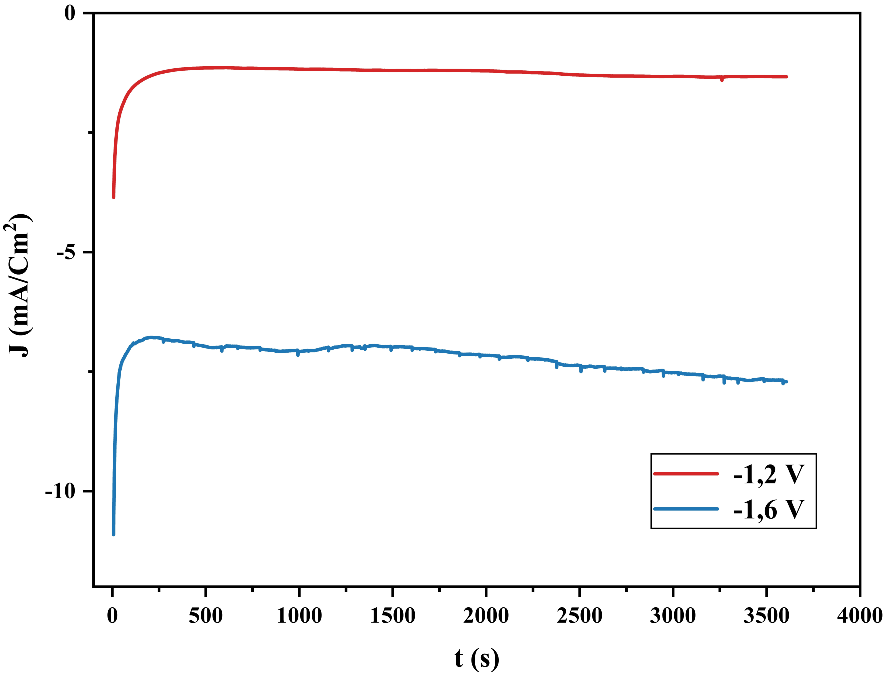

Figure 3.21: Chronoamperometric response of graphite electrode in 0.5 M K_2CO_3 as a function of the applied potential under CO_2 atmosphere

3.10.0.2 HCl-Doped PANI thin films on Graphite electrode

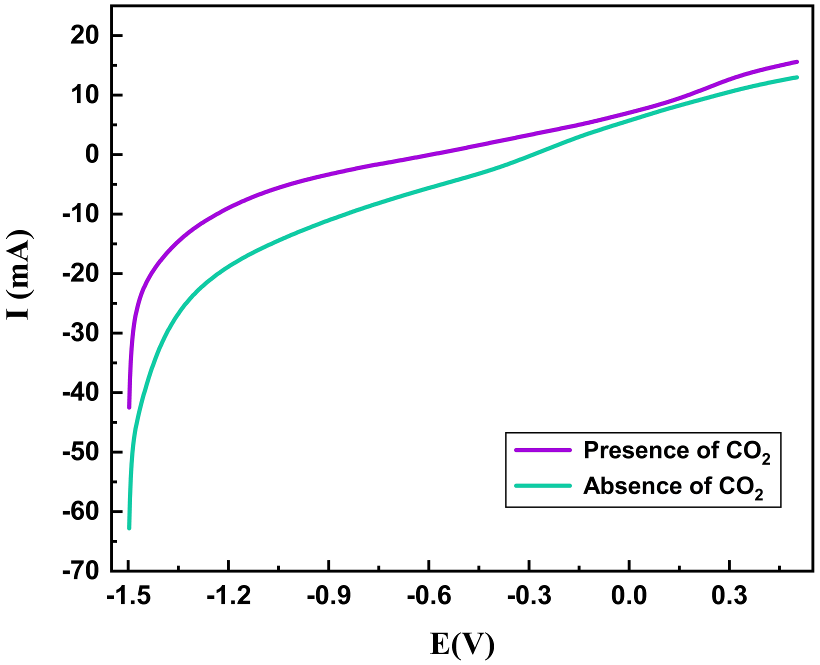

Figure 3.22: LSV curves of HCl–PANI/graphite electrode in 0.5 M K_2CO_3 electrolyte, under sunlight illumination, in CO_2-saturated/free environments, at a scan rate of 10 mV · s^{-1}

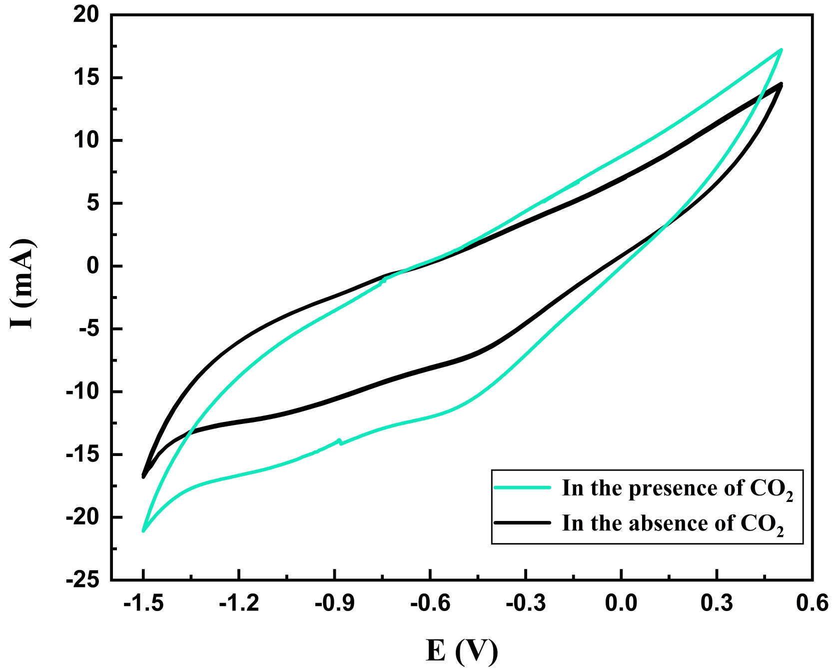

Figure 3.23: CV curves of HCl–PANI/graphite electrode in 0.5 M K_2CO_3 electrolyte, under constant illumination, comparing the electrocatalytic response with and without CO_2 saturation

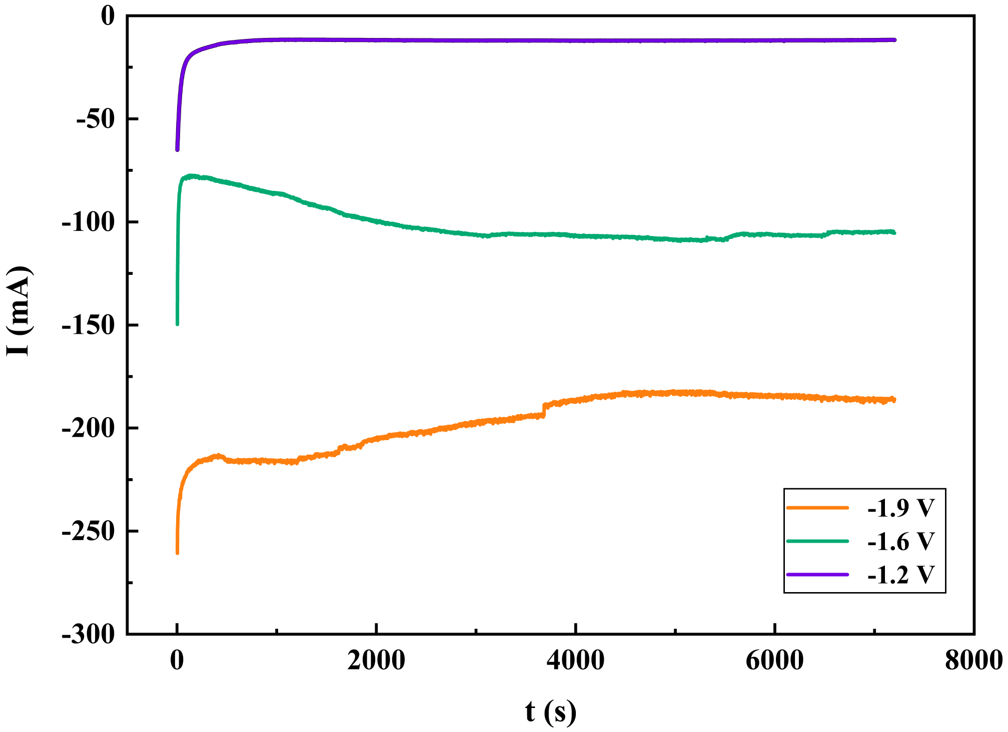

Figure 3.24: Chronoamperometric characterization of HCl–PANI/graphite electrode in 0.5 M K_2CO_3 electrolyte under CO_2 atmosphere as a function of applied potential

3.10.0.3 Bilayer of Cu_2O on HCl-doped PANI on Graphite electrode

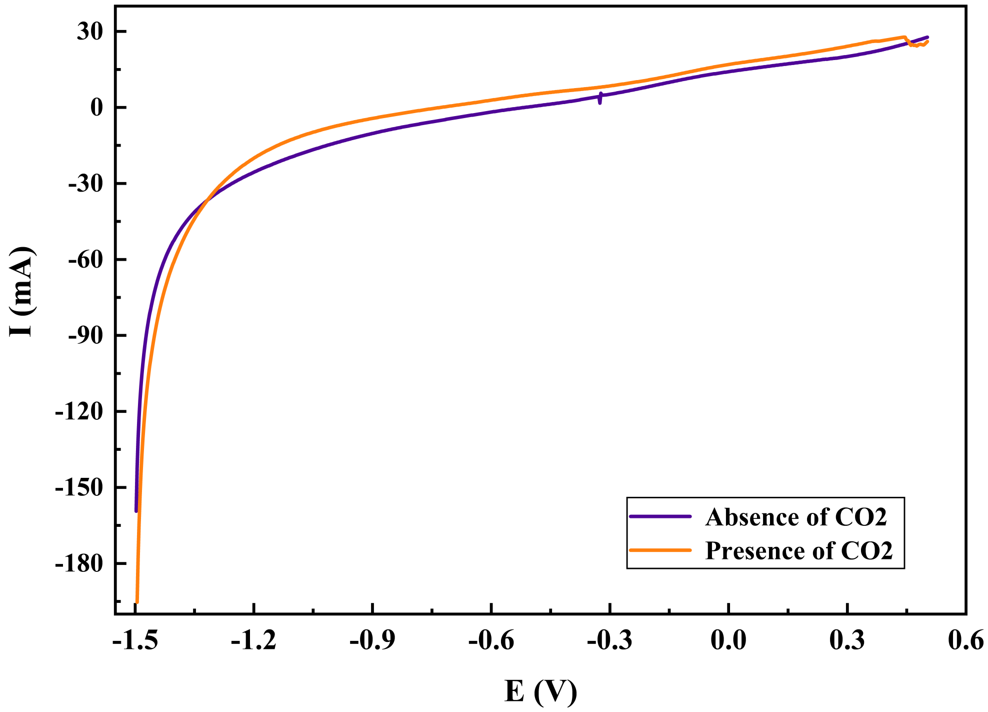

Figure 3.25: LSV curves of Cu_2O/HCl–PANI electrode on graphite in 0.5 M K_2CO_3 electrolyte, under sunlight illumination, in the presence and absence of CO_2, at a scan rate of 10 mV · s^{-1}

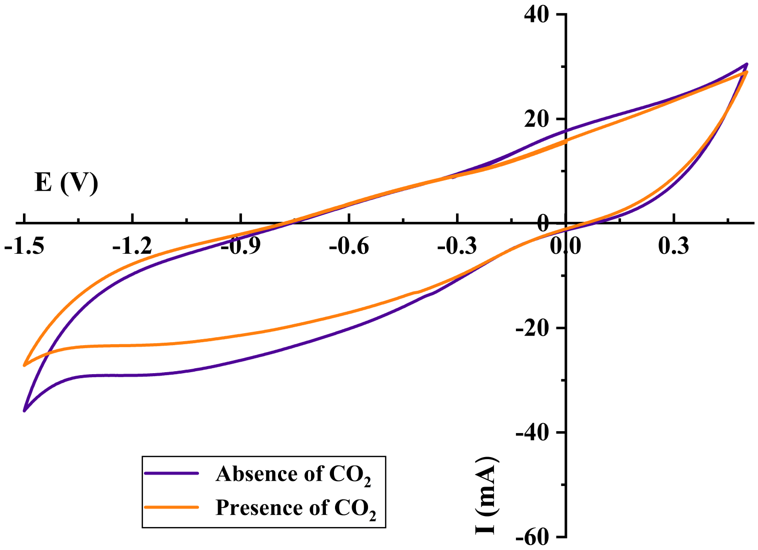

Figure 3.26: CV curves of Cu_2O/HCl–PANI/graphite electrode in 0.5 M K_2CO_3 electrolyte, under solar illumination, comparing the electrocatalytic behavior with and without CO_2

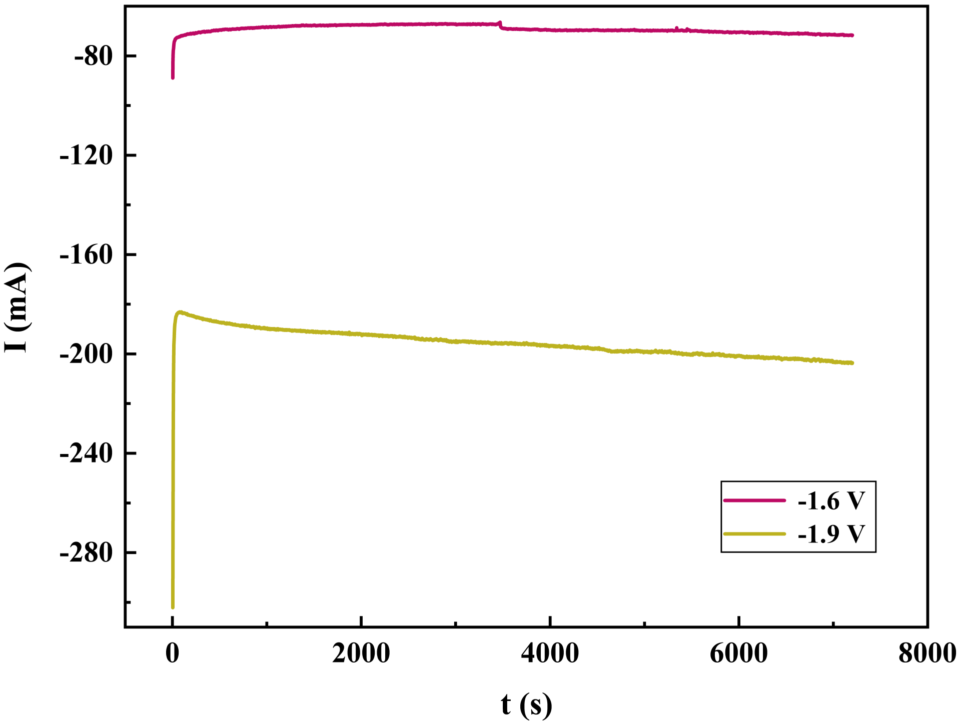

Figure 3.27: Chronoamperometric profile of Cu_2O/HCl–PANI/graphite electrode in 0.5 M K_2CO_3 electrolyte under CO_2 atmosphere as a function of the applied potential

Experiments were carried out in two conditions: a 0.5 M potassium carbonate (K_2CO_3) solution and the same solution saturated with CO_2 for 30 minutes prior to measurement. The tests were performed at a basic pH of approximately 11.6, under ambient temperature and pressure, using natural sunlight as the illumination source. The applied scan rate for all voltammetric measurements was 10 $mV \cdot s^{-1}$.

Comparing the voltammograms recorded in CO_2-saturated and unsaturated K_2CO_3 solutions revealed no distinct cathodic or anodic peaks; however, the presence of dissolved CO_2 led to marked changes in the voltammetric profiles. These included the emergence of anodic bands and shifts in cathodic photocurrent onset, indicative of redox activity influenced by CO_2 species [108, 109].

The CV response of HCl-PANI (Figure 3.23) exhibited higher oxidation and reduction currents under CO_2 saturation, strongly suggesting its active role in CO_2 conversion. This behavior implies the formation of reduction products such as formic acid or methanol. Similarly, the CV of Cu_2O-modified HCl-PANI electrodes (Fig. 3.26)demonstrated pronounced increases in both anodic and cathodic currents in the presence of CO_2, accompanied by broader redox peaks. This broadening implies enhanced electron transfer kinetics and a more extensive CO_2 reduction process, likely involving multi-step electron transfers leading to valuable products.

These broadened voltammetric loops suggest quasi-reversible processes—characteristic of systems where electrochemical transformations are coupled with slower chemical steps. Altogether, the data confirm the superior electrocatalytic activity of the Cu_2O/HCl-PANI/Cgr hybrid electrode in promoting CO_2 reduction.

The general increase in cathodic current, along with observable changes in voltammetric response under CO_2, further supports the hypothesis that the tested electrodes facilitate CO_2 electroreduction. The mechanism likely involves kinetically complex processes extending over a wide range of overpotentials.

LSV analysis in 0.5 M K_2CO_3 showed significant evolution in cathodic current density, particularly under CO_2 - saturated conditions compared to the blank electrolyte. This trend confirms the occurrence of CO_2 reduction reactions, driven by the electrochemical characteristics of the electrode surfaces. By examining the onset potentials and current profiles, the occurrence and kinetics of CO_2RR could be confirmed.

Notably, the LSV profile of HCl-PANI in Figure 3.22 revealed a marked enhancement in cathodic current under CO_2, especially in the negative potential domain, indicating effective CO_2 activation. This performance is attributed to the intrinsic conductivity and redox activity of the emeraldine form of PANI, which facilitates electron transfer to CO_2 molecules.

The Cu_2O/PANI electrode displayed a substantial cathodic current increase in the presence of CO_2 (Figure 3.25), particularly beyond -0.9 V, revealing additional electrochemical activity directly tied to CO_2 reduction. This increase underscores the catalytic effectiveness of the Cu_2O/PANI composite system.

To evaluate photoelectrochemical stability, chronoamperometry was conducted at fixed cathodic potentials (-1.2 V, -1.6 V, and -1.9 V) for 7200 s. Prior to each test, the electrolyte was saturated with pure CO_2 for 30 minutes. The chronoamperometric curves in Figures 3.24 and 3.27 exhibited a steady increase in current under visible light irradiation, eventually reaching a plateau—indicative of electrode activation and stabilized photoelectrocatalytic performance.

The incorporation of Cu_2O into the PANI matrix not only improved the stability but also enabled faster equilibrium. Cu_2O, with a bandgap of $\sim 2.35\ eV$ [110], produces photogenerated electrons of sufficient energy to participate in CO_2 reduction. Its contribution to visible light absorption and carrier separation makes it an effective co-catalyst for PANI-based systems.

Finally, chronoamperometric data at -1.2 V and -1.6 V showed nearly identical current densities, implying that the system reaches its optimal catalytic performance within this potential range—combining high activity with stable operation.

3.11 Gas Chromatography

The analysis of the two electrolytic solutions obtained at the end of the photoelectrochemical process was carried out by gas chromatography (GC) at the LCAGC laboratory of the Faculty of Sciences at UMMTO in Tizi-Ouzou. The instrument used was equipped with two detectors: a thermal conductivity detector (TCD) and a flame ionization detector (FID), enabling sensitive and specific detection of volatile compounds present in the samples.

The results of this analysis are presented in Figures 3.28 and 3.29. The chromatograms reveal a distinct peak corresponding to methanol in both samples, indicating that methanol is the primary identifiable product of the reaction. This identification is based on prior calibration of methanol, allowing for precise quantification of this compound. However, the absence of standards for other potential products such as ethanol, formic acid, or other organic compounds limits the ability to identify and quantify these substances in the samples. Additionally, the inability to directly couple the electrochemical cell to the GC system prevents real-time monitoring of CO_2 reduction and the detection of gaseous products such as methane and hydrogen. Consequently, these gases could not be quantified after opening the electrochemical cell at the end of each experiment. These limitations highlight the need to develop more comprehensive analytical methods and to have a broader range of standards for an exhaustive characterization of the products from the photoelectrochemical reduction of CO_2.

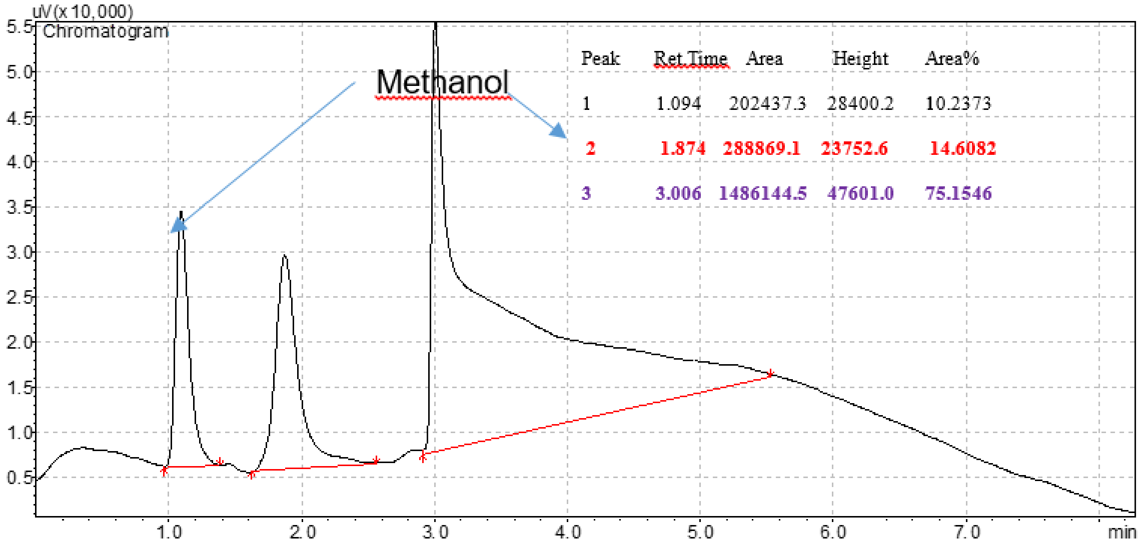

Peak	Ret.Time	Area	Height	Area%
1	1.094	202437.3	28400.2	10.2373
2	1.874	288869.1	23752.6	14.6082
3	3.006	1486144.5	47601.0	75.1546

Figure 3.28: Characteristic peaks of a Gas Chromatograph of the electrolyte after CO2 reduction using PANI/Cgr as photocathode.

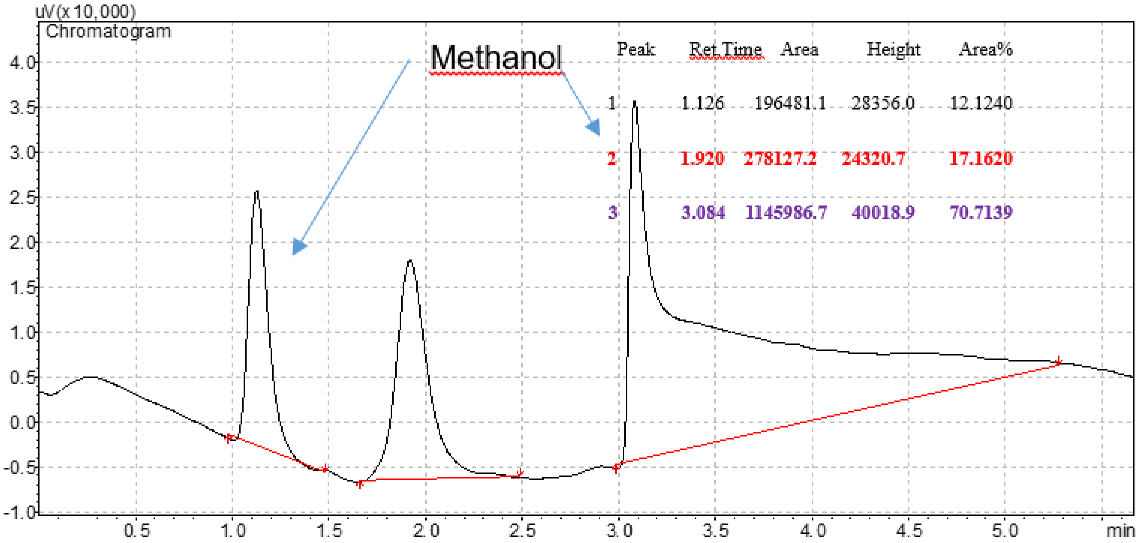

Peak	Ret.Time	Area	Height	Area%
1	1.126	196481.1	28356.0	12.1240
2	1.920	278127.2	24320.7	17.1620
3	3.084	1145986.7	40018.9	70.7139

Figure 3.29: Characteristic peaks of a Gas Chromatograph of the electrolyte after CO2 reduction using Cu2O /PANI/Cgr as photocathode.

The obtained results indicate that modifying the surface of polyaniline (PANI) with a deposit of copper oxide (Cu_2O) films significantly enhances methanol production compared to unmodified PANI. This structure achieved a CO_2 reduction rate of 17.62%, representing the best performance observed, suggesting an increase in faradaic efficiency. This demonstrates that the design of such structures strengthens the working electrode's activity, exerting a positive effect on the electrochemical reduction of CO_2. Compared to the HCl-PANI electrode, the Cu_2O/PANI electrode exhibited superior activity for the electrochemical reduction of CO_2 to methanol, with a maximum faradaic efficiency of 14.608%. These observations suggest that the high yield obtained is attributable to the dispersion of Cu_2O in the polyaniline matrix.

It is reasonable to assume that the Cu^+ ions present in Cu_2O act as active sites promoting CO_2 reduction. In particular, the electronic properties of Cu_2O, a p-type semiconductor, play a crucial role in CO_2 adsorption. The oxygen species in copper oxides increase the number of electronic defects, thereby facilitating CO_2 adsorption on the catalyst's surface [111]. According to some studies, the photocatalytic reduction of CO_2 using TiO_2 loaded with Cu_2O and CuO led to the formation of methanol as the sole reaction product, with the best yield obtained [112]. The integration of Cu_2O into the elaborated heterostructures induces absorption in the visible region by the obtained photocathodes, which contributes to improving their reducing power. According to the work of Park et al. [113, 114], copper oxides significantly increase carbon dioxide adsorption capacity. Since CO_2 is considered a soft acid, copper oxide nanoparticles, endowed with electron-donating properties, promote its adsorption through interaction with its electron-acceptor characteristics. Therefore, the synergistic association between PANI and Cu_2O facilitates CO_2 reduction, while Cu_2O enhances gas adsorption on the surface of the polymer deposited on the graphite support.

In an effort to improve electrocatalytic activity through the incorporation of heteroatoms into the carbon structure, using substitutional doping to modulate the chemical characteristics of a catalyst, a synthesis of PANI-based photocatalysts, Zn-doped PANI, and Zn-PANI nanocomposites in slurry form on graphite was undertaken, where the active material (the semiconducting polyaniline powder) was synthesized via the chemical route.

3.12 Characterization of the chemically synthesized electrodes

3.12.1 Cyclic voltammetry analysis of chemically synthesized Zn-doped Polyaniline (Zn/PANI) under light irradiation

Following the chemical synthesis route, cyclic voltammetry (CV) was employed to evaluate the redox behavior and electrocatalytic response of Zn-doped polyaniline (Zn/PANI) composites under light irradiation. The CV curves obtained in the absence and presence of CO_2 are presented in the figures below. The voltammetric responses of the three formulations (undoped PANI, 20% Zn-PANI, and 30% Zn-PANI) under CO_2-free conditions revealed behavior dominated by Faradaic processes and double-layer charging. Specifically:

- **Undoped PANI** exhibits a weak and diffuse current profile across the potential range. The absence of distinct redox peaks reflects sluggish charge transfer kinetics due to the lack of CO_2 acceptors and doping-induced conductivity enhancement. This behavior corresponds to the intrinsic electroactivity of chemically synthesized PANI, governed by transitions among the leucoemeraldine, emeraldine, and pernigraniline states.
- **Zn-doped PANI** displays an enhanced cathodic current density compared to the undoped version, with a notable increase between -0.6 V and -1.1 V. This suggests improved electronic conductivity attributed to the modulation of the PANI matrix by Zn^{2+} dopants, likely via increased formation of polarons and bipolarons that facilitate charge carrier mobility. The higher the Zn content, the greater the cathodic response—indicative of more effective electronic delocalization within the polymer chains. Elevated Zn_{2+} concentrations enhance electroactivity due to band structure modifications and a higher density of redox-active states arising from Zn coordination, preconditioning the material for superior electrocatalytic functionality.

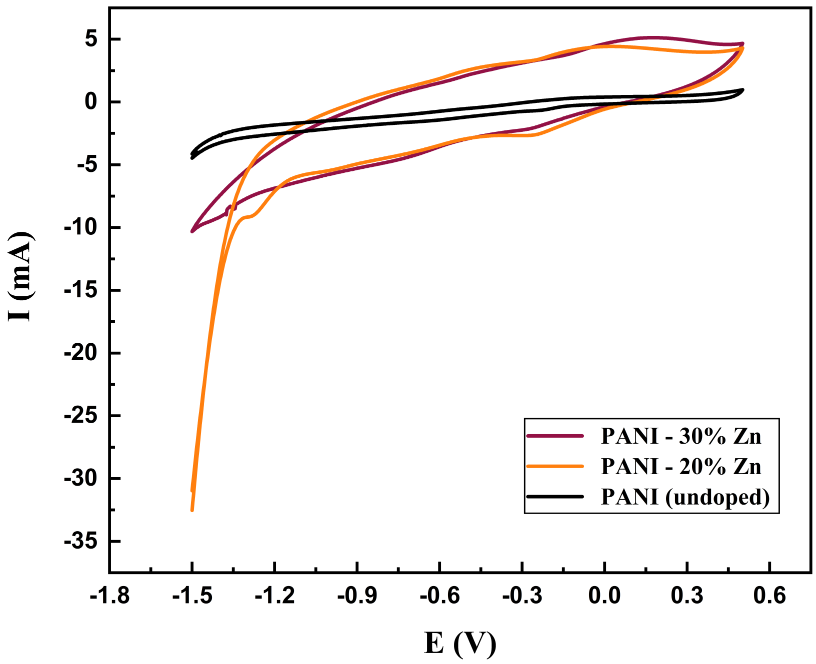

Figure 3.30: Cyclic voltammetry curves of PANI-based electrodes (undoped, 20% Zn, 30% Zn) in 0.5 M K_2CO_3 under illumination, in the absence of CO_2.

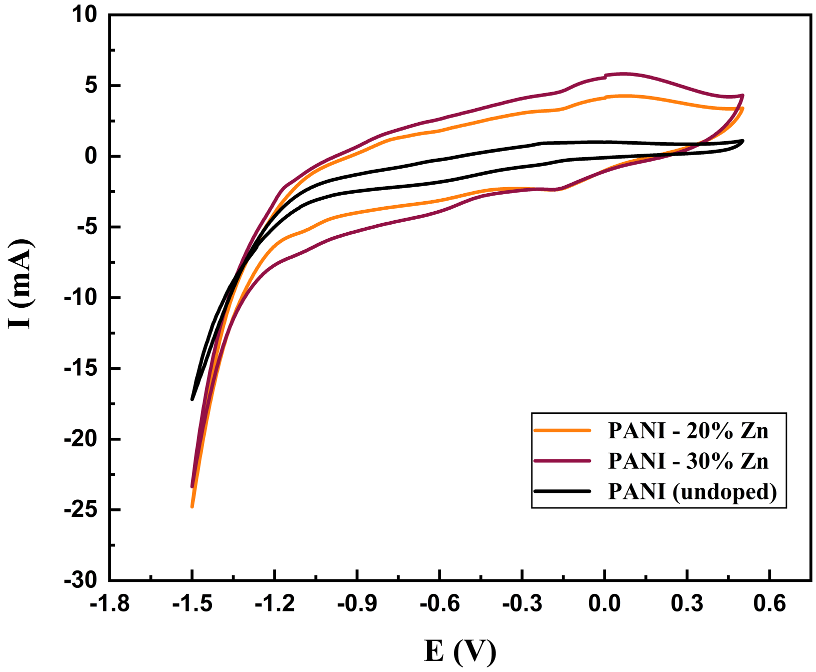

Figure 3.31: Cyclic voltammetry curves of PANI-based electrodes (undoped, 20% Zn, 30% Zn) in 0.5 M K_2CO_3 under illumination, in the presence of CO_2.

Upon introducing CO_2 into the system, a notable increase in cathodic current was observed- particularly in the range from -0.5 V to -1.2 V which indicates a CO_2 reduction activity. The undoped PANI exhibited low catalytic efficiency, attributed to the scarcity of active sites and poor stabilization of CO_2 reduction intermediates. In contrast, the Zn-doped composites, especially with 30% Zn, demonstrated a significantly stronger cathodic response, suggesting improved CO_2 adsorption and facilitated electron transfer for reduction. Zinc plays a pivotal role by enhancing electronic delocalization, stabilizing $^*CO_2$ - intermediates, and modifying the polymer's electronic structure, thereby improving performance even under CO_2 - free conditions.

Compared to the undoped system, Zn doping clearly improves catalytic activity by lowering activation barriers and promoting an efficient redox cycle. The observed order of activity is:

$$30\% \text{ Zn-PANI} > 20\% \text{ Zn-PANI} > \text{undoped PANI} \tag{3.4}$$

This performance trend is attributed to higher charge carrier densities, reinforced π–π stacking, increased electroactive surface area, and favorable $Zn^{2+} - CO_2$ interactions enhancing molecular adsorption and reduction.

3.12.2 Linear Sweep Voltammetry analysis of chemically synthesized Zn-doped PANI Electrodes in CO_2-Free and CO_2-Saturated Environments

LSV was employed to further probe the photocathodic behavior of the Zn-doped PANI systems. Measurements were conducted under visible light illumination in an alkaline 0.5 M K_2CO_3 electrolyte for the undoped and Zn-doped (20% and 30%) PANI samples, both in the absence and presence of CO_2.

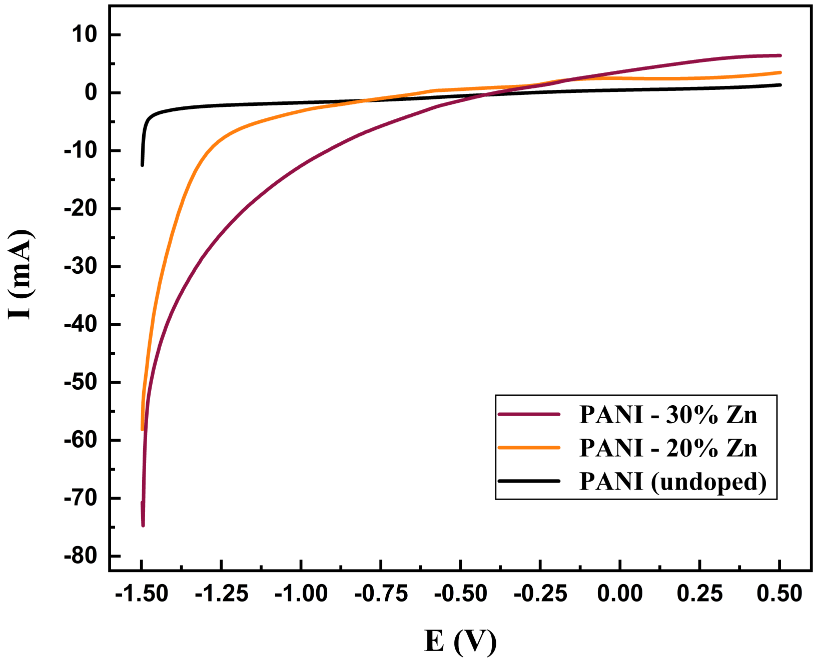

Figure 3.32: Linear sweep voltammetry of PANI-based electrodes (undoped, 20% Zn, 30% Zn) in 0.5 M K_2CO_3 under illumination, in the absence of CO_2.

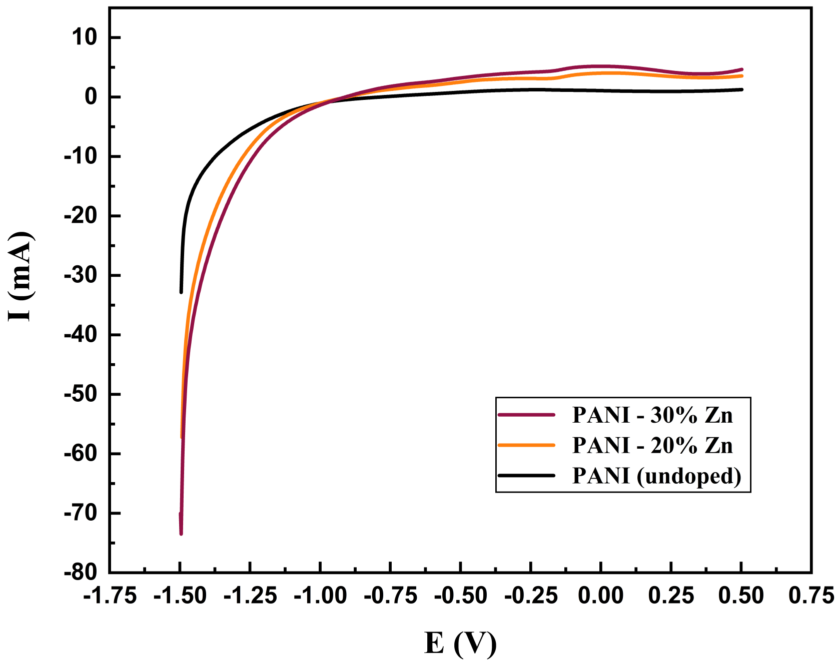

Figure 3.33: Linear sweep voltammetry of PANI-based electrodes (undoped, 20% Zn, 30% Zn) in 0.5 M K_2CO_3 under illumination, in the presence of CO_2.

In both atmospheric and CO_2-saturated environments, all systems exhibited increased cathodic current as the potential shifted more negatively-consistent with charge transfer activity. However, CO_2 saturation resulted in a marked increase in cathodic current for all samples, particularly at potentials below -0.6 V vs. Ag/AgCl, strongly suggesting CO_2 reduction processes.

Undoped PANI showed a modest photocurrent response under both conditions, with only a slight increase in cathodic current upon CO_2 exposure, which is an indicative of low CO_2 adsorption affinity and limited electron transfer capacity in the absence of dopants.

20% Zn-PANI exhibited a significantly higher cathodic current under CO_2, with a slightly more negative onset potential than undoped PANI.

30% Zn-PANI displayed the most pronounced cathodic shift and highest current, pointing to superior catalytic activity and electronic conductivity.

This improvement is attributed to Zn doping, which enhances the conductivity and provides more favorable active sites for CO_2 interaction. The behavior reflects the cumulative effects of Zn incorporation, including modulation of the PANI band structure, facilitation of localized energy states, and an increased density of charge carriers via improved polaron/bipolaron delocalization.

a) Effect of CO_2 saturation and photocatalytic activity

The presence of CO_2 promotes additional Faradaic processes associated with the CO_2 reduction reaction (CO_2RR). The observed enhancement in cathodic current corresponds to multi-electron reduction pathways such as:

$$CO_2 + 2H^+ + 2e^- \rightarrow HCOOH \qquad E^\circ \approx -0.61 \text{ V vs SHE} \tag{3.5}$$

$$CO_2 + 4H^+ + 4e^- \rightarrow HCHO + H_2O \qquad E^\circ \approx -0.48 \text{ V vs SHE} \tag{3.6}$$

$$CO_2 + 6H^+ + 6e^- \rightarrow CH_3OH + H_2O \qquad E^\circ \approx -0.38 \text{ V vs SHE} \tag{3.7}$$

In an alkaline K_2CO_3 medium (pH $\approx$ 10.3), these standard potentials are cathodically shifted due to reduced proton availability, though the overall thermodynamic trend remains consistent. The emergence and intensification of cathodic waves in this region confirms that Zn-doped PANI electrodes serve as photoactive catalytic interfaces, facilitating CO_2RR under illumination.

b) Comparative performance and optimization of Zn doping

Among the three systems studied, the 30% Zn-doped PANI displayed the most efficient photoelectrocatalytic performance. A steeper slope and significantly higher cathodic current in the presence of CO_2 point to reduced kinetic barriers and enhanced turnover frequency, reflecting a higher density of catalytically active sites and improved electronic conductivity.

However, 20% Zn-doped PANI also demonstrated competitive performance, achieving a balance between catalytic activity and operational potential window. It is worth noting that in related systems, excessive doping beyond optimal thresholds can lead to morphological defects, phase segregation, or diminished redox activity—though such limitations were not observed in the present case at 30% Zn doping.

This performance hierarchy underscores the beneficial role of Zn in modulating the structural and electronic properties of polyaniline, promoting CO_2 adsorption, and enhancing both photocatalytic and electrochemical activity under illumination.

3.12.3 Chronoampermetry analysis of chemically synthesized Zn-doped PANI Electrodes

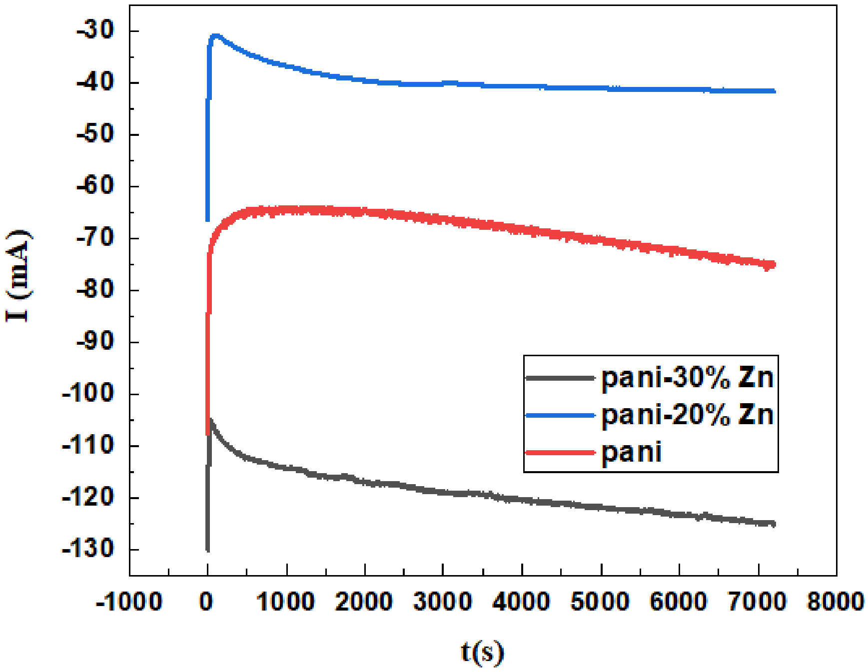

Figure 3.34: Chronoamperometric Response of PANI, PANI-20%Zn and PANI-30%Zn at -1.6 V

The chronoamperometry results shown in figure 3.34 reveal that all samples initially show a sharp cathodic current spike attributed to the charging of the electrical double layer at the electrode/electrolyte interface, followed by a decay as diffusion layers establish. At longer times, the current stabilizes, indicating pseudo-steady-state catalytic activity.

The PANI-20% Zn electrode demonstrated the poorest performance among the three samples. It showed the smallest initial current response (-30 mA) and stabilized at the lowest activity level (-41 mA). While this composition maintained stable operation over time, its consistently weak current output clearly indicates that 20% zinc loading is insufficient for effective catalytic performance.

Pure PANI displayed intermediate characteristics, beginning with a moderate initial current spike (-71 mA) that stabilized between -65 to -70 mA. However, this electrode showed gradual performance decay over extended operation, eventually reaching -75 mA. These results reveal that while undoped PANI offers reasonable initial activity, it suffers from significant long-term stability issues.

The PANI-30% Zn composite exhibits the highest initial catalytic activity, generating the strongest initial response ($\sim$-105 mA), Although as time progresses, the current for PANI-30% Zn gradually decreases, dropping from approximately -110 mA at around 500 seconds to about -125 mA at 7000 seconds. This is a significant decay compared to the PANI-20% Zn sample,indicating a trade off between high activity and long term stability.

3.13 Electrokinetic evaluation through Tafel polarization analysis

Tafel polarization, a potentiodynamic technique based on the semi-logarithmic plotting of current density versus applied potential (log I vs E), offers crucial insights into the kinetics of electron transfer at the electrode–electrolyte interface. It allows for the extraction of key electrochemical parameters such as corrosion potential (E_{corr}), corrosion current density (I_{corr}), and Tafel slopes (β_a and β_c), which collectively elucidate the charge transfer dynamics, electrocatalytic activity, and interfacial stability of the electrode material. In this study, Tafel analysis was conducted on a series of chemically and electrochemically synthesized electrodes aimed at CO_2 electroreduction under illumination.

The polarization curves of HCl-doped PANI, Cu_2O/HCl-PANI, and Zn-doped PANI interfaces in K_2CO_3 (0.5 M) are shown in Figures 3.35 to 3.39. The corresponding electrokinetic parameters derived by extrapolation of the linear regions of the Tafel plots are compiled in Table 3.5 - 3.6.

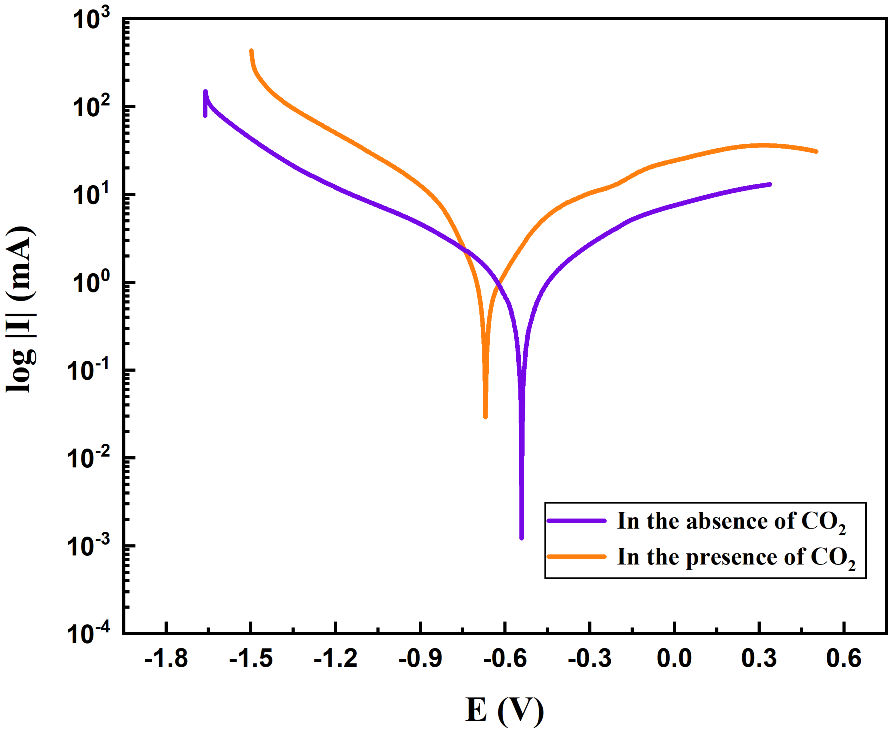

Figure 3.35: Overall Tafel polarization curves of HCl-doped PANI electrode in 0.5 M K_2CO_3 electrolyte

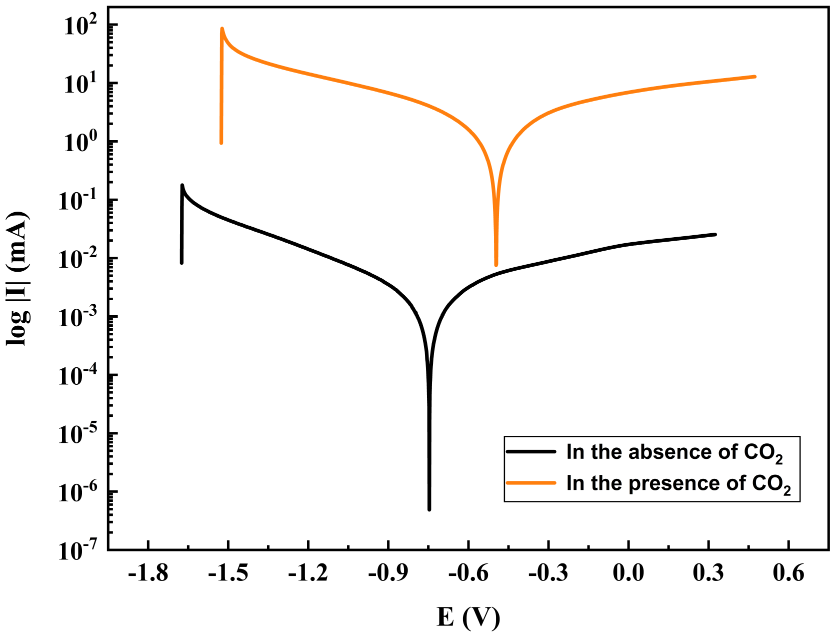

Figure 3.36: Tafel polarization behavior of Cu_2O/HCl–PANI hybrid electrode in 0.5 M K_2CO_3 electrolyte

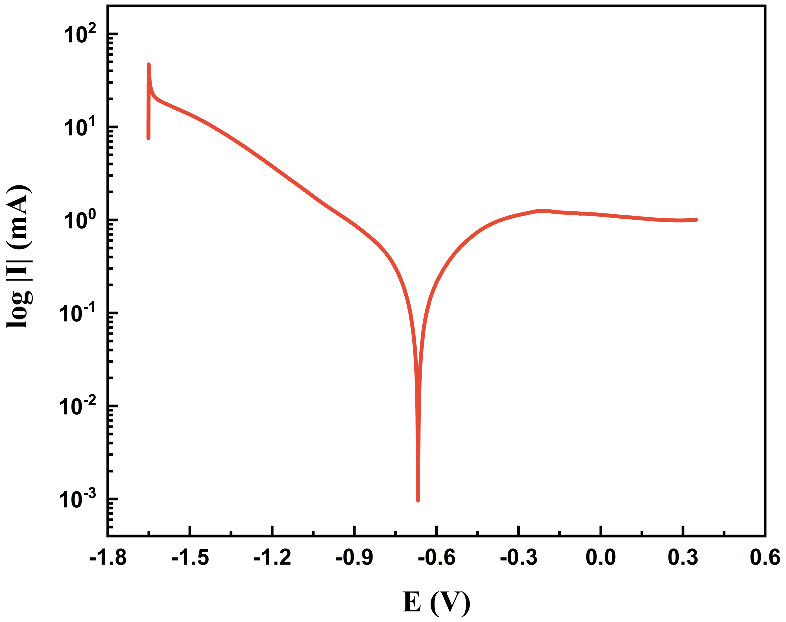

Figure 3.37: Tafel polarization response of undoped PANI (chemically synthesized) electrode in 0.5 M K_2CO_3 electrolyte

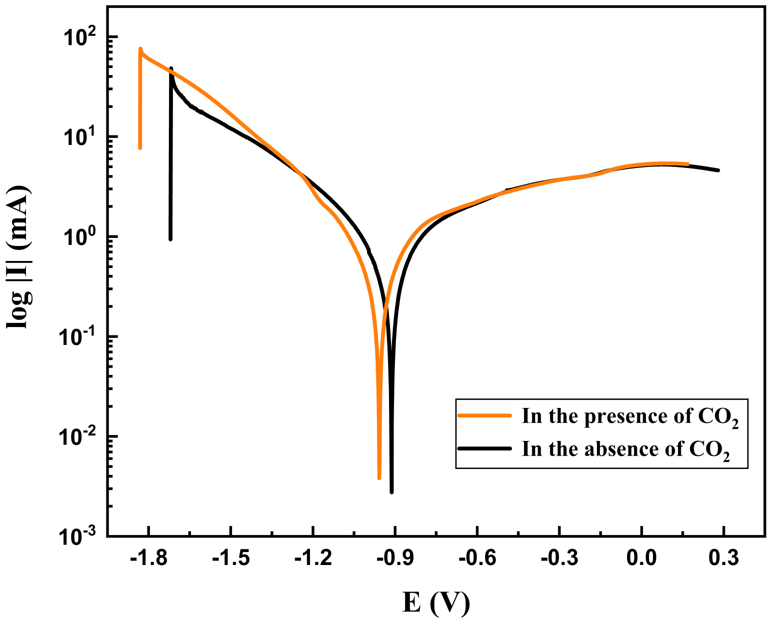

Figure 3.38: Tafel polarization curves of 30% Zn–doped PANI electrode in 0.5 M K_2CO_3 electrolyte

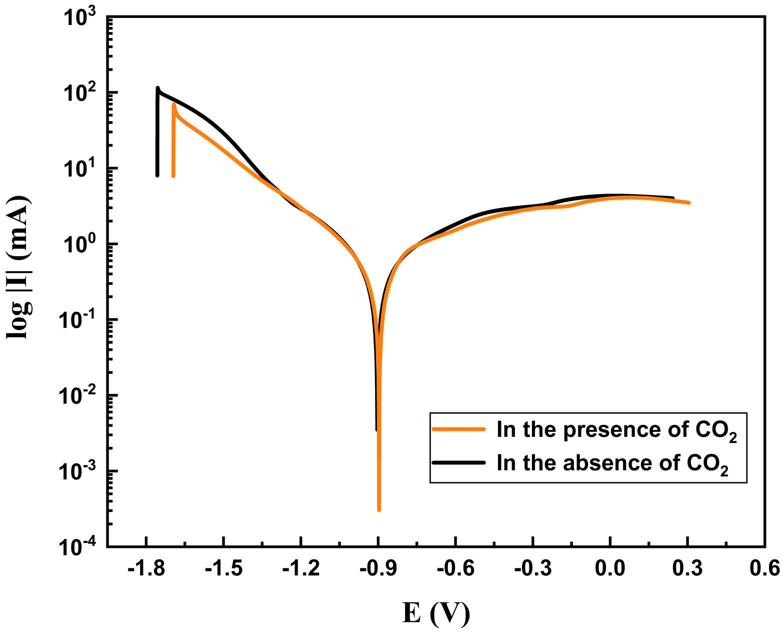

Figure 3.39: Tafel polarization curves of 20% Zn–doped PANI electrode in 0.5 M K_2CO_3 electrolyte

Table 3.5: Electrokinetic parameters of the catalysts in the absence of CO_2 (illumination, 0.5 M K_2CO_3).

Catalyst	$-E_{\text{corr}}$ (V)	j_{corr} ($\text{mA} \cdot \text{cm}^{-2}$)	R_p (Ω)	β_a ($\text{V} \cdot \text{dec}^{-1}$)	β_c ($\text{V} \cdot \text{dec}^{-1}$)
HCl–PANI	0.54089	5.4026	89.378	3.3739	1.6584
Cu_2O/HCl–PANI	0.74663	0.57915	64.879	0.16939	0.17685
Undoped PANI	–	–	–	–	–
30% Zn–PANI	0.91311	0.31166	150.49	0.22753	0.20556
20% Zn–PANI	0.9033	0.41403	193.13	0.41478	0.33108

Table 3.6: Electrokinetic parameters of the catalysts in the presence of CO_2 (illumination, 0.5 M K_2CO_3).

Catalyst	$-E_{\text{corr}}$ (V)	j_{corr} ($\text{mA} \cdot \text{cm}^{-2}$)	R_p (Ω)	β_a ($\text{V} \cdot \text{dec}^{-1}$)	β_c ($\text{V} \cdot \text{dec}^{-1}$)
HCl–PANI	0.06689	0.70824	56.589	0.20592	0.16723
Cu_2O/HCl–PANI	0.49615	0.3819	89.778	0.14803	0.16917
Undoped PANI	0.66684	0.14054	385.63	0.28861	0.21984
30% Zn–PANI	0.95736	0.1547	166.62	0.13432	0.10635
20% Zn–PANI	0.89681	0.15326	184.09	0.11577	0.14803

The symmetry observed around the corrosion potential across all log(I)–E profiles indicates a balanced electron transfer mechanism at the electrode/electrolyte interface, with well-defined anodic and cathodic branches.

Under CO_2 atmosphere and continuous light exposure, the HCl-PANI electrode exhibits a dynamically enhanced electrochemical response, marked by a relatively high corrosion current density. This behavior is attributed to the emeraldine form of PANI, known for its effective generation and transport of charge carriers (electrons and holes), thereby accelerating redox reactions. The low electronic resistance and steep Tafel slopes further reflect its favorable electronic conductivity and capacity to support redox cycling, hallmarks of conductive polymers. The extracted parameters confirm a notable photo-induced charge transfer efficiency conducive to CO_2 reduction. Importantly, the observed corrosion is interpreted not as material degradation but as an indicator of high intrinsic redox activity.

The Cu2O/HCl-PANI composite catalyst, evaluated under identical conditions, displayed clear enhancements in performance upon CO2 saturation. A shift of Ecorr to more negative values indicates increased electrochemical reactivity, while the concurrent decrease in Icorr and increase in polarization resistance (R_p) suggest improved stability—likely due to protective surface layer formation or selective CO_2 adsorption. Variations in the Tafel slopes further support the hypothesis of CO_2-influenced reaction mechanisms at the interface.

The comparison between undoped and Zn-doped PANI electrodes reveals the profound influence of Zn^{2+} incorporation on electrochemical behavior:

- **Undoped PANI** shows limited charge transfer kinetics, as indicated by low current densities and a sparse distribution of electroactive sites. Nevertheless, its relatively favorable E_{corr} indicates inherent suitability for CO2 reduction.
- **30% Zn-doped PANI** exhibits a more negative Ecorr and enhanced charge transfer kinetics, attributable to the mediating role of Zn^{2+}. The increased R_p observed in CO_2-

saturated conditions may point to surface passivation or formation of inhibitory intermediates, though the system remains the most stable and selective for CO_2 electroreduction.

- **20% Zn-doped PANI** presents similar behavior, albeit with less pronounced enhancements, indicating a positive yet suboptimal effect of the Zn^{2+} concentration on catalytic performance.

In conclusion, emeraldine-type PANI, especially when Zn-doped and illuminated under CO_2-rich conditions, demonstrates substantial promise as an electrocatalyst for photo-assisted CO_2 reduction. Tafel analysis validates that Zn doping significantly enhances the redox dynamics and charge transfer capability of PANI, with the 30% Zn formulation striking an optimal balance between conductivity, interfacial stability, and selectivity. These characteristics make it a strong candidate for scalable CO_2 photoreduction technologies. Likewise, the Cu_2O/HCl-PANI composite confirms its potential as a bifunctional catalyst, effectively interacting with CO_2 and maintaining electrochemical stability, thus supporting the formation of value-added reduction products such as methane, ethanol, or methanol.

3.14 Interfacial charge transport and photoelectrochemical impedance analysis

Electrochemical Impedance Spectroscopy (EIS) was employed to investigate the charge transfer kinetics, interfacial resistances, and catalytic activity of various PANI-based materials—namely, undoped PANI, HCl-doped PANI, PANI/Cu_2O, and Zn-doped PANI (30%)—electrodeposited on graphite substrates for the photoelectroreduction of CO_2. The analysis of Nyquist and Bode plots enabled the evaluation of composite interfacial properties, including electron transfer efficiency, adsorption of reactive intermediates, and the overall electrochemical stability of the system.

3.14.1 Electrochemical route

3.14.1.1 Nyquist

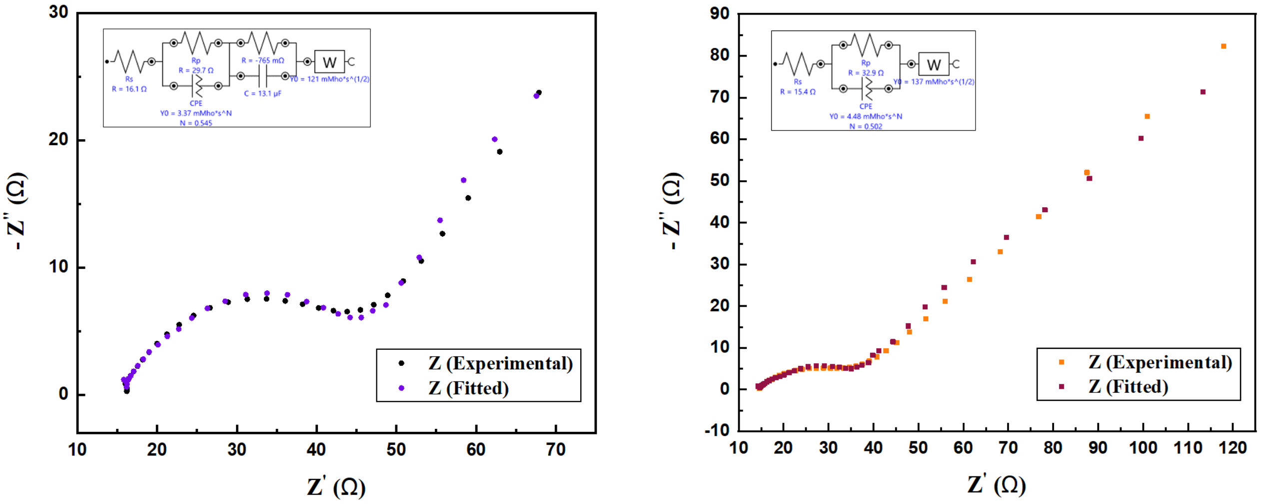

(a) In the absence of light

(b) In the presence of light

Figure 3.40: Nyquist plot ($-Z''$ vs Z') of the HCl-doped PANI/graphite electrode in 0.5 M K_2CO_3 under CO_2 atmosphere.

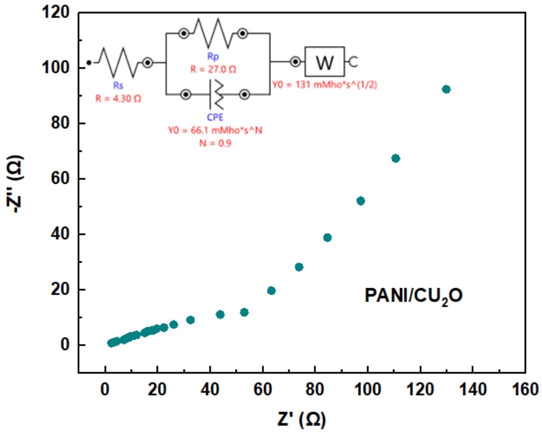

Figure 3.41: Nyquist plot of Cu_2O-Hcl/PANI

3.14.1.2 Bode

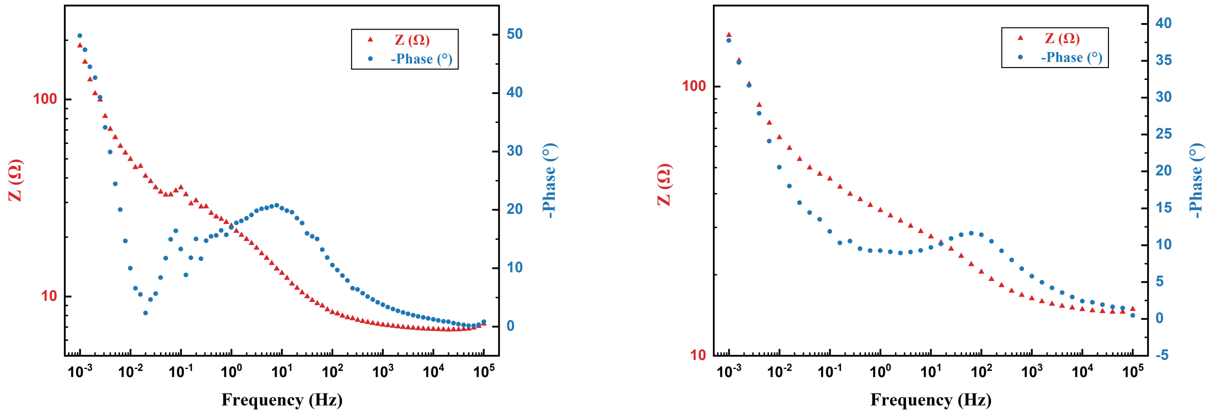

(a) In absence of light

(b) In presence of light

Figure 3.42: Bode phase and impedance magnitude plots of HCl-doped PANI in 0.5 M K_2CO_3 under CO_2 atmosphere across the frequency domain (1 mHz–100 kHz).

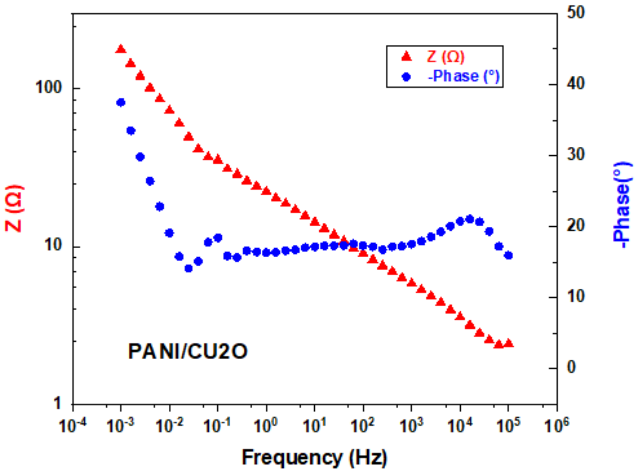

Figure 3.43: Bode plot of Cu_2O/HCl-doped PANI electrode in 0.5 M K_2CO_3 under CO_2 atmosphere across the frequency domain (1 mHz–100 kHz).

The Nyquist plots, which represent the imaginary component of impedance ($-Z''$) versus the real component (Z'), along with the corresponding Bode diagrams, of the HCl-doped PANI and Cu_2O/HCl-doped PANI are shown in the figures above. Equivalent electrical circuit models in nyquist graphs were fitted to the data in order to extract electrokinetic parameters relevant to interfacial performance.

For instance, The fitted circuit topology for 3.40a corresponds to eq. 3.8:

$$Z(\omega) = R_s + (\mathrm{CPE} \parallel R_p) + (C_1 \parallel R_1) + W_1 \tag{3.8}$$

Where:

- R_s: Solution resistance (electrolyte + contact + substrate),
- R_p (R_{ct}): Charge transfer resistance at the polymer/electrolyte interface,
- CPE (Q): Constant phase element modeling non-ideal double-layer behavior due to surface roughness or heterogeneity,
- R_1–C_1: Interfacial polymer resistance/capacitance pair,
- W_1: Warburg impedance element, capturing ion diffusion limitations at low frequencies.

Nyquist plot analysis in Fig. 3.40 revealed distinct impedance signatures for the HCl-doped PANI under illumination, which exhibited a reduced series resistance (R_s) and improved capacitive and diffusive behavior. This response is attributed to enhanced separation and mobility of photogenerated charge carriers, promoting efficient interfacial electron transfer and favorable ion diffusion—key criteria for effective photoelectrocatalysis of CO_2.

The bode plots in fig. 3.42 reveal the frequency-dependent evolution of both the modulus of the impedance ($|Z|$) and the phase angle (θ), offering crucial insights into the resistive, capacitive, and diffusive dynamics of the system.

- At **high frequencies** ($f > 1\,\mathrm{kHz}$), the phase angle approaches 0°, and the impedance modulus $|Z|$ plateaus near the series resistance ($R_s \approx 16.1\,\Omega$ in the dark; $14.4\,\Omega$ under light), confirming ohmic control dominated by the electrolyte and doped PANI.
- In the **mid-frequency range** ($100\,\mathrm{Hz}$ to $1\,\mathrm{kHz}$), the phase angle reaches higher values under illumination, which indicates enhanced capacitive behavior. This is consistent with a more homogeneous and responsive double-layer capacitance, likely due to increased photogenerated charge carriers improving interfacial polarization.
- At **low frequencies** ($f < 10\,\mathrm{Hz}$), a rise in $|Z|$ and a drop in phase angle reflect diffusion-limited ion transport. The smaller slope and higher phase angle under illumination suggest improved ionic mobility or better electrolyte penetration into the PANI matrix, potentially enabled by photo-induced structural softening.

For the Cu_2O/HCl-doped PANI electrode, the nyquist plot 3.41 shows a significantly smaller semicircle compared to pure PANI, followed by a more pronounced and steeper Warburg diffusion tail at lower frequencies. The overall impedance is much lower than that of pure PANI. The extracted parameters from the equivalent circuit reveal further details:

- **Solution Resistance (Rs)**: Approximately 4.3Ω.
- **Charge Transfer Resistance (Rct)**: Around 27Ω. This is a drastic reduction compared to pure PANI.
- **Warburg Impedance**: A clear and relatively steep linear region at low frequencies, indicating diffusion controlled processes are significant.

The significant decrease in Rct indicates that the incorporation of Cu_2O has dramatically improved the charge transfer kinetics at the electrode surface. This suggests better electrical conductivity and more active sites for electrochemical reactions. The more prominent Warburg tail implies that mass transport (CO_2 diffusion to the electrode surface) becomes a more limiting factor at lower frequencies, which is a good sign as it means charge transfer is no longer the primary obstacle.

For bode plot in fig. 3.43 The PANI/Cu_2O electrode demonstrates excellent charge transport characteristics, as evidenced by its impedance modulus decreasing from $\sim$ 200Ω at low frequencies (10^{-3} Hz) to below 5Ω at high frequencies (10^5 Hz). This low impedance correlates well with the small solution resistance ($R_S \approx 4.3\Omega$) observed in Nyquist plots, confirming the composite's highly conductive nature.

The phase angle profile provides further mechanistic insights, showing three distinct features:

- A low frequency peak ($10^{-1}Hz$, $\sim 20°$) indicating mixed faradaic and mass transport control of CO_2 reduction processes, consistent with the Nyquist plot's Warburg tail;
- A prominent high-frequency peak ($\sim 10^4$ Hz) reflecting fast charge transfer kinetics at the PANI/Cu_2O interface, supported by the significantly reduced charge transfer resistance.
- A characteristic mid frequency shoulder ($\sim 10^2$ Hz) attributable to PANI's redox pseudocapacitance, which facilitates electron injection during CO_2 activation.

These features demonstrate Cu_2O's combined role in enhancing both charge transport and catalytic activity, lowering kinetic barriers while maintaining efficient mass transport and redox mediation. The excellent agreement between Bode magnitude, phase angle, and Nyquist plot features provides robust evidence for the composite's superior electrochemical performance in CO_2 reduction applications.

3.14.2 Chemical route

3.14.2.1 NYQUIST

Figure 3.44 represents the nyquist plots of three electrodes deposited on graphite: pure PANI and PANI-30%Zn nanocomposite.

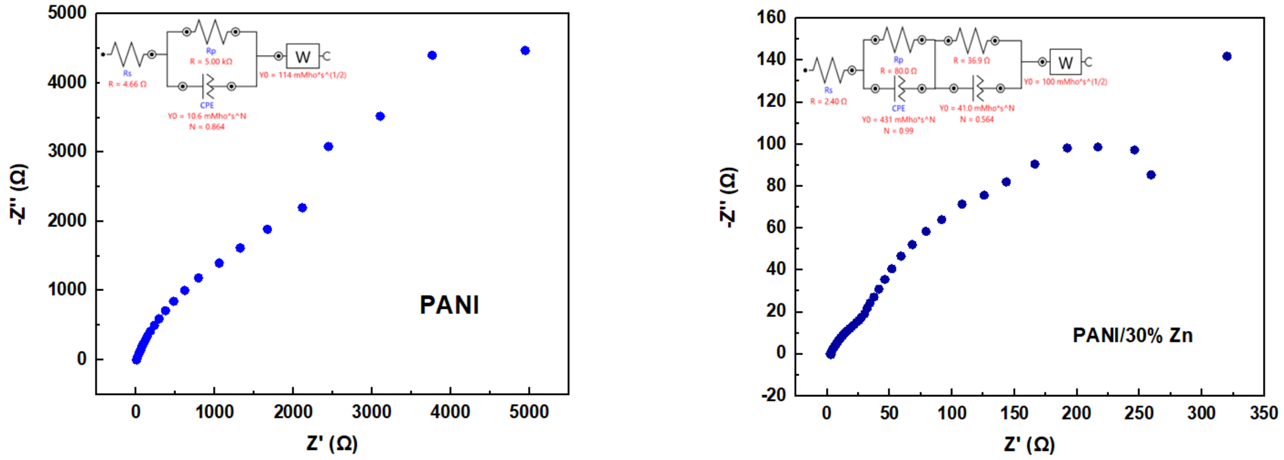

Figure 3.44: Nyquist plots for pure PANIand PANI-30%Zn nanocomposite.

The Nyquist plot for the pure PANI electrode exhibits a very large, depressed semicircle in the high to mid frequency region, followed by a relatively short, inclined line at lower frequencies. The semicircle is not fully closed within the displayed range, indicating a very high impedance.From the equivalent circuit of this system, the electrochemical parameters can be derived:

- **Solution Resistance (Rs)**: Approximately 4.66 Ω.
- **Charge Transfer Resistance (Rct)**: Very high, approximately 5000Ω, given the large diameter of the semicircle. This indicates very slow charge transfer kinetics at the PANI electrode surface.
- **Warburg Impedance**: The low frequency tail is present but not very steep, suggesting some diffusion limitation, but the dominant process is the high charge transfer resistance.

The very high Rct for pure PANI suggests that it has poor electrical conductivity and very slow electron transfer kinetics for electrochemical reactions. This would severely limit its efficiency for CO_2 conversion, as the charge transfer step is an obstacle. A high Rct means that a large overpotential would be required to drive the reaction, leading to low current densities and poor energy efficiency.

In the case of PANI-30% Zn electrode, The plot reveals dramatically improved kinetics compared to pure PANI, while maintaining excellent solution conductivity. Featuring two distinct charge transfer processes through overlapping semicircles, suggesting parallel conduction pathways via both PANI/Zn interfaces and modified polymer regions. followed by a distinct Warburg tail. Key parameters from equivalent circuit fitting quantify these improvements:

- **Solution Resistance (Rs)**: Approximately 2.4 Ω.
- **Charge Transfer Resistance (Rct)**: a combined value of 116.9 Ω. (80 Ω from the first semi circle and 36.9 Ω from the second),still significantly lower than pure PANI but higher than PANI/Cu_2O.
- **Warburg Impedance**: A prominent linear region, indicates the system has transitioned to diffusion limited behavior, confirming that charge transfer is no longer the primary obstacle.

In conclusion, both nanocomposites (PANI/Cu_2O/HCl and PANI/30%Zn) show significantly improved electrochemical properties compared to pure PANI, making them more suitable for electrochemical CO_2 conversion. The PANI/Cu_2O/HCl appears to have slightly better charge transfer kinetics and mass transport properties based on these Nyquist plots. These EIS results provide strong evidence for the enhanced catalytic activity and conductivity of the modified PANI electrodes, which are crucial for driving the CO_2 reduction reaction efficiently.

3.14.2.2 Bode

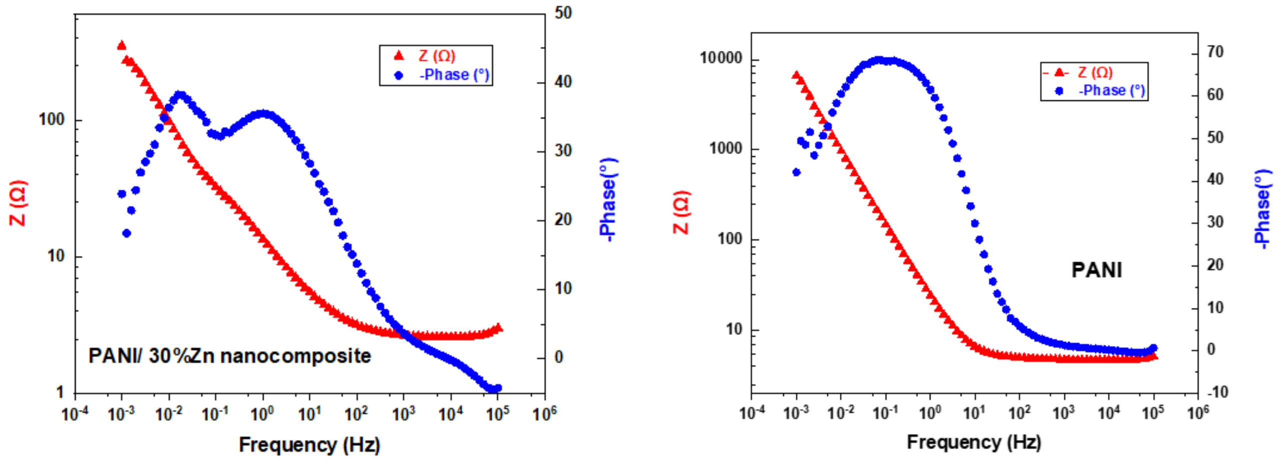

Figure 3.45: Bode plots for PANI/Cu_2O,PANI,and PANI/30%Zn nanocomposite.

Figure 3.45 represents the Bode plots of three graphite supported electrodes: PANI and PANI-30%Zn nanocomposite. These frequency dependent impedance spectra provide insight into the electrochemical characteristics relevant to CO_2 conversion processes, including interfacial charge transfer, capacitive storage, and ionic diffusion within the electrode structure

The pure PANI electrode exhibits significantly limited charge transfer characteristics, as demonstrated by its high impedance modulus ($>10^3$ Ω at low frequencies, approaching 10^4 Ω at $10^{-3} Hz$). This substantial resistance persists across the entire frequency range, with even the high frequency impedance remaining relatively elevated ($5 - 10\Omega$), reflecting both solution resistance and poor intrinsic conductivity. These observations align perfectly with the Nyquist plot's massive semicircle, which revealed an exceptionally high charge transfer resistance.

The phase angle profile shows a dominant capacitive peak reaching 70° (centered around 10^{-1} Hz), confirming the material's strong pseudocapacitive behavior characteristic of electroactive polymers. However, the absence of any secondary peak at low frequencies clearly indicates inadequate faradaic activity, a critical limitation for CO_2 conversion applications. This electrochemical profile reveals two fundamental constraints:

- Severely hindered electron/ion transport due to the polymer's high charge transfer resistance.
- The lack of metal centers to stabilize key CO_2 reduction intermediates.

While the graphite substrate provides some conductive pathways, it cannot overcome these intrinsic limitations. The consistent evidence from both Bode and Nyquist analyses confirms that pure PANI, despite its redox capacitive properties, suffers from kinetic obstacles that fundamentally restrict its catalytic performance for electrochemical CO_2 conversion.

The PANI/30%Zn electrode demonstrates markedly improved conductivity compared to pure PANI, evidenced by its low frequency impedance modulus of $\sim 200\ \Omega$ (at 10^{-3} Hz). This enhanced performance is consistent across the frequency spectrum, with high frequency impedance stabilizing at $2-3\ \Omega$, reflecting both low solution resistance (R_S) and efficient charge transfer. These Bode plot observations correlate perfectly with Nyquist results showing a dramatically reduced semicircle diameter compared to pure pani. The phase angle profile reveals two key features:

- a primary pseudocapacitive peak at $\sim 10^{-2}$ to 10^{-1} Hz ($\sim 40°$), less pronounced than pure PANI's 70° peak, indicating faster charge transfer kinetics
- a secondary pseudocapacitive peak at $\sim 10^{0}$ to 10^{1} Hz (35° to 40°),attributed to the charge transfer process across the electrode/electrolyte interface and the capacitive behavior of the electrode
- a characteristic high-frequency decline as capacitive effects give way to resistive behavior

While the Nyquist plot confirms some persistent mass transport limitations, the dominant improvement lies in charge transfer efficiency. This enhancement stems from Zn's dual role: improving bulk conductivity while creating active sites for CO_2 interaction. The metal centers facilitate both electron transfer through the composite and stabilization of reaction intermediates, while the PANI matrix provides proton conduction pathways and the graphite substrate ensures electrical connectivity. Though not as conductive as PANI/Cu_2O, this composite represents a significant advancement over pure PANI for CO_2 electroreduction applications.

3.15 Comparative evaluation of photoelectrocatalytic parameters

To conclude the electrochemical investigation, a comparative analysis of the three key descriptors—**Tafel slope**, **charge transfer resistance (R_{ct})**, and **steady-state photocurrent (I_{CA}) at** (-1.6 V)—is presented in Table 3.7. This synthesis enables a critical evaluation of the photoelectrocatalytic efficiency across the developed electrodes under CO_2-saturated illumination in 0.5 M K_2CO_3.

Table 3.7: Comparison of Tafel slopes, charge transfer resistances, and chronoamperometric current plateaus ($V = -1.6$ V) for various catalysts under illumination in CO_2-saturated* 0.5 M K_2CO_3.

Catalyst	**Tafel slope** ($\mathrm{V \cdot dec^{-1}}$)	$\boldsymbol{R_{ct}}$ **(Ω)**	$\boldsymbol{I_{CA}}$ **@ -1.6 V (mA)**
HCl–PANI	0.16723	32.9	-105
Cu_2O/HCl–PANI	0.16917	27	-70
Undoped PANI (chem.)	0.21984	5×10^3	-68
20% Zn–PANI	0.14803	–	-43
30% Zn–PANI	0.10635	116.9	-117

*Introduced via bubbling, and in supporting carbonate electrolyte.

Based on **standard performance criteria** for CO_2 electroreduction:

- The **Cu_2O/HCl–PANI** electrode demonstrates the most favorable interfacial kinetics, with an R_{ct} of $27\,\Omega$, classifying it as *good*, and far superior to the *undoped PANI*, which exhibits a high resistance of $\sim 5\,\mathrm{k\Omega}$—well beyond the acceptable threshold (*low performance*). The incorporation of Cu_2O is thus shown to significantly enhance charge transfer by forming efficient heterojunction interfaces.
- The **30% Zn–PANI** nanocomposite achieves the lowest Tafel slope ($0.10635\,\mathrm{V \cdot dec^{-1}}$), which lies within the *good* kinetic regime, and exhibits the highest photocurrent ($|I_{CA}| = 117\,\mathrm{mA}$), indicating efficient catalytic turnover and high electron availability at the reaction interface. Despite a moderate R_{ct} ($\sim 117\,\Omega$), its superior current output suggests effective active site accessibility and redox performance under illumination.
- The **20% Zn–PANI** sample, although not accompanied by R_{ct} data, shows decent Tafel kinetics ($0.14803\,\mathrm{V \cdot dec^{-1}}$) and moderate I_{CA} ($-43\,\mathrm{mA}$), yet underperforms compared to its 30% counterpart, reinforcing the advantage of increased Zn incorporation.
- Both **HCl–PANI** and **undoped PANI** exhibit higher Tafel slopes (> 0.16 and $> 0.21\,\mathrm{V \cdot dec^{-1}}$ respectively), and reduced I_{CA} values (-105 and $-68\,\mathrm{mA}$), correlating with limited charge transfer and catalytic efficiency.

These results clearly establish that:

1. Cu_2O integration is optimal for minimizing interfacial resistance;
2. 30% Zn doping offers the best balance between kinetic activation and product-forming current.

The combination of these findings confirms the synergistic enhancement brought by inorganic phase incorporation into the PANI matrix. This strategy significantly surpasses the limitations of undoped PANI in terms of conductivity, charge mobility, and catalytic site activity—making both **Cu_2O/HCl–PANI** and **30% Zn–PANI** promising candidates for selective and efficient CO_2 photoelectroreduction under mild, sunlight-driven conditions.

These findings collectively confirm that doping polyaniline with Cu_2O or Zn markedly enhances its interfacial electrochemical characteristics and efficiency in CO_2 photoelectroreduction, in contrast to undoped PANI, which is constrained by poor conductivity and the absence of effective catalytic centers.

3.16 Conclusion

The results obtained from this study clearly demonstrate the potential of polyaniline-based photoelectrodes—prepared either as thin films or paste-type formulations—for the electrochemical reduction of CO_2 to methanol and other unidentified products in 0.5 M K_2CO_3 media. Notably, the integration of Cu_2O nanoparticles within the polyaniline matrix significantly improved electrode performance, particularly in terms of photocurrent generation and photoelectrocatalytic CO_2 reduction efficiency. The modified photocatalyst achieved a CO_2-to-methanol conversion efficiency of 17.162 %, outperforming the 14.608 % yield recorded for HCl-doped PANI alone. This improvement is primarily attributed to the homogeneous dispersion of Cu_2O within the conductive PANI framework.

Moreover, Zn-doping of PANI has emerged as a promising strategy for CO_2 valorization. Zinc offers favorable catalytic properties, including the ability to adsorb CO_2, facilitate its activation under illumination, and promote efficient electron transfer. Zn also contributes to improved conductivity and catalytic behavior of the PANI matrix by generating active sites capable of reducing CO_2 into products such as carbon monoxide (CO) or formic acid (HCOOH). These findings underscore the role of compositional and structural engineering in optimizing the performance of PANI-based photoelectrodes for sustainable carbon dioxide conversion.

General conclusion

The transition to a sustainable energy future demands innovative solutions that not only reduce carbon emissions but also transform CO_2 into valuable resources. Among emerging technologies, photoelectrocatalytic CO_2 reduction stands out as a promising approach that combines renewable solar energy with advanced catalytic materials to produce fuels and chemicals. Our research contributes to this field by developing and optimizing novel hybrid photoelectrodes for efficient CO_2 conversion.

This study focused on 4 key electrode systems: pure polyaniline (PANI), HCl-doped polyaniline , Cu_2O/HCl-doped PANI , and Zn-doped PANI composites, all deposited on graphite electrodes. Each system was carefully characterized and evaluated for its photoelectrocatalytic performance in CO_2 reduction. The work was conducted at the Research Center in Semiconductor Technology for Energetics (CRTSE), with particular attention to material properties, catalytic activity, and product selectivity.

Key findings from our comprehensive investigation include:

- **Material and morphological Characterization:**
  - HCl-PANI exhibited a porous, nanofibrous structure ideal for catalytic surface reactions
  - Cu_2O deposition created uniform nanoparticle coatings that enhanced light absorption
  - Zn doping introduced new crystalline phases while maintaining PANI's conductive network
  - XPS analysis revealed that electrochemically synthesized PANI-HCl exhibits enhanced surface oxidation and nitrogen protonation, creating more active sites for CO_2 adsorption and reduction compared to chemically synthesized PANI.
- **Electrochemical Performance :**
  - All electrodes exhibited increased cathodic currents under CO_2 saturation
  - Cu_2O modification significantly reduced charge transfer resistance
- **Photocatalytic Activity :**
  - UV-Vis spectroscopy confirmed visible-light responsiveness (1.5-2.35 eV bandgaps) for all materials
  - enhanced catalytic activity under CO_2-saturated conditions, particularly for PANI-30%-zn modified electrodes.
- **Methanol Production:** Gas chromatography (GC) analysis identified methanol as the primary CO_2 reduction product, with a Faradaic efficiency of up to 17.62% for Cu_2O/PANI electrodes, highlighting their selectivity for value-added chemicals.

Both modification strategies (Cu_2O deposition and Zn doping) proved effective for improving different aspects of photoelectrocatalytic performance.

Perspectives for Future Research: To advance this work, systematic optimization of dopant concentrations (higher Cu_2O loading or ZnO substitution) should be pursued to enhance charge transfer and catalytic stability. A critical next step involves comprehensive product analysis using HPLC and gas chromatography to quantify all CO_2 reduction products (formate, methanol, C^{2+} compounds) and establish precise Faradaic efficiencies. Coupled with in-situ spectroelectrochemical characterization (Raman, FTIR) and post-reaction surface analysis (XPS, TEM), these techniques would unravel reaction pathways and degradation mechanisms. Additionally, integrating these materials into advanced reactor designs, such as membrane electrode assemblies (MEAs), could accelerate their transition to industrial applications.

Bibliography

[1] Wangkheimayum Marjit Singh, Teera Baine, Shotaro Kudo, Shiliang Tian, Xuan Anh N. Ma, Hongyu Zhou, Nathan J. DeYonker, Truc Chi Pham, John C. Bollinger, Daniel L. Baker, Bing Yan, Charles E. Webster, and Xuan Zhao. Electrocatalytic and photocatalytic hydrogen production in aqueous solution by a molecular cobalt complex. *Angewandte Chemie International Edition*, 51(24):5941–5944, 2012.

[2] United States Environmental Protection Agency (USEPA). Global greenhouse gas emissions data. https://www.epa.gov/ghgemissions/global-greenhouse-gas-emissions-data, 2022. Accessed on 28 July 2022.

[3] Hannah Ritchie, Max Roser, and Pablo Rosado. Co and greenhouse gas emissions. *Our World in Data*, 2020. https://ourworldindata.org/co2-and-greenhouse-gas-emissions.

[4] National Oceanic & Atmospheric Administration (NOAA). Global monitoring laboratory. trends in atmospheric carbon dioxide. https://gml.noaa.gov/ccgg/trends/gl_trend.html, 2023. Accessed on 16 January 2023.

[5] Our World in Data. Why do greenhouse gas emissions matter? https://ourworldindata.org/co2-and-other-greenhouse-gas-emissions, 2022. Accessed on 28 July 2022.

[6] J. Podder, B.R. Patra, F. Pattnaik, S. Nanda, and A.K. Dalai. A review of carbon capture and valorization technologies. *Energies*, 16(6):2589, 2023.

[7] Peng Chen, Yuxin Zhang, Ying Zhou, and Fan Dong. Photoelectrocatalytic carbon dioxide reduction: Fundamental, advances and challenges. *Nano Materials Science*, 3, 06 2021.

[8] C. Zuo, Q. Su, and X. Yan. Research progress of co-catalysts in photocatalytic co2 reduction: A review of developments, opportunities, and directions. *Processes*, 11(3):867, 2023.

[9] K. Kočí, K. Matějů, L. Obalová, S. Krejčíková, Z. Lacný, D. Plachá, L. Čapek, A. Hospodková, and O. Šolcová. Effect of silver doping on the tio for photocatalytic reduction of co. *Applied Catalysis B: Environmental*, 96:239–244, 2013.

[10] Roberta Farina, Silvia Scalese, Domenico Corso, Giuseppe Emanuele Capuano, Giuseppe Andrea Screpis, Maria Anna Coniglio, Guglielmo Guido Condorelli, and Sebania Libertino. Chronoamperometric ammonium ion detection in water via conductive polymers and gold nanoparticles. *Molecules*, 29(13), 2024.

[11] Mohmmad Khalid, Ana Maria Borges Honorato, and Hamilton Varela. Polyaniline: Synthesis methods, doping and conduction mechanism. In *Conducting Polymers*, chapter 2. IntechOpen, London, UK, 2018.

[12] Warren Athol Thompson, Eva Sanchez Fernandez, and M. Mercedes Maroto-Valer. Review and analysis of co2 photoreduction kinetics. *ACS Sustainable Chemistry & Engineering*, 8(12):4677–4692, 2020.

[13] Xiaojie She, Yifei Wang, Hui Xu, Shik Chi Edman Tsang, and Shu Ping Lau. Challenges and opportunities in electrocatalytic co_2 reduction to chemicals and fuels. *Angewandte Chemie International Edition*, 61:e202211396, 2022.

[14] Wenchuan Lai, Yan Qiao, Yanan Wang, and Hongwen Huang. Stability issues in electrochemical co2 reduction: Recent advances in fundamental understanding and design strategies. *Advanced Materials*, 35(51):2306288, 2023.

[15] Diane Turner. Gas chromatography – how a gas chromatography machine works, how to read a chromatograph and gcxgc, 2024. Last updated: March 12, 2024.

[16] P. Friedlingstein, M. O'Sullivan, M. Jones, and et al. Global carbon budget 2023. *Earth System Science Data*, 2023.

[17] Intergovernmental Panel on Climate Change (IPCC). Climate change 2023: Synthesis report, 2023. IPCC.

[18] World Meteorological Organization (WMO). Wmo provisional state of the global climate 2023, 2023. Provisional Report.

[19] Yashly Yesudas K, Gopal Buvaneswari, and Annamalai Senthil Kumar. Polyaniline-based synergetic electrocatalysts for co2 reduction reaction: A review. *Electrochemical Science Advances*, 5(1):e2400007, 2024.

[20] S. S. H. F. K. Ledley. Climate change and greenhouse gases. *American Geophysical Union (AGU)*, 1999.

[21] N. Harris, D. Gibbs, A. Baccini, and et al. Global maps of twenty-first century forest carbon fluxes. *Nature Climate Change*, 2021.

[22] World Meteorological Organization (WMO). Wmo greenhouse gas bulletin: The state of greenhouse gases in the atmosphere. https://public.wmo.int, 2023. World Meteorological Organization, Geneva.

[23] G. Hurtt, B. Poulter, et al. Nasa arctic-boreal vulnerability experiment (above) synthesis studies. https://carbon.nasa.gov/, 2021–2023. NASA Carbon Monitoring System.

[24] NOAA Global Monitoring Laboratory. Annual greenhouse gas index (aggi). https://gml.noaa.gov/aggi/, 2023.

[25] NASA Ozone and Air Quality Team. Nasa ozone watch: Latest status of the ozone layer. https://ozonewatch.gsfc.nasa.gov/, 2024. NASA Goddard Space Flight Center.

[26] UNEP/WMO Scientific Assessment Panel. Scientific assessment of ozone depletion: 2022, 2022. World Meteorological Organization.

[27] World Meteorological Organization (WMO). State of the global climate 2023, 2023. WMO.

[28] Kaykobad Md. Rezaul Karim, Mostafa Tarek, Shaheen M. Sarkar, Rabah Mouras, Huei Ruey Ong, Hamidah Abdullah, Chin Kui Cheng, and Md. Maksudur Rahman Khan. Photoelectrocatalytic reduction of co_2 to methanol over $cufe_2o_4$@pani photocathode. *Journal of CO_2 Utilization*, 60:101990, 2022.

[29] Yashly Yesudas and Gopal Buvaneswari. Polyaniline-based synergetic electrocatalysts for co_2 reduction reaction: A review. *Chemosphere*, 348:139358, 2023.

[30] Z. Tan. *Air Pollution and Greenhouse Gases: From Basic Concepts to Engineering Applications for Air Emission Control.* Springer, 2016.

[31] US EPA. Greenhouse gas inventory reports: Inventory of u.s. greenhouse gas emissions and sinks: 1990–2006. #430-R-08-005. Available at: http://www.epa.gov/climatechange/emissions/downloads/08_CR.pdf, 2008. Accessed July 2008.

[32] United Nations. World population division website. Available at: http://www.un.org/en/development/desa/population/publications/pdf/trends/WPP2012_Wallchart.pdf, 2012. Accessed January 2014.

[33] Peng Chen, Yu Zhang, Yifei Zhang, and Feng Dai. Photoelectrocatalytic carbon dioxide reduction: Fundamental, advances and challenges. *Nano Materials Science*, 2021.

[34] NOAA Climate.gov. Climate change: Atmospheric carbon dioxide, n.d. Accessed July 2025.

[35] Messer Group. Ccus and net zero: The importance of carbon capture to achieve our climate goals, 2024. Accessed July 2025.

[36] Wenhao Zhang, Abdul Rahman Mohamed, and Wee-Jun Ong. Z-scheme photocatalytic systems for carbon dioxide reduction: Where are we now? *Advanced Science*, 8(7):2004029, 2021.

[37] Yuchao Wang, Yi Liu, Wei Liu, Jiao Wu, Qian Li, Qingguo Feng, Zhiyan Chen, Xiang Xiong, Dingsheng Wang, and Yongpeng Lei. Regulating the coordination structure of metal single atoms for efficient electrocatalytic co_2 reduction, 2020.

[38] Xingchen Jiao, Zongwei Chen, Xiaodong Li, Yongfu Sun, Shan Gao, Wensheng Yan, Chengming Wang, Qun Zhang, Yue Lin, Yi Luo, and Yi Xie. Defect-mediated electron–hole separation in one-unit-cell $znin_2s_4$ layers for boosted solar-driven co_2 reduction. *Journal of the American Chemical Society*, 139(22):7586–7594, 2017.

[39] Vignesh Kumaravel, John Bartlett, and Suresh C. Pillai. Photoelectrochemical conversion of carbon dioxide (co_2) into fuels and value-added products. *ACS Energy Letters*, 5(2), 2020.

[40] Y.Y. Birdja, E. Pérez-Gallent, M.C. Figueiredo, F. Scholten, E.A. Hernandez-Pagan, and M.T.M. Koper. Advances and challenges in understanding the electrocatalytic conversion of carbon dioxide to fuels. *Nature Energy*, 4:732–745, 2019.

[41] G. Centi and S. Perathoner. Catalysis: Role and challenges for a sustainable energy. *Topics in Catalysis*, 52(7–8):948–961, 2009.

[42] M. Halmann. Photoelectrochemical reduction of aqueous carbon dioxide on p-type gallium phosphide in liquid junction solar cells. *Nature*, 275(5676):115–116, 1978.

[43] Thomas J. LaTempa, Sanju Rani, Ningzhong Bao, and Craig A. Grimes. Generation of fuel from co_2 saturated liquids using a p-si nanowire ∥ n-tio_2 nanotube array photoelectrochemical cell. *Nanoscale*, 4(7):2245–2250, 2012.

[44] Mohamed A. Hassaan, Mohamed El-Nahhal, et al. Principles of photocatalysts and their different applications: A review. *National Library of Medicine*, 2023.

[45] Bhupendra Kumar, Mark Llorente, Jesse Froehlich, Tram Dang, Aaron Sathrum, and Clifford P. Kubiak. Photochemical and photoelectrochemical reduction of co. *Annual Review of Physical Chemistry*, 63:541–569, 2012.

[46] Elin Svensson, Karin Eriksson, Mathilde Luneau, and Stefan Heyne. Electrochemical reduction of co_2: What potential is there for sustainable production of chemicals through direct electrochemical conversion of carbon dioxide? Final Report Version Final, Climate Leading Process Industry (Klimatledande Processindustri), 2024.

[47] Blanca Belsa, Lu Xia, Viktoria Golovanova, Bárbara Polesso, Adrián Pinilla-Sánchez, Lara San Martín, Jiaye Ye, Cao-Thang Dinh, and F. Pelayo García de Arquer. Materials challenges on the path to gigatonne CO electrolysis. *Nature Reviews Materials*, 9(8):535–549, August 2024.

[48] Asma Al Harthi, Mohammed Al Abri, Hussein A. Younus, and Rashid Al Hajri. Criteria and cutting-edge catalysts for co electrochemical reduction at the industrial scale. *Journal of CO2 Utilization*, 83:102819, 2024.

[49] Vignesh Kumaravel, John Bartlett, and Suresh C. Pillai. Photoelectrochemical conversion of carbon dioxide (co2) into fuels and value-added products. *ACS Energy Letters*, 5(2):486–519, 2020.

[50] Cheng Zuo and Xiao Yu. Research progress of co-catalysts in photocatalytic co2 reduction: A review of developments, opportunities, and directions. *College of Chemical Engineering and Environmental Engineering, Weifang University*, 2023.

[51] Anas Boussaa and Sabiha. *Traitement de la silice destinée à l'élaboration du silicium solaire : enrichissement et caractérisation.* Doctoral dissertation, Université des Sciences et de la Technologie Houari Boumédiène (USTHB), Alger, Algeria, 2018.

[52] T. S. Ledley, E. T. Sundquist, S. E. Schwartz, D. K. Hall, J. D. Fellows, and T. L. Killeen. Climate change and greenhouse gases. *Eos, Transactions American Geophysical Union*, 80(39):453–458, 1999.

[53] György Inzelt. *Conducting Polymers: A New Era in Electrochemistry.* Monographs in Electrochemistry. Springer-Verlag Berlin Heidelberg, Berlin, Heidelberg, 2 edition, 2012.

[54] Dorottya Hursán, Attila Kormányos, Krishnan Rajeshwar, and Csaba Janáky. Polyaniline films photoelectrochemically reduce co2 to alcohols. *Chem. Commun.*, 52:8858–8861, 2016.

[55] Ahlem Hadjadj and Zahra Mohamed Ykhlef. Synthèse et caractérisation des composites par polymérisation in-situ de l'aniline chargé de diatomite. Mémoire de master, Centre Universitaire Belhadj Bouchaib d'Aïn Témouchent (CUBBA), Aïn Témouchent, Algérie, September 2020. Consulté pour la section sur la polyaniline (pp. 23–30).

[56] Mahnoush Beygisangchin, Suraya Abdul Rashid, Suhaidi Shafie, Amir Reza Sadrolhosseini, and Hong Ngee Lim. Preparations, properties, and applications of polyaniline and polyaniline thin films—a review. *Polymers*, 13(12), 2021.

[57] A. Tab, C. Belabed, A. Mahieddine, et al. 1t/2h-mos2@zn-ni mof composite: A novel catalyst for efficient hydrogen production and antimicrobial activity. *Journal of Water Process Engineering*, 75:108047, 2025.

[58] M. C. O. Monteiro, M. F. Philips, K. J. P. Schouten, et al. Efficiency and selectivity of co_2 reduction to co on gold gas diffusion electrodes in acidic media. *Nature Communications*, 12:4943, 2021.

[59] E.T. Kang, K.G. Neoh, and K.L. Tan. Polyaniline: A polymer with many interesting intrinsic redox states. *Progress in Polymer Science*, 23:277–324, 1998.

[60] Wenchuan Lai, Yan Qiao, Yanan Wang, and Hongwen Huang. Stability issues in electrochemical co_2 reduction: Recent advances in fundamental understanding and design strategies. *Advanced Materials*, 35:24, 10 2023.

[61] Z. Haihua, P. Shunjin, and P. Weijie. Electrochemical properties of pani as single electrode of electrochemical capacitors in acid electrolytes. *The Scientific World Journal*, 2013:940153, 2013.

[62] Tatyana Nychyporuk. *Nouvelles morphologies du silicium nanostructuré issues de l'anodisation électrochimique: élaboration, propriétés physico-chimiques et applications.* Doctoral dissertation, Institut National des Sciences Appliquées de Lyon, Lyon, France, 2006.

[63] Md Mostafizur Rahman, Tanvir Mahtab, M Zobayer Bin Mukhlish, MO Faruk, and Mohammed Mastabur Rahman. Enhancement of electrical properties of metal doped polyaniline synthesized by different doping techniques. *Polymer Bulletin*, 78(9):5379–5397, 2021.

[64] Wang Lin. Polyaniline and its nanocomposites for green energy production and storage. M.sc. thesis, Pittsburg State University, Pittsburg, KS, USA, May 2021. Advisor: Dr. Ram K. Gupta.

[65] Tingting Zhu, Jin Zhou, Zhaohui Li, Shijiao Li, Weijiang Si, and Shuping Zhuo. Hierarchical porous and n-doped carbon nanotubes derived from polyaniline for electrode materials in supercapacitors. *Journal of Materials Chemistry A*, 2(31):12545–12551, 2014.

[66] Jérôme Toupin. *Photoélectrolyse de l'eau : étude de matériaux semiconducteurs de type P comme photocathode pour la réduction de protons en H.* Doctoral dissertation, Université Pierre et Marie Curie (Paris VI), Paris, France, 2016.

[67] W. Li, N. Jiang, B. Hu, T. B. Hanson, T. L. Liu, and Y. Sun. Electrolyzer design for flexible decoupled water splitting and organic upgrading with electron reservoirs. *Chem*, 4:637–649, 2018.

[68] Quan-Bao Ma, Jürgen Ziegler, Bernhard Kaiser, Dominic Fertig, Wolfram Calvet, Eswaran Murugasen, and Wolfram Jaegermann. Solar water splitting with p-sic film on p-si: Photoelectrochemical behavior and xps characterization. *International Journal of Hydrogen Energy*, 39:1623–1629, 2014.

[69] Michael C. Leech and Kwok Lam. A practical guide to electrosynthesis. *Nature Reviews Chemistry*, 6(4):275–286, April 2022.

[70] Hugues R. Paqueton et al. Microscopie électronique à balayage: principe et équipement. *Techniques de l'ingénieur*, page P865, 2006.

[71] Élodie Charon. *Géochimie et nanostructures de carbones des achondrites primitives : recherche de signatures pré-accrétionnelles par SIMS, Raman et METHR.* Doctoral dissertation, Université Paris-Sud, Orsay, France, 2012.

[72] Hélène Colder. *Croissance basse température de films minces de carbure de silicium nanocristallisé : propriétés et performances d'hétérojonctions SiC/Si.* Doctoral dissertation, Université de Caen–Basse-Normandie, Caen, France, 2005.

[73] N. M. Rahim and Y. Ould Mohamed. Élaboration des matériaux hybrides pour la valorisation du co par photocatalyse. Master's thesis, Université des Sciences et de la Technologie Houari Boumédiène (USTHB), Alger, Algeria, 2022.

[74] M. P. Fuller and P. R. Griffiths. Diffuse reflectance measurements by infrared fourier-transform spectrometry. *Analytical Chemistry*, 50:1906–1910, 1978.

[75] Samir Kaci. La photo-électro-réduction du co. Research report, Centre de Recherche en Technologie des Semi-conducteurs et Énergies Renouvelables (CRTSE), Arzew, Algeria, 2019.

[76] GeeksforGeeks. What is x-ray diffraction? https://www.geeksforgeeks.org/physics/what-is-x-ray-diffraction/, 2025. Last updated April 22, 2025; accessed July 1, 2025.

[77] VEQTER Ltd. X-ray diffraction: Residual stress measurement. https://www.veqter.co.uk/residual-stress-measurement/x-ray-diffraction, 2024. Accessed: 2025-07-01.

[78] J. K. Kim, K. S. Kim, and C. W. Tu. Optical properties of silicon and germanium in the extreme ultraviolet. *Physical Review B*, 6(12):4502–4513, 1972.

[79] Aude Gandon. *Développement de méthodes d'analyses permettant le screening de molécules pharmaceutiques à l'aide du Sirius T3 : détermination de constantes d'acidité de molécules ionisables par spectrophotométrie UV-visible et analyse en composantes principales.* Doctoral dissertation, Université de Limoges, Limoges, France, 2014.

[80] Houyem Slimi. *Élaboration et caractérisation de couches minces co-dopées In, Co préparées par pulvérisation cathodique : applications aux cellules photovoltaïques.* Doctoral dissertation, Universités du Littoral Côte d'Opale et de Sfax, Dunkerque, France & Sfax, Tunisia, 2019.

[81] Isabelle Fotsing. *Étude par voltammétrie cyclique des conditions d'électrodéposition de phosphure de zinc pour des applications photovoltaïques.* Doctoral dissertation, Université de Montréal, Montréal, Canada, 2015.

[82] Djaouida Allam. *Réactivité catalytique de CO sur des catalyseurs d'oxydes métalliques et hétéropolyanioniques.* Doctoral dissertation, Université Mouloud Mammeri de Tizi-Ouzou (UMMTO), Tizi-Ouzou, Algeria, 2019.

[83] D.E. Stilwell and S.M. Park. Electrochemistry of conductive polymers. electrochemical studies on growth properties of polyaniline. *Journal of the Electrochemical Society*, 135:2254, 1988.

[84] L. Talbi, M. Berouaken, K. Khaldi, A. Keffous, N. Gabouze, M. Trari, H. Menari, and Y. Belkacem. Elaboration and characterization of electrochemically prepared h+ doped polyaniline/au/a-sic: H based chemical sensor. *Journal of Solid State Electrochemistry*, December 2017.

[85] P. Snauwaert, R. Lazzaroni, J. Verbist, and D. Gonbeau. In *Springer Series in Solid State Sciences*, volume 91, pages 301–304. Springer, 1989.

[86] L.X. Zhang, P. Liu, and Z.X. Su. Preparation of pani–tio2 nanocomposites and their solid-phase photocatalytic degradation. *Polymer Degradation and Stability*, 91:2213–2219, 2006.

[87] C.Q. Bian, Y.J. Yu, and G. Xue. Synthesis of conducting polyaniline/tio2 composite nanofibres by one-step in situ polymerization method. *Journal of Applied Polymer Science*, 104:21–26, 2007.

[88] L.G. Gai, G.J. Du, Z.Y. Zuo, Y.M. Wang, D. Liu, and H. Liu. Controlled synthesis of hydrogen titanate–polyaniline composite nanowires and their resistance temperature characteristics. *Journal of Physical Chemistry C*, 113:7610–7615, 2009.

[89] H. Liu, X.B. Hu, J.Y. Wang, and R.I. Boughton. Structure, conductivity, and thermopower of crystalline polyaniline synthesized by the ultrasonic irradiation polymerization method. *Macromolecules*, 35:9414–9419, 2002.

[90] K.A. Khan. Stability of a cu2o photoelectrode in an electrochemical cell and the performances of the photoelectrode coated with au and sio2 thin films. *Applied Energy*, 65:59–66, 2000.

[91] P. Chutia and A. Kumar. Electrical, optical and dielectric properties of hcl doped polyaniline nanorods. *Physica B: Condensed Matter*, 436:200–207, 2014.

[92] Surajit Sinha, Sambhu Bhadra, and Dipak Khastgir. Effect of dopant type on the properties of polyaniline. *Journal of Applied Polymer Science*, 112(5):3135–3140, 2009.

[93] Parisa Najmi, Navid Keshmiri, Mohammad Ramezanzadeh, and Bahram Ramezanzadeh. Synthesis and application of zn-doped polyaniline modified multi-walled carbon nanotubes as stimuli-responsive nanocarrier in the epoxy matrix for achieving excellent barrier-self-healing corrosion protection potency. *Composites Part B: Engineering*, 223:109102, 2021.

[94] Ahmad Abdolahi, Azizah Abdul Hamid, Zainovia Lockman, and Azmi Zakaria. Synthesis of uniform polyaniline nanofibers through interfacial polymerization. *Materials*, 5(8):1487–1494, 2012.

[95] Bhupendra K. Sharma, Ajai K. Gupta, Neeraj Khare, S. K. Dhawan, and H. C. Gupta. Synthesis and characterization of polyaniline–zno composite and its dielectric behavior. *Composites Science and Technology*, 67(11–12):2132–2136, 2007.

[96] S. Maadadi, M. E. A. Benamar, Y. Mebdoua, et al. Investigation of optical, dielectric, and electrical properties of zno/cold sprayed al system and their correlation with photovoltaic performance. *Optical and Quantum Electronics*, 57:1–27, 2025.

[97] N. E. Arabi, Y. Bencheikh, W. Achour, et al. Facile hydrothermal synthesis of rgo/coso4 composite as high-performance supercapacitor electrode: Effect of autoclave and non-autoclave. *Diamond and Related Materials*, 135:112416, 2025.

[98] K. Derkaoui, T. Hadjersi, K. Boukhouidem, et al. Optical, dielectric and photoelectrochemical performances of the ceo2/silicon nanowire system: Studying the silicon nanowire length effect on the photodegradation of rhodamine b. *Reaction Kinetics, Mechanisms and Catalysis*, 138:499–518, 2024.

[99] A. Nair, A. Kurian, A. Samuel, and S. Sumathi. Photocatalytic degradation of crystal violet using yttrium and copper co-doped nickel aluminate. *Environmental Science and Pollution Research*, pages 1–14, 2025.

[100] Y. Tong, Y. Wei, A. J. Song, et al. Polyaniline/tungsten trioxide organic-inorganic hybrid anode for aqueous proton batteries. *Chemistry – A European Journal*, 30:e202401257, 2024.

[101] Shaheen Shah, S. Oladepo, M. A. Ehsan, et al. Recent progress in polyaniline and its composites for supercapacitors. *The Chemical Record*, 24:e202300105, 2024.

[102] H. J. Li, C. Chen, X. Zhang, et al. Dual-functional silicon nanowire arrays-based photocatalytic fuel cell for solar-to-electricity conversion and self-powered glucose detection. *Journal of Power Sources*, 603:234432, 2024.

[103] M. Liang and M. Zheng. Reaction of spinel cufe2o4 oxygen carrier with converter off-gas during chemical looping combustion: An experimental characteristic and decomposition kinetic study. *Journal of Environmental Chemical Engineering*, 13:115131, 2025.

[104] K. Derkaoui, I. Belkhettab, I. Bencherifa, et al. Optical and dielectric properties of nife2o4 prepared by co-precipitation: correlation with photocatalytic performance for rhodamine b degradation under visible light. *Reaction Kinetics, Mechanisms and Catalysis*, pages 1–19, 2025.

[105] K. Derkaoui, I. Bencherifa, A. Elfiad, et al. Unveiling the optical and dielectric properties of mnfe2o4: A high-performance visible-light photocatalyst for sustainable rhodamine b degradation. *Journal of Electronic Materials*, pages 1–16, 2025.

[106] Amera G Baker. The study of optical energy gap, refractive index, and dielectric constant of pure and doped polyaniline with hcl and h2so4 acids. *ARO-The Scientific Journal of Koya University*, 7(1):47–52, 2019.

[107] Patrycja Makuła, Michał Pacia, and Wojciech Macyk. How to correctly determine the band gap energy of modified semiconductor photocatalysts based on uv–vis spectra, 2018.

[108] Andrews Nirmala Grace, Song Yi Choi, Mari Vinoba, Margandan Bhagiyalakshmi, Dae Hyun Chu, Yeoil Yoon, Sung Chan Nam, and Soon Kwan Jeong. Electrochemical reduction of carbon dioxide at low overpotential on a polyaniline/cu2o nanocomposite based electrode. *Applied Energy*, 120:85–89, 2014.

[109] K. Benfadel, S. Kaci, M. Leitgeb, A. Ouerek, and F. Kezzoula. Photoelectrochemical conversion of co2 using nanostructured pbs–si photocathode. *Journal of Applied Electrochemistry*, 52(5):835–848, 2022.

[110] W. Gao, Y. Zhang, Y. Wang, J. Xu, Y. Feng, M. Meng, and K. Liu. Nail-like cu2s nanoarrays with a partial interconnected structure synthesized on cu foam for high-performance asymmetric supercapacitors. *Journal of Materials Science: Materials in Electronics*, 32(16):21770–21779, 2021.

[111] K. W. Frese. Electrochemical reduction of co2 at intentionally oxidized copper electrodes. *J ElectrochemSoc*, 138(44):3338, 1991.

[112] M. D. Ward and A. J. Bard. Photocurrent enhanced via trapping of photogenerated electrons of tio2 particles. *J. Phys. Chem.*, 86(18):3599–360, 1982.

[113] Jong-Hyun Park, Soo-Young Lee, Min-Ho Kim, and Hyeon-Seo Choi. High-efficiency gas chromatography analysis of CO reduction products using a modified capillary column. *Journal of Chromatography A*, 1595:187–195, 2019.

[114] Seung-Min Park, Ji-Hoon Kim, Eun-Bi Park, and Tae-Hyun Kwon. Quantitative analysis of liquid products from photoelectrochemical CO reduction via high-performance liquid chromatography. *Analytical Chemistry*, 93(12):5123–5131, 2021.